

**Remote Sensing and Modeling of the Earth's
Middle Atmosphere: Results of the CRISTA
Experiment**

Habilitationsschrift zur Erlangung der Venia Legendi

vorgelegt von

Martin Riese

Bergische Universität-Gesamthochschule Wuppertal

Fachbereich 8 - Physik

August 2000

Contents

1	Introduction	1
2	The CRISTA experiment	4
2.1	Measurement technique	4
2.2	Sampling grid and observational geometry	6
2.3	Data system	9
2.4	Data processing and temperature and trace gas retrieval	11
2.5	Synoptic mapping of measured trace gas fields	22
2.6	Data validation	25
3	Dynamical processes observed by CRISTA	30
3.1	Atmospheric waves	30
3.2	Tracer transport by inertially unstable circulation	37
3.3	Exchange of tropical and extra-tropical air	41
4	Three-dimensional modeling of the stratosphere	46
4.1	Model description	46
4.2	Simulation of the CRISTA measurement periods	48
5	Trace gas assimilation	60
5.1	The sequential approach	60
5.2	Transport studies based on assimilated trace gas fields	65
5.3	Modeling of chemically active species	71
6	Summary	78
7	References	82

List of Figures

1	CRISTA measurement configuration	5
2	Horizontal sampling grid of CRISTA-1	6
3	Footprints of the SCS spectrometer during CRISTA-2	8
4	Limb-viewing geometry of the CRISTA telescopes	8
5	Limb-radiance spectra measured by a detector channel of the left telescope (SL5)	9
6	Flowchart of the CRISTA data processing	10
7	Global distribution of CFC-11 limb-radiance values at 18 km altitude .	12
8	Radiative transfer in the atmosphere	14
9	Comparison of measured and simulated CO ₂ limb-radiance spectra . . .	19
10	Mixing ratios of ClONO ₂ measured by CRISTA on November 6, 1994 at 21 km altitude	21
11	Comparison of measured and assimilated CFC-11 values at 46.4 mbar for November 6, 7, and 10, 1994	23
12	Validation orbit on August 11, 1997	26
13	Temperature profiles of two falling spheres and the corresponding zero miss distance temperature profile of CRISTA	26
14	Eq/ Θ mapped ozone values of six instruments operated during ATLAS 3	28
15	Local solar time distribution (LST) of the center telescope	31
16	Comparison of temperature amplitudes of the diurnal tide measured by CRISTA with corresponding GSWM results	32
17	Wave-two geopotential perturbation field during CRISTA-2	34
18	South polar view of CRISTA-2 temperature fields	35
19	Same as Figure 18 but for ozone	35

20	Longitude vs altitude cross section of CRISTA temperatures detrended from the longitudinal mean for several observation periods	38
21	Zonal mean CH ₄ mixing ratio averaged over the CRISTA-1 mission . . .	39
22	Ertels potential vorticity (EPV) derived from CRISTA data on the 1800 K (48 km) isentropic surface	40
23	Mixing ratios of HNO ₃ measured by CRISTA on November 6, 1994 at 22.5 mbar (25 km)	42
24	Mixing ratios of CH ₄ measured by CRISTA on August 11, 1997 at 4.6 mbar (35 km)	43
25	Analyzed (assimilated) CRISTA distributions of CH ₄ , N ₂ O, and CFC-11 on August 11, 1997	44
26	Comparison of a measured and modeled northern hemispheric N ₂ O distribution for November 6, 1994, at 14.7 mbar	49
27	Comparison of measured and modeled longitudinal plots of detrended N ₂ O values at 14.7 mbar	50
28	Measured and modeled time sequence (November 6 to November 10, 1994) of the northern hemispheric CFC-11 distribution at 31.6 mbar . . .	51
29	Comparison of measured and modeled longitudinal plots of detrended CFC-11 values at 31.6 mbar for November 6 , and 8, 1994	52
30	Comparison of a measured, an analyzed, and a modeled southern hemispheric distribution of N ₂ O for November 6, 1994 at 10 mbar	54
31	Temporal evolution of the southern hemispheric N ₂ O distribution at the 10 mbar pressure level	56
32	Comparison of measured and modeled CH ₄ distributions for August 11, 1997 at 4.6 mbar	58
33	Mixing ratios of HNO ₃ measured by CRISTA on November 6, 1994 at 22.5 mbar projected onto a regular CTM grid	61
34	Mixing ratios of CH ₄ measured by CRISTA on August 11 and August 14, 1997 at 4.6 mbar projected onto a regular CTM grid	63

35	Analyzed (assimilated) CH ₄ mixing ratios for August 11 and August 14, 1997 at 4.6 mbar	64
36	Comparison of the meridional CFC-11 eddy flux (31.6 mbar) derived from assimilated CRISTA data with respective model results	67
37	Time sequence of assimilated CH ₄ data of CRISTA at 4.6 mbar	69
38	Comparison of measured zonal mean tendencies of CH ₄ mixing ratios with calculated tendencies	70
39	Comparison of measured and simulated zonal mean profiles (30°N to 50°N) of nitrogen components for early nighttime conditions (19 LT)	73
40	Comparison of measured and modeled diurnal variations of nitrogen species in the middle stratosphere (50°N to 60°N)	75
41	Comparison of measured and modeled nitrogen species for November 6, 1994, at 22.5 mbar (25 km)	76

1 Introduction

Small- and medium-scale structures play an important role in atmospheric dynamics and photochemistry. This has been demonstrated, for example, by simultaneous observations of ground-based, balloon-borne, and rocket-borne (GBR) experiments (e. g. *Offermann, 1994*), by high-altitude aircraft observations (e. g. *Bacmeister et al., 1996*), and by results from three-dimensional models (e. g. *Rood et al.; 1991, Rose and Brasseur, 1989*). Limb observations of atmospheric temperature and trace gas fields from satellites provide a wealth of data for investigations of dynamical and photochemical structures in the middle atmosphere with global coverage. However, present-day limb-sounding instruments lack horizontal resolution. The Cryogenic Infrared Spectrometers and Telescopes for the Atmosphere (CRISTA) instrument aboard the Shuttle Palette Satellite (SPAS) [*Offermann et al., 1999*] was developed for global limb measurements of trace gas emissions in the infrared region with improved horizontal resolution (typically 6° in longitude and 3° in latitude). The main scientific objective was to study small- and medium-scale structures in stratospheric trace gas fields which result, for example, from planetary wave breaking (e. g. *McIntyre and Palmer, 1983*) and associated transport processes (e. g. *Rose and Brasseur, 1989*).

At the beginning of the CRISTA project it was not clear to what extent small and medium-scale structures would be present in the atmosphere. The experiment was thus exploratory in nature and relatively short missions lasting about a week appeared to be adequate. The instrument was especially designed to operate during missions of NASA's Space Shuttle. It was successfully flown during the missions STS 66 (November 1994) and STS 85 (August 1997). The first flight in early November 1994 was part of the ATmospheric Laboratory for Application and Science 3 (ATLAS-3) mission of NASA (*Kaye and Miller, 1996*). CRISTA-1 was launched aboard the Space Shuttle Atlantis into a 300 km, 57° inclination orbit. During a free-flying period of seven days about 50,000 height profiles of limb-radiance spectra were measured by using a number of different measurement modes, including scans of different altitude regions of the atmosphere, and some calibration modes (Section 2). The latitudinal coverage was from -57° to $+67^\circ$. CRISTA-2 was launched on August 7, 1997 by Space Shuttle Discovery (300 km circular orbit, 57° inclination). During this mission the latitudinal coverage of the observation was extended to the latitudinal band from

-74° to +74° by utilizing the maneuver capabilities of the CRISTA-SPAS satellite (*Grossmann, 2000*).

Atmospheric temperature and trace gas distributions retrieved from CRISTA radiance observations demonstrate that the instrument is well suited to resolve dynamical structures such as atmospheric waves and effects of transport processes (Sections 3 to 5). Atmospheric waves such as planetary waves, gravity waves, and tidal oscillations play an important role in the dynamics of the atmosphere, e. g. in the mean circulation. Vertically propagating waves generated in the troposphere provide, for example, a large fractions of eddy momentum and heat fluxes in the middle atmosphere (*Holton, 1975*). The stratospheric meridional circulation is predominantly driven by planetary waves. In the winter hemisphere mass is transported poleward as a result of wave breaking. Conservation of mass leads to downward motion in the polar region and upward motion in the tropics, whereby the mean vertical velocity at a given level is controlled by the integrated wave dissipation above this level (downward control principle, e. g. *Haynes et al., 1991*). Planetary waves drive the mean meridional circulation and at the same time facilitate quasi-horizontal mixing of chemical species. Transport effects are most pronounced in the stratospheric surf zone (e. g. *McIntyre and Palmer, 1983*), which connects the tropical transport barrier (e. g. *Trepte et al., 1993*) with mid-latitudes. As shown in Sections 3 to 5, high resolution trace gas fields measured by CRISTA are ideally suited for studies of such stratospheric transport processes. In addition, CRISTA observations provide valuable information on trace gas transport at higher altitudes. In the stratopause region (50 km) circulation cells arising from inertially unstable conditions appear to play a significant role in tracer transport (Section 3.2).

Planetary waves are always present in the winter stratosphere with highly variable amplitudes and phases. The quasi-stationary planetary wave-one is the most pronounced feature in the northern winter hemisphere, while the southern hemispheric winter circulation is dominated by traveling planetary waves. During both missions, CRISTA observed pronounced planetary wave activity causing large deviations from zonal symmetry. At the beginning of the CRISTA-1 period the stratospheric dynamics was dominated by a pronounced wave-two structure, which decayed in favor of a planetary wave-one during the course of the mission. The large wave activity was associated with relatively large exchange of tropical and extra-tropical air, mainly in

form of planetary-scale tongues of tropical and polar air (Section 3.3). Similar results were obtained for the southern hemispheric winter stratosphere during the second CRISTA mission. Pronounced traveling planetary waves caused a stratospheric surf zone containing air masses of highly variable mixing ratio values.

High resolution stratospheric trace gas distributions measured by CRISTA are ideally suited to test the ability of chemical transport models (CTM) to produce accurate synoptic trace gas distributions and to account for the important transport processes discussed above. For this reason, simulations of the CRISTA measurement periods were performed with a three-dimensional CTM, which combines the transport and chemistry codes of the National Center for Atmospheric Research (NCAR) Research on Ozone in the Stratosphere and Its Evolution (ROSE) model (e. g. *Rose and Brasseur*, 1989) with wind and temperature fields provided by the UK Meteorological Office (*Swinbank and O'Neill*, 1994). In general, very good agreement is found between measured and simulated trace distributions (Section 4). For quantitative studies of transport and photochemical processes, the ROSE CTM was used as the core of a sequential data assimilation system (Section 5). The assimilation system provides synoptic distributions that are consistent with the CRISTA measurements at each time step of the model (20 min). Data gaps are filled and the measured trace gas fields are extrapolated towards higher latitudes, which are not accessible to observation. In addition, the assimilation system provides distributions of unmeasured species (consistent with measured species). All trace gas fields are available on the temporal and spatial grid of the meteorological fields. This allows for quantitative studies of dynamical processes such as the influence of eddy fluxes on the temporal evolution of the background atmosphere (Section 5.2). In addition, the assimilation system can be used to separate dynamical and photochemical processes in simulations of short-lived species such as NO_2 and N_2O_5 (Section 5.3).

2 The CRISTA experiment

2.1 Measurement technique

Global measurements of atmospheric infrared emissions provide the opportunity to derive distributions of a variety of minor constituents simultaneously. A number of experiments have therefore used the limb-sounding technique to measure infrared emissions of atmospheric trace gases. This technique yields good spatial coverage as well as good horizontal and vertical resolution. In addition, it allows measurements during daytime and nighttime. Global limb measurements of thermal emissions of atmospheric trace gases were performed by several instruments. The LIMS (Limb Infrared Monitor of the Stratosphere) [Gille and Russell, 1984] and SAMS (Stratosphere and Mesosphere Sounder) [Drummond *et al.*, 1980] instruments aboard the NIMBUS 7 satellite were launched in October 1978 and provided seasonal cycles of several trace gases. More recently, the CLAES (Cryogenic Limb Array Etalon Spectrometer) [Roche *et al.*, 1993] and ISAMS (Improved Stratosphere and Mesosphere Sounder) [Taylor *et al.*, 1993] instruments performed emission measurements aboard the Upper Atmospheric Satellite (UARS), a platform with nine instruments for a comprehensive study of the chemistry, dynamics, and energetics of the upper atmosphere (Reber, 1985). There are several upcoming limb-viewing instruments sensing infrared emissions of atmospheric trace constituents including the SABER (Sounding of the Atmosphere using Broadband Emission Radiometry) radiometer (Mlynczak, 1997) on NASA's TIMED (Thermosphere Ionosphere Mesosphere Energetics and Dynamics) satellite and the MIPAS (Michelson Interferometer for Passive Atmospheric Sounding) instrument (Endemann *et al.*, 1993) on board ESA's ENVISAT platform. The High Resolution Dynamics Limb Sounder (HIRDLS) [Gille and Barnett, 1992] and the Tropospheric Emission Spectrometer (TES) [Beer, 1996] will fly on board NASA's Earth Observing System AURA (EOS AURA) satellite in 2003.

The Cryogenic Infrared Spectrometers and Telescopes for the Atmosphere instrument (CRISTA) aboard the Shuttle Palette Satellite (SPAS) [Offermann *et al.*, 1999] was developed to provide global measurements of atmospheric infrared emissions with increased horizontal resolution. The limb-scanning technique is used to measure thermal emissions (4 - 71 μm) of selected atmospheric trace gases with unprecedented horizontal resolution. The instrument is mounted on the reusable CRISTA-SPAS

satellite (*Wattenbach and Moritz, 1992*) which is released from the Shuttle and operates at a distance of 50 - 100 km behind it (Figure 1). The CRISTA-SPAS satellite includes a star tracker for very accurate attitude control. The platform also houses the MAHRSI (Middle Atmosphere High Resolution Spectrograph Investigation) instrument which performs UV measurements of OH and NO in the middle atmosphere (*Conway et al., 1999*). After its missions the CRISTA-SPAS satellite is retrieved by the Shuttle.

For improved horizontal resolution CRISTA uses 3 telescopes that sense the atmosphere at angles 18° apart. The detectors and the optics are cooled by cryogenic helium. This results in high sensitivity of the infrared detectors, and consequently, high measuring speed and high spatial resolution. Altitude scans are performed by using tiltable mirrors. The incoming radiance is analyzed by four grating spectrometers with a spectral resolution of about 500. Each telescope feeds a spectrometer for short wavelength from 4 to $14 \mu\text{m}$. The center telescope feeds, in addition, a spectrometer for longer wavelength up to $71 \mu\text{m}$. The large altitude range of the observations (7 to 180 km) allows for comprehensive studies of dynamical features over a wide range of altitudes (e. g. atmospheric waves). The spectral resolution of the instrument is sufficient to provide valuable information on the distribution of trace species at low altitudes, e. g. in the upper troposphere (*Schäler and Riese, 2000*). A detailed description of the instrument, tests, calibrations, measured trace gases, and the data system is given by *Offermann et al. (1999)* and by *Riese et al. (1999a)*.

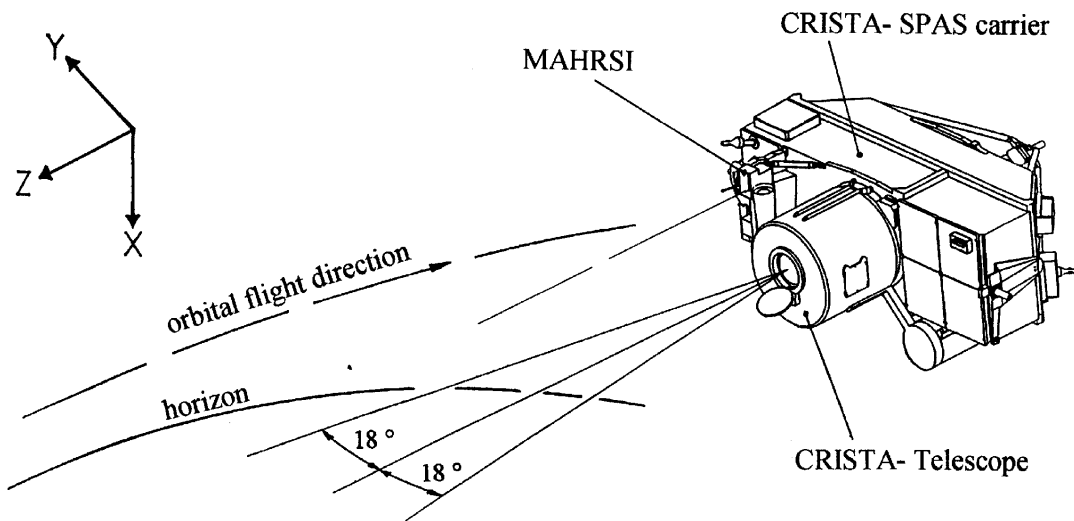


Figure 1: CRISTA measurement configuration

2.2 Sampling grid and observational geometry

The horizontal net of measurement points is sketched in Figure 2 for four consecutive orbits during CRISTA-1. The earth rotates underneath the orbital track which is almost stationary with respect to the sun. The orbital period of about 90 minutes results in large gaps (2500 km) between subsequent orbital tracks at the equator. In the case of CRISTA, these gaps are filled by the tangent point tracks of the lateral telescopes. Each dot in Figure 2 represents complete altitude profiles of more than 15 trace gases. The viewing directions of the three telescopes are separated by 18° . This yields a horizontal distance between the tangent points of about 600 km across the flight track. The horizontal distance of two subsequent measurement points (profiles) along the flight track are on the order 200 to 400 km, depending on the measuring mode. At the northern and southern turning point of the orbital track a complete coverage of a latitudinal circle takes about 24 hours. At the equator, a complete coverage takes only 12 hours since the ascending and the descending nodes are separated by about 180° (12 hours in local time).

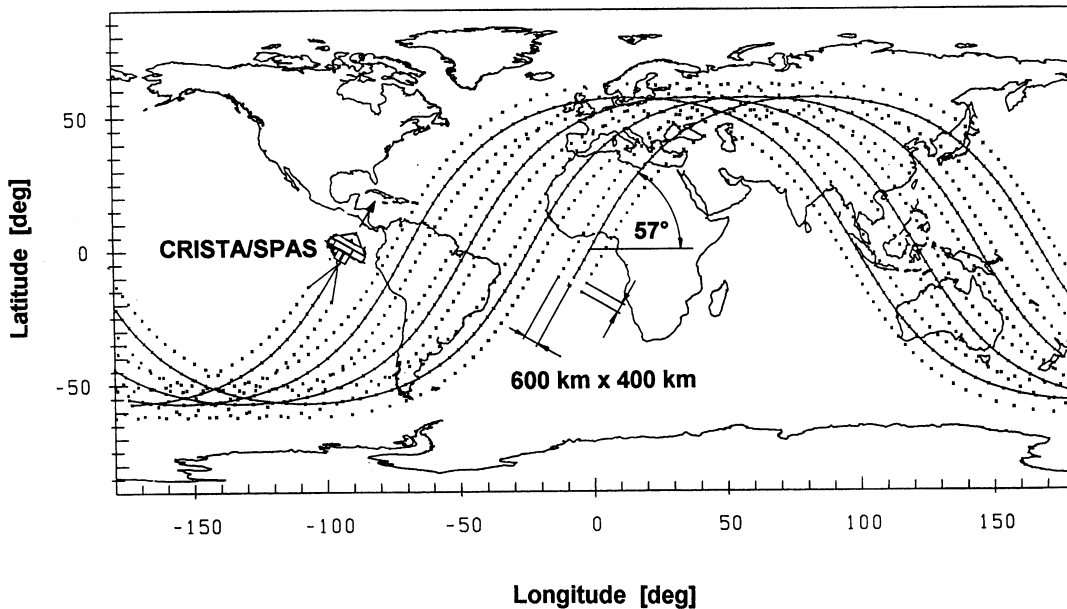


Figure 2: Horizontal sampling grid for four subsequent orbits during CRISTA-1. Each dot represents complete altitude profiles of more than 15 trace gases. The horizontal distance of two adjacent profiles along the flight track is on the order of 200 to 400 km, depending on the measurement mode.

Mode ID	Objective	Altitude range (km)*	Vertical Step (km)	Step along track (km)	Hours of data
1	Stratosphere/ Mesosphere	16 - 79 (125)	1.5	400	54.6
2	Stratosphere	16 - 44 (73)	1.5	200	76.7
M/T	Mesosphere/ lower Thermosphere	60 - 164	2.7	360	4.3
V/R-1	check of IR detectors	16 - 79	1.5	720	5
V/R-2	check of IR detectors	16 - 44	3.0	190	5
H/O	oversampling	22 - 35	0.75	200	15
					160.6

Table 1: CRISTA-1 measurement modes

* The altitudes of the long wavelength spectrometer are about 24 km higher than the numbers given.

For CRISTA-2 the maneuver capabilities of the CRISTA-SPAS satellite were considerably improved. An example of three consecutive orbits during CRISTA-2, including a so-called validation orbit, is given in Figure 3. Shown are the footprints of profiles of a spectrometer (SCS) of the center telescope. The first and the third orbit are representative of the so-called ping-pong mode. In this mode the viewing direction was tilted northward in the northern parts of the orbits (and southward in the southern parts). This way, the latitudinal coverage of the measurements was extended to 74° N and 74° S. The ping-pong mode was used during most of the operational time. The second orbit shown in Figure 3 is a validation orbit, where the viewing direction of the center telescope was directed towards the two main sites of the CRISTA/MAHRISI validation campaign located at Wallops Islands, Virginia, USA (37.9° N, 75.5° W), and Hohenpeissenberg, Germany (47.8° N, 11.0° E). These stations are indicated by the full diamonds in Figure 3.

The CRISTA instrument measures the radiance emitted by the atmosphere along the line-of-sight (Figure 4). The distance of the tangent point from the instrument is on the order of 2000 km. The height of the line-of-sight that is closest to the surface is the tangent height (TH in Figure 4), the corresponding point is the tangent point. The atmosphere is scanned from high to low tangent heights by tilting the telescope mirrors with an angle step that corresponds to a tangent height step of

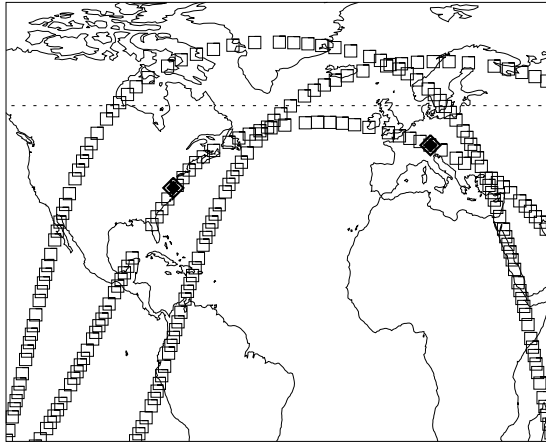


Figure 3: Footprints of the CRISTA spectrometer (open squares) for three subsequent orbits. The second orbit is a validation orbit with CRISTA pointing at Wallops Island and Hohenpeissenberg (full diamonds). A dotted line is drawn at 57° N indicating the orbit inclination.

1.5 km. Typical stratospheric limb-radiance spectra observed during CRISTA-1 are shown in Figure 5 for a detector channel of the left telescope (SL5).

The limb-viewing geometry yields relatively good vertical resolution since the line-of-sight segment immediately above the tangent point is relatively large (see Figure 4) and the total density of the atmosphere decreases greatly with altitude. About 50% of the measured limb-radiance signal originates from a 2 km thick layer above the tangent point (assuming optically thin conditions, an infinitesimal field of view, and

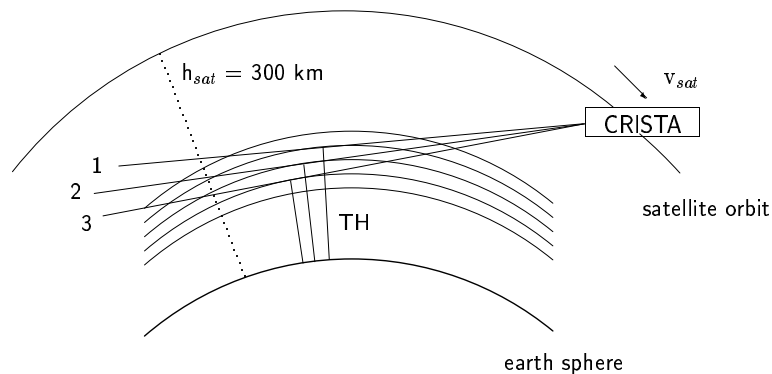


Figure 4: Limb-viewing geometry of one of the CRISTA telescopes. The atmosphere is scanned from high to low tangent heights by means of a tiltable mirror. During an altitude scan the mirrors of all three telescopes are tilted simultaneously.

a negligible vertical gradient in the trace gas mixing ratio profile).

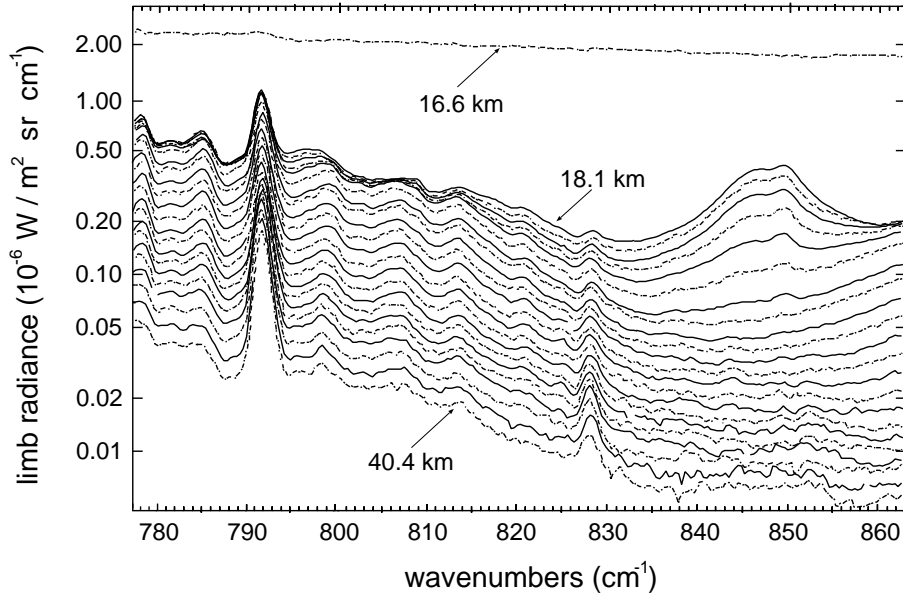


Figure 5: Logarithmic plot of limb-radiance spectra measured by a detector channel (SL5) of the left telescope in the altitude range from 16.6 to 40.4 km. The emission at the lowest tangent height is caused by subvisible cirrus clouds (e. g. *Offermann and Spang, 1998*)

2.3 Data system

A flowchart of the data evaluation process is sketched in Figure 6. During the two missions all data were stored on magnetic tape aboard the CRISTA-SPAS satellite. These recorder data are the basis of four data products (level 0 to level 3).

CRISTA level 0 data contain detector output voltages, signals from the tilting mirrors of the telescopes and gratings of the spectrometers, and data from about 200 housekeeping channels. The detector signals undergo several corrections (e. g. for electrical interferences and spikes), before they are converted to limb-radiance spectra on an instrument sampling grid (level 1 data) by means of several calibration factors, calibration functions, and CRISTA-SPAS attitude data (e. g. *Riese and Offermann, 2000*). The fast measurement technique of CRISTA results in a large amount of radiance data. The radiative transfer calculations required to retrieve atmospheric pressures, temperatures, and trace gas mixing ratios (level 2 data) are very complex and several iterations of the whole retrieval process (data versions) have to be

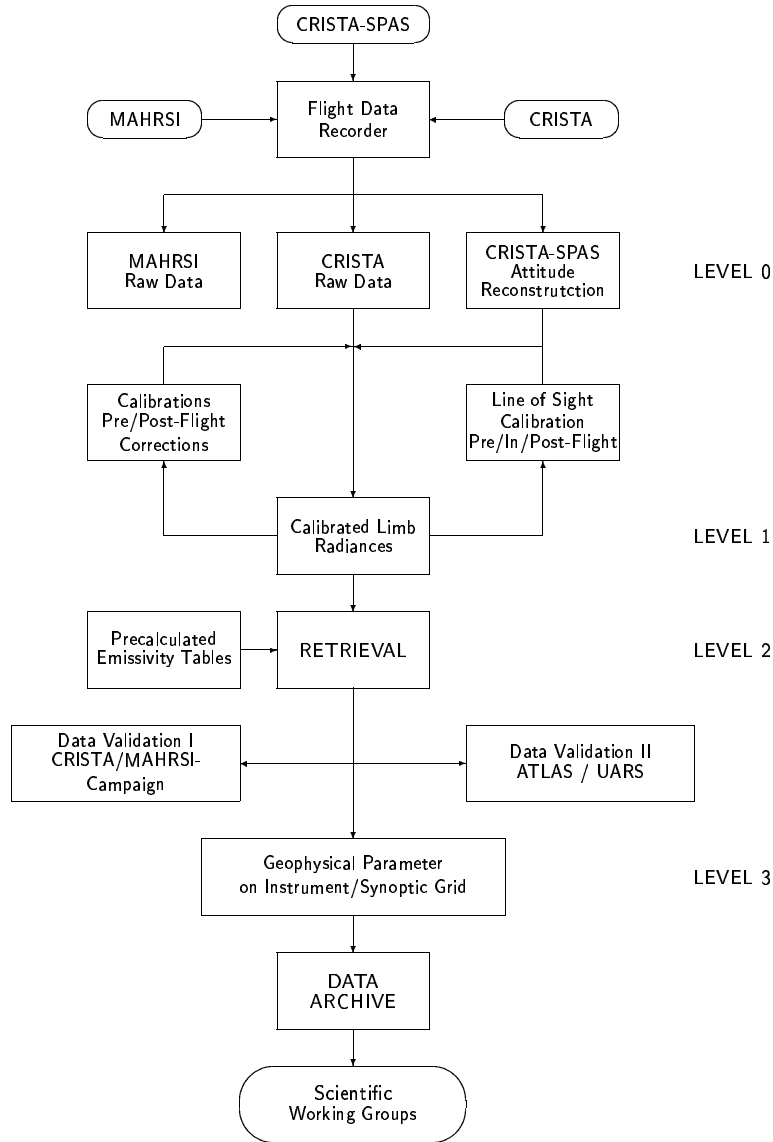


Figure 6: Flowchart of the CRISTA data processing

performed in order to achieve high-quality retrieval results. The CRISTA retrieval therefore uses fast radiative transfer codes based on atmospheric emissivity lookup tables pre-calculated by means of the Linepak library (*Gordley et al., 1994*). The lookup tables were calculated at the spectral resolution of the instrument. This allows very fast and accurate forward calculations of atmospheric infrared spectra by means of the Bandpak libraries (*Marshall et al., 1994*). In general, the measured spectra are of good quality and instrument effects are well understood. It is therefore possible to accurately model the measured signals and to perform the retrieval by simple multiple-emitter onion-peeling retrieval schemes. The resulting level 2 data are atmospheric

pressures, temperatures, and trace gas mixing ratios on an instrument grid. For further analyses, the level 2 data are interpolated to a regular latitude/longitude grid and common synoptic times (level 3 data) using several gridding methods described in Section 2.5.

2.4 Data processing and temperature and trace gas retrieval

Global radiance fields

Global limb-radiance distributions are the primary measurement quantity of CRISTA. In the CRISTA data system, calibrated limb-radiance spectra (see Figure 5) are registered in terms of limb-radiance profiles. The accuracies of the radiometric calibration and of the wavelength calibration are on the order of 2% and $\Delta\lambda/6$ respectively. The location of each spectrum, i.e. longitude, latitude and tangent height, is derived from CRISTA-SPAS attitude data and line-of-sight calibrations (tilting angle calibrations of the primary mirrors). An accurate attitude reconstruction is very important since the tangent height data enter the pressure and temperature retrieval of CRISTA. The CRISTA observations take advantage of the CRISTA-SPAS attitude system which consists of a star camera, two gyro packages, and a GPS receiver. During the CRISTA missions, the major axis Z of CRISTA-SPAS (Figure 1), which is in the same direction as the optical axis of the center telescope, pointed at a constant tangent height of about 63 km. This required the eccentricity of the orbit as well as the earth's oblateness to be taken into account. The in-flight accuracy of the tangent height of the CRISTA-SPAS Z axis is on the order of 250 m. The post-flight accuracy is of the order of 70 m at the tangent point. The alignment between the CRISTA-SPAS attitude system and CRISTA was determined by laboratory measurements. Knowledge about the alignment was verified (and improved) by means of in-flight line-of-sight calibrations using the planet Mars (CRISTA-1) and the planet Jupiter (CRISTA-2) as calibration sources. The overall accuracy of the tangent height reconstruction is on the order of 200 to 300 m for CRISTA-1 and about 100 m for CRISTA-2. Knowledge of the relative spacing of the tangent points of individual profiles is on the order of 60 m. This allows for accurate pressure and temperature retrievals, and thus, reliable calculations of geopotential heights, geostrophic wind fields, and distributions of potential vorticity (see for instance Section 3.2).

A global distribution of spectrally integrated radiances (840 to 855 cm^{-1} , see part of Figure 5) is shown in Figure 7 for the 18 km altitude level. The radiance distribution was measured on November 6, 1994 by using the stratospheric measuring mode (Mode 2, see Table 1). The radiance values are shown at the horizontal sampling grid of the instrument. The measuring tracks of the three telescopes can easily be identified in Figure 7. Each colored square represents a complete altitude scan in the altitude range from 15 km to 45 km with an altitude step of 1.5 km. The spectral interval from 840 to 855 cm^{-1} essentially represents CFC-11 in the lower stratosphere. There are some overlapping emissions of aerosol, HNO_3 , and ozone in this spectral region, however, only about 20 to 30% of the total. Since the influence of the atmospheric temperature field is moderate, structures in the CFC-11 radiance field are a proxy for structures in the CFC-11 mixing ratio field (unless atmospheric temperature variations become too large, i. e. in case of a minor warming).

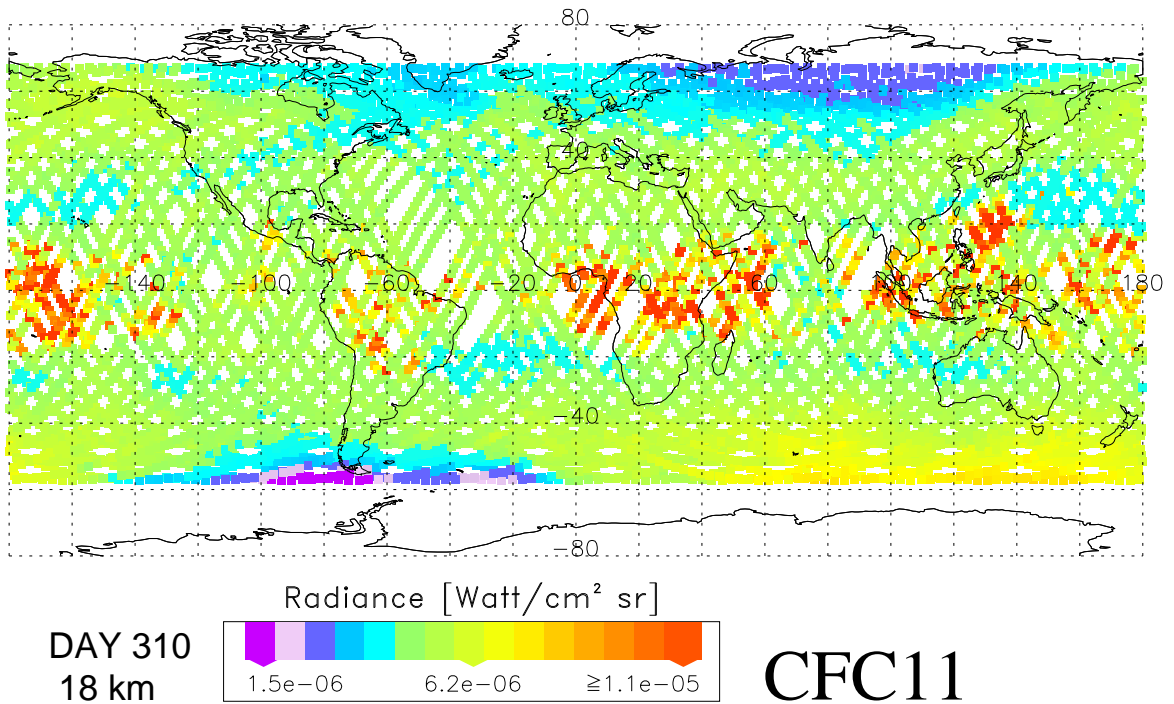


Figure 7: Horizontal distribution of CFC-11 limb-radiance values at 18 km altitude. The observations were made on November 6, 1994 by using measurement mode 2 (see Tab. 1). The map shown in this figure covers longitudes from 180°W to 180°E and latitudes from -80° to +80°. Each colored symbol represents a complete altitude profile (15 to 45 km).

In Figure 7, the elongated South Polar vortex is indicated by very low radiance values at the tip of South America. These low values are a result of considerable

downwelling and associated downward transport of CFC-11 poor air during the winter months. Vertical radiance profiles as well as corresponding retrieved CFC-11 values suggest a downward transport over ~ 5 km (*Riese et al.*, 1999a; *Spang*, 1997.) The distribution of Figure 7 also exhibits areas with relatively high radiation values in the equator region, centered around the Amazon, Congo, and Indonesia. These are areas of strong upwelling and deep convection. Another area of high radiation at the date line is consistent with convection patterns associated with an El Nino event (*Spang*, 1997). Analyses of corresponding spectra show that the high radiance values are not from CFC-11 emissions but probably from “subvisible” clouds (e. g. *Offermann and Spang*, 1998). During CRISTA-2, considerable (highly variable) polar stratospheric cloud cover was seen over Antarctica (*Spang et al.*, 2000).

Radiative transfer in the atmosphere

In order to retrieve atmospheric pressures, temperatures, and trace gas mixing ratios from the observed limb-radiance spectra, the radiative transfer equation has to be solved. For a limb-sounding emission-measuring instrument this equation is given by:

$$I_{\nu}^i(x_0 = 0) = \int_0^{\infty} k_{\nu}(x)\rho(x)J_{\nu}(x)\tau_{\nu}^i(x) dx \quad (1)$$

$$\tau_{\nu}^i(x) = \exp \left[- \int_0^x k_{\nu}(x')\rho(x') dx' \right] \quad (2)$$

$$\frac{\partial \tau_{\nu}^i(x)}{\partial x} = -k_{\nu}(x)\rho(x)\tau_{\nu}^i(x) \quad (3)$$

with:

ν	wavenumber of radiance
i	viewing direction index
I_{ν}^i	radiance received from viewing direction i
$k_{\nu}(x)$	absorption cross-section at location x
$\rho(x)$	number density at location x
$J_{\nu}(x)$	source function at location x
$\tau_{\nu}^i(x)$	atmospheric transmission between location x and the instrument ($x_0=0$)

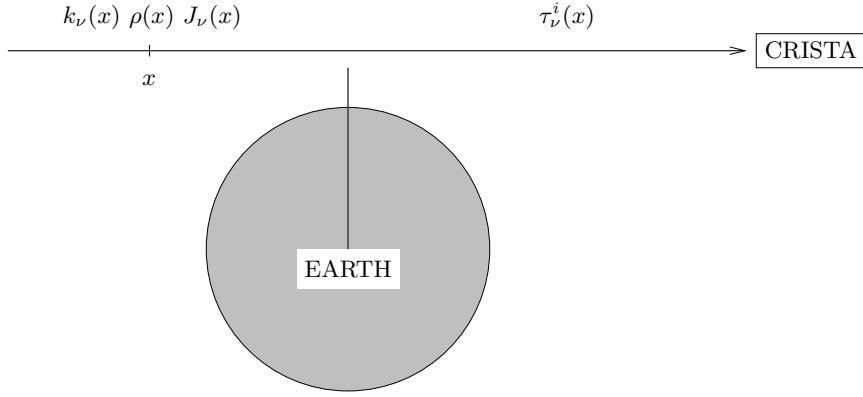


Figure 8: Radiative transfer in the atmosphere

The radiance contributions are accumulated along the line-of-sight (LOS) starting from the location of the instrument ($x_0=0$). The emission of the atmosphere at location x (see Figure 8) can be expressed as product of the source function $J_\nu(x)$, the absorption cross-section $k_\nu(x)$, and the atmospheric number density $\rho(x)$. The fraction of the emitted light received by the instrument is given by the atmospheric transmission between location x and the instrument ($x_0=0$).

Combining of Equation 1 and Equation 3 and assuming conditions of local thermodynamic equilibrium (LTE) yields:

$$I_\nu^i(x_0 = 0) = - \int_0^\infty B_\nu[T(x)] \frac{\partial \tau_\nu^i(x)}{\partial x} dx \quad (4)$$

$$I_\nu^i(x_0 = 0) = \int_0^\infty B_\nu[T(x)] \frac{\partial \epsilon_\nu^i(x)}{\partial x} dx \quad (5)$$

$$\epsilon_\nu^i(x) = 1 - \tau_\nu^i(x) \quad (6)$$

$$\partial \epsilon_\nu^i(x) / \partial x = -\partial \tau_\nu^i(x) / \partial x \quad (7)$$

with:

$B_\nu[T(x)]$	Planck function
$T(x)$	atmospheric temperature
$\epsilon_\nu^i(x)$	atmospheric emissivity between location x and the instrument ($x_0=0$)
$\partial\epsilon_\nu^i(x)/\partial x$	weighting function

To solve Equation 4 or Equation 5, the atmospheric path is usually divided into segments (e. g. Figure 4), each defined by suitable mean values of pressure, temperature, and trace gas mixing ratios. This allows for fast calculations of transmission changes (weighting functions) since the total transmission of multiple segments can be calculated by multiplying the single transmissions of the path segments.

Finally, the instrument spectral response function has to be taken into account by using a spectral integral:

$$R_\nu^i = \int_{\nu_1}^{\nu_2} g(\nu') I^i(\nu') d\nu' \quad (8)$$

with:

R_ν^i	Measured radiance received from direction i
$g(\nu')$	Spectral response function of the instrument
ν_1, ν_2	wavenumbers spanning the non-zero region of $g(\nu')$

The spectral response function $g(\nu')$ of CRISTA is given by the spectrometer function at the actual position of the grating during a spectral scan. The shape of the CRISTA spectrometer function can be readily approximated by a triangle function. For radiometric instruments such as LIMS or SABER, $g(\nu')$ represents a filter with a spectral bandpass of typically 50 cm^{-1} width. For interferometers such as MIPAS or TES, $g(\nu')$ accounts for the apodized instrument line shape (AILS).

The most accurate solutions of Equation 1 are obtained by calculating high resolution absorption cross-sections by means of a line-by-line (lbl) model. Such models account for the contributions of all molecular lines near (30 cm^{-1}) the considered wavenumber point:

$$k_\nu(x) = \sum_j S^j [T(x)] f_\nu^j [T(x), P(x)] \quad (9)$$

with:

$k_\nu(x)$	absorption cross-section at location x
ν	wavenumber of radiance
f_ν^j	line shape function
$S^j(T)$	line intensity
j	line index
$T(x)$	atmospheric temperature
$P(x)$	atmospheric pressure

To simulate atmospheric spectra, absorption cross-sections $k_\nu(x)$ have to be calculated for a rather fine wavenumber grid (typically 1/5 of the line width) and a large number of atmospheric path segments along the line-of-sight (see Figure 4).

The CRISTA fast forward radiance model

During its two missions, CRISTA measured about 95,000 height profiles of limb-radiance spectra. This number matches the number of profiles obtained from a sun occultation instrument (such as HALOE) during an operational period of about seven years. The resulting large amount of radiance data requires extremely fast retrieval algorithms. The standard CRISTA forward radiance model is therefore based on approximate (but accurate) techniques to solve the radiative transfer equation.

The calculations of high resolution cross-sections represents a major (time consuming) problem for any instrument receiving radiation from large spectral regions (e. g. *Riese*, 1999c; 1999d). For this reason, the retrieval schemes planned for MIPAS utilize only a small fraction of the spectral range covered (so-called micro-windows). For radiometers such as LIMS and SABER a restriction to narrow spectral regions is not possible. The time consuming integration over $d\nu'$ (Eq. 8) has to be performed in order to account for the broadband filter functions. Since detailed lbl calculations are too time consuming for the retrieval of all radiance data gathered by radiometers, approximate forward models have been developed to address this problem (e. g. *Gordley and Russell*, 1981). These models utilize pre-calculated emissivity lookup tables, which already include the spectral integration of Equation 8. The non-monochromatic tables are calculated for homogeneous cells by means of detailed lbl calculations for all realistic atmospheric conditions of pressure, temperature, and mass paths U :

$$\bar{\epsilon}_\nu(U, T, P) = \int_{\Delta\nu} g(\nu') \epsilon_\nu(U, T, P) B_\nu(T) d\nu' / \bar{B}_\nu(T) \quad (10)$$

$$\bar{B}_\nu(T) = \int_{\Delta\nu} g(\nu') B_\nu(T) d\nu' \quad (11)$$

$$\bar{\epsilon}_\nu(U, T, P) = 1 - \bar{\tau}_\nu(U, T, P) \quad (12)$$

with:

U mass path
 T cell temperature
 P cell pressure

The pre-calculated tables can be used to perform radiative transfer calculations in a non-monochromatic formulation of Equation 5. However, the calculation of the weighting function (Eq. 7) is somewhat more complicated than in a monochromatic formulation since the combined transmission of several path segments cannot be calculated just by multiplying the single segment transmissions. For this reason emissivity growth approaches have been developed to accumulate the broadband radiance contributions of segments along the line-of-sight (see Figure 4). These methods are known as pseudo-mass approximation and Curtis-Godson approximation (CGA) [e. g. *Marshall et al.*, 1994].

The spectral resolution of CRISTA is considerably better than those of radiometers. However, the retrieval involves large spectral regions comparable to the spectral bandwidth of radiometers (and typically a factor 20 broader than the MIPAS micro-windows). In addition, the high measuring speed of the four simultaneously operating spectrometers results in a large amount of radiance data having to be inverted. The CRISTA forward model is therefore based on the approximate methods originally developed for radiometric applications. In particular, the formalism has been adapted to the details of the CRISTA spectroscopy: the radiance that enters a CRISTA spectrometer is chopped, collimated, and directed to the diffraction grating, which resolves the incoming spectrum of light, and afterwards focuses it on 5 to 8 parallel detector channels, depending on the spectrometer. A spectral scan (1.15 s) is performed by

tilting the diffraction gratings of all spectrometers simultaneously. The integration time of the electronics is on the order of 4.5 ms (chopper period), which means the spectral range of each detector channel is sampled by about 250 measurement points while the grating is scanning over it. This results in a wavenumber increment between two subsequent spectral measurement points of about 1/6 of the spectral resolution. Emissivity lookup tables have been calculated by means of the LINEPAK lbl code (*Gordley et al.*, 1994) for all spectral sampling points by accounting for the spectrometer function $g(\nu')$ at each point. The lookup tables are used in conjunction with the BANDPAK libraries (*Marshall et al.*, 1994) to calculate the radiance that enters the CRISTA detectors. BANDPAK offers a number of options to use non-monochromatic emissivity tables in an emissivity growth approach to accumulate the radiance contributions of the segments of the line-of-sight (Figure 4). For CRISTA an option is used that provides a method to calculate an average result from PMA (pseudo-mass approximation) and CGA (Curtis-Godson approximation).

The CRISTA forward model allows rapid calculations of complete limb-radiance spectra at the spectral resolution of the instrument, which agree to within 1% with detailed line-by-line calculations for most of the applications. Compared to detailed lbl calculations the number of spectral frequency points required for the calculation of the radiative transfer is reduced by factors of 100 to 1000. Figure 9a shows a comparison of a measured (solid line) and a simulated (dashed line) spectrum for the strong $15 \mu\text{m}$ bands of CO_2 at 75 km altitude. The CO_2 emission at $15 \mu\text{m}$ is used to derive pressure and temperature distributions of the upper stratosphere and mesosphere based on a two color method (*Riese et al.*, 1999a). The accuracy (2K) and the precision (1K) of the results obtained for CRISTA are comparatively high and, for instance, allows the first calculations of geostrophic wind fields in the mesosphere to be made from observations on a daily basis.

Figure 9b shows a comparison between an observed spectrum and a simulated spectrum for the channel at $12.6 \mu\text{m}$, which is used for the stratospheric temperature retrieval. In this case, the retrieval is performed simultaneously with the retrieval of ozone, chlorine nitrate (ClONO_2) and aerosols, since significant interferences of these trace gases occur in the spectral range of the CO_2 emission. In addition, background emissions of HNO_3 and CCl_4 are taken into account. The contributions of interfering gases are also shown in Figure 9b. Figure 9 demonstrates that the details of the

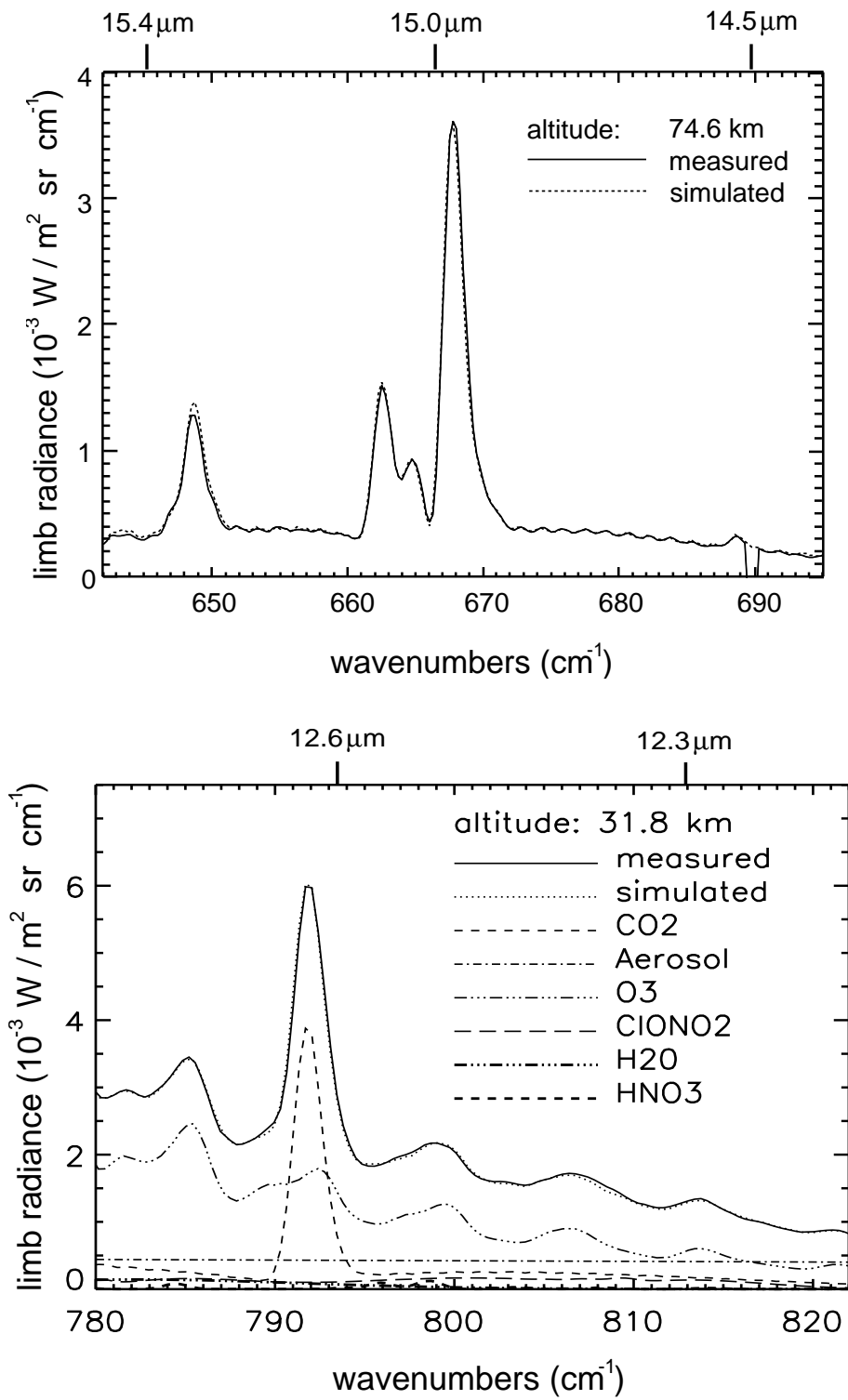


Figure 9: Comparison of a measured and a simulated limb-radiance spectrum for detector channel SCL2 at a tangent height of 74.6 km (upper panel, Figure 9a) and for detector channel SCS6 at a tangent height of 31.8 km (lower panel, Figure 9b). For details see text.

CRISTA spectra can be accurately modeled by the approximate forward model.

The CRISTA onion-peeling retrieval algorithms

For limb-viewing instruments such as CRISTA, the retrieval of atmospheric temperature and trace gas fields can be performed with simple onion-peeling schemes (e. g. *Russell and Drayson, 1972*). The approximate CRISTA forward model (see above) is the basis of a multiple-emitter multiple-spectral sampling point onion-peeling retrieval algorithm (*Riese et al., 1997; 1999a*). The inversion of the limb-radiance spectra starts at the uppermost tangent height (see Figure 4) and proceeds to lower tangent heights by taking into account the retrieved values at the levels above. Thus, the temperature value and the trace gas number densities of the line-of-sight segment immediately above the tangent point (see Figure 4) have to be adjusted in order to simulate the measured limb-radiance spectra at a given tangent height. Fast convergence is achieved by calculating the partial derivatives (Jacobians) of the simulated radiance values from the temperature and/or trace gas mixing ratio at every iteration step and by using these quantities for the next update.

In most of the measurement modes, the tangent points of the radiance spectra of the individual profiles are separated by about 1.5 km in the vertical (CRISTA-1). For stability reasons, the inversion to geophysical parameters is performed on two profiles (vertical spacing 3 km, offset 1.5 km). These two profiles are then recombined to produce inverted profiles at 1.5 km spacing (*Riese et al., 1999a*). The temperature (and pressure) retrieval has to be performed first. After this, trace gas mixing ratios can be derived from the observed spectra. Since no information from one profile retrieval enters the retrieval of another profile, horizontal structures are resolved as far as possible for a limb-sounding instrument.

The spectral resolution of CRISTA is sufficient to retrieve mixing ratios of weakly emitting trace gases such as chlorine nitrate (ClONO₂). A retrieved distribution of ClONO₂ at 46.5 mbar (21 km) is shown in Figure 10. The ability of CRISTA to provide valuable information about coherent medium- and small-scale structures in atmospheric trace gas distributions is clearly demonstrated in Figure 10.

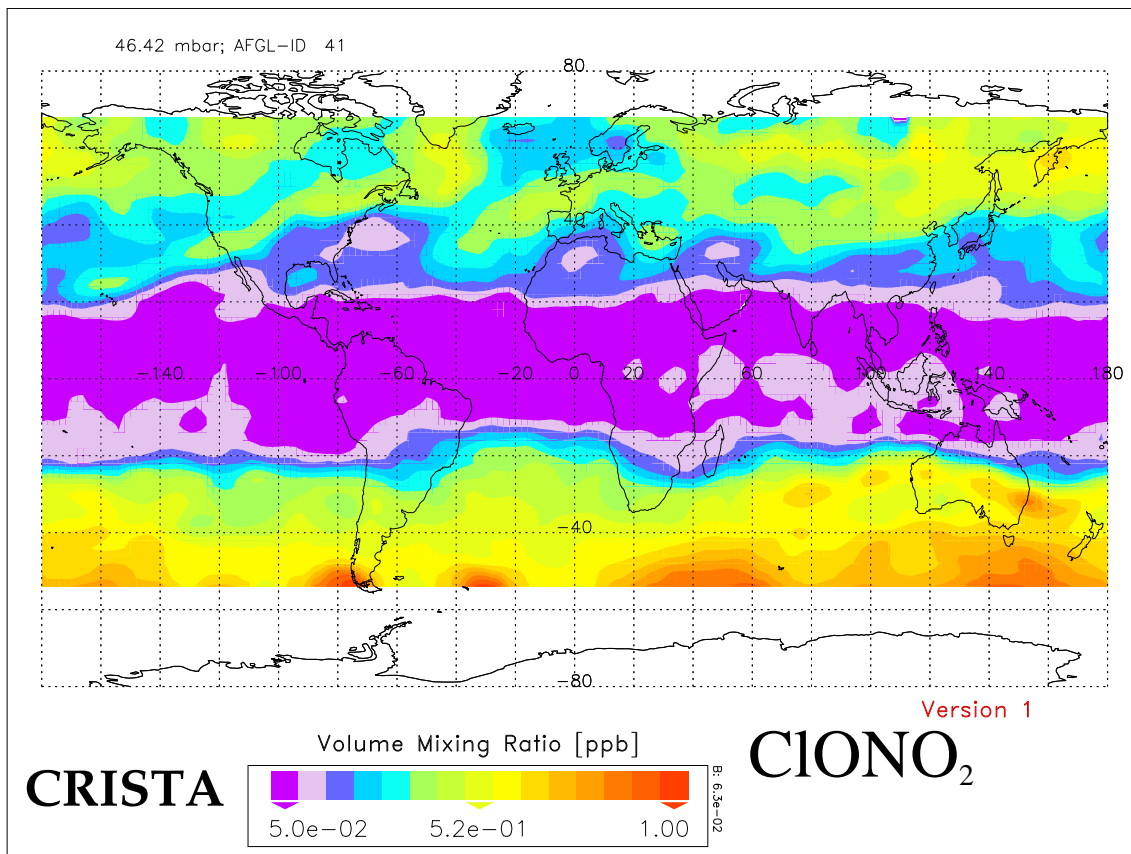


Figure 10: Mixing ratios of ClONO₂ measured by CRISTA on November 6, 1994 at 21 km altitude. The field was obtained by interpolating the CRISTA data onto a regular grid (3° x 1.5°, longitude x latitude) by using a horizontal filter with a half width of 8° in longitude and 4° in latitude. Daytime measurements have been used as well as nighttime measurement.

2.5 Synoptic mapping of measured trace gas fields

The CRISTA retrieval yields asynoptic temperature and trace gas fields on an instrument sampling grid (level 2 data). However, theoretical studies often require interpolation of asynoptic satellite data to a common time and to a regular spatial grid (level 3 product). Well-established mapping methods include spectrally-based, Kalman-filtering approaches (e. g. *Rodgers et al.*, 1976) and Fourier synoptic mapping techniques (*Salby et al.*, 1982a, b). Trajectory mapping techniques based on observed wind fields (e. g. *Morris et al.*, 1995) represent an attractive alternative to spectrally based approaches, since they use a physically-based model to describe the data time behaviour. Recently, trace gas assimilation into chemical transport models has been used to generate synoptic maps from asynoptic limb-viewing measurements (e. g. *Riese et al.*, 1999b).

In the standard data processing of CRISTA, a Kalman filter (*Ern*, 1995) is used which estimates amplitudes and phases of sinusoidal waves around the latitude circles in order to interpolate asynoptic level 2 data (instrument sampling grid) to synoptic grids (level 3 product). Zonal wavenumbers up to $m=15$ are used for the Kalman filter. In addition, *Bacmeister et al.*, (1999) have developed an isentropic trajectory mapping method for intercomparisons of CRISTA ozone, CFC-11, and NO_y observations with aircraft observations of NASA's ER-2 carried out at the end of the airborne measurement campaign known as Airborne Southern Hemisphere Ozone Experiment and Measurements to Assess the Effects of Stratospheric Aircraft (ASHOE/MAESA).

Due to the high data density CRISTA trace gas fields are especially suited for mapping techniques based on trace gas assimilation. CRISTA synoptic maps of long-lived tracers have therefore been generated by means of a sequential trace gas assimilation method which has been developed for quantitative analyses of trace gas transport and mixing processes (*Riese et al.*, 1999b). The assimilation system combines the asynoptic CRISTA observations with results from a chemical transport model (CTM). It provides synoptic trace gas maps, which are consistent with the asynoptic CRISTA measurements at the time steps of the model (20 min). Details of the technique are given in Section 5.

A comparison of measured and analyzed CFC-11 distributions is shown in Figure 11 for the period November 6 to November 10 and the 46.4 mbar pressure level.

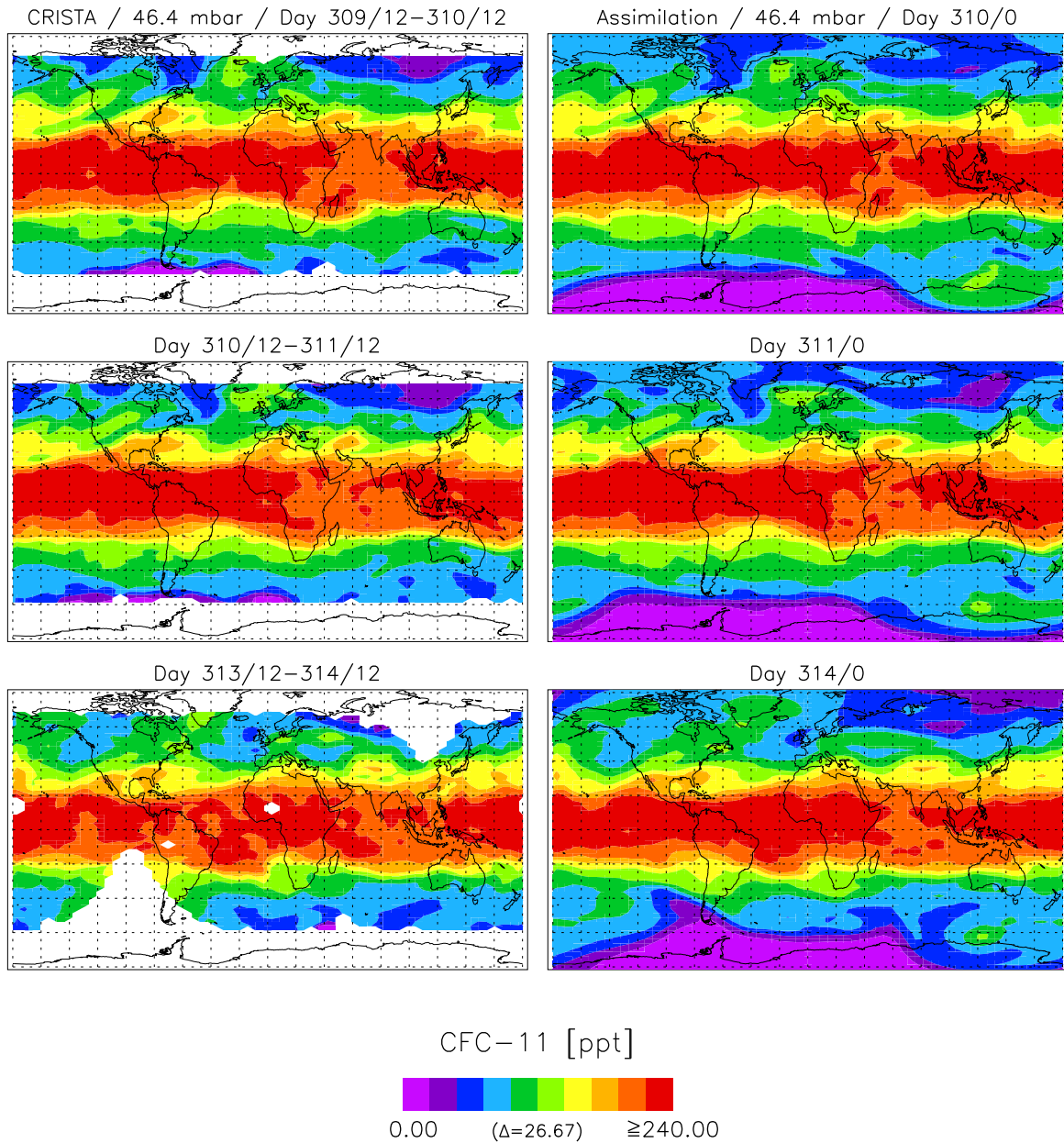


Figure 11: Comparison of measured and assimilated CFC-11 values at 46.4 mbar for November 6, 7, and 10, 1994. The measurements of each map were taken over a time period of 24 hours, while the assimilated distributions represent synoptic maps (0000 UT). Note that the horizontal density of the measured data of day 314 (November, 10) is about a factor of two lower than on days 310 and 311 (November 6, and 7, 1994). This is not apparent in the filtered data shown in this plate. Blank areas indicate regions, where no measurements are available

The analyzed maps represent synoptic distributions of CFC-11 for 0:00 GMT each day, while the measured data corresponding to each map were gathered over a time span of 24 hours. The figure demonstrates that model predictions successfully fill in temporal gaps. This applies, for example, to large data gaps occurring on the last two days of the time sequence. These gaps are filled in the analyzed distributions by means of the model forecast which is based on previous observations.

Synoptic trace gas fields are especially suited for studies of the temporal development of large-scale and medium-scale dynamical structures. In Figure 11 very interesting tropical extrusions occur at latitudes around 30°N, shaped like Kelvin Helmholtz billows. The billows resemble ClONO₂ structures at 30°N shown in Figure 10. The CRISTA measurements represent the first global observation of such dynamical features. They are theoretically predicted by *Shepherd et al.*, (2000) based on a theory of chaotic advection in the stratosphere, which is primarily controlled by the large-scale low-frequency component of the flow. The billows are most pronounced on November 6 and 7. The tropical extrusion on the east coast of the USA is quite stationary, while some eastward movement of the less pronounced billows in the west Asian area can be seen. In addition, these more transient features start to dissolve on November 14.

The analyzed (assimilated) maps of Figure 11 represent a value-added level 3 data product of CRISTA. The presentation of the synoptic evolution of trace gas fields is an important feature of the assimilated data product. However, the combination of measured trace gas fields of high spatial resolution data with a chemical transport model provides many more advantages, which will be discussed in Section 5 in terms of quantitative studies of atmospheric transport and photochemical processes.

2.6 Data validation

Validation by correlative in-situ measurements

Major elements of the two CRISTA missions were the CRISTA/MAHRSI validation campaigns. During these campaigns correlative measurements were performed with ground-based systems, balloons, and rockets (GBR campaigns).

A major objective of the CRISTA/MAHRSI campaigns was the validation of CRISTA temperature measurements, since atmospheric temperatures represent an essential input for the retrieval of trace gas mixing ratios from limb-radiance spectra. In particular, validation of the mesospheric temperatures derived from $15\mu\text{m}$ is important, since CRISTA provides the first global data set with high accuracy in the mesospheric region. Special features of the second mission were so-called zero miss distance / zero miss time comparisons (*Lehmacher et al.*, 2000), where the maneuver capabilities of the CRISTA-SPAS satellite were used to point the viewing direction of CRISTA at selected validation sites (zero miss distance). In addition, the launches of balloons and rockets were coordinated with the satellite overflights in order to obtain zero miss time comparisons.

The NASA/GSFC Wallops Flight Facility (WFF) was the main site for validation of CRISTA temperature measurements. Falling sphere and data sonde rocket launches were performed. During CRISTA-2, falling spheres were launched in pairs within a few minutes of each other to obtain coincident measurements at two different altitudes. An example of a zero miss distance / zero miss time comparison of two falling spheres and CRISTA-2 temperature observations is sketched in Figure 12. Shown is the location of the measurement points (center telescope) of three adjacent CRISTA vertical profiles of the validation orbit. The profiles are separated by about 290 km. The small V-shaped line originating from the coast represents the trajectories of two falling spheres. The CRISTA profile closest to WFF can be considered as a zero miss distance profile, since the width of the horizontal weighting function of the limb-viewing method is on the order of 200 km.

The temperature profiles for both falling spheres and the zero miss distance profile of CRISTA are shown in Figure 13. They agree with each other to within the estimated statistical error of the falling spheres (about 3-4 K at these altitudes) [*Lübken et al.*,

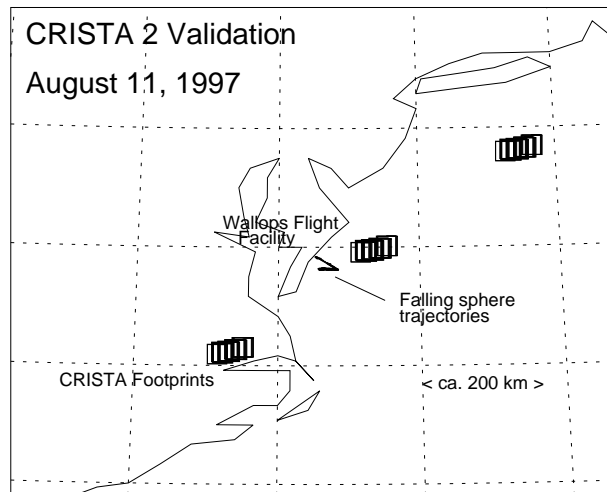


Figure 12: Details of the validation orbit on August 11, 1997. CRISTA footprints at different altitude points (open squares) are shown for three subsequent profiles measured by the SCL spectrometer. It can be seen that all tangent points of the individual CRISTA profiles were measured at about the same horizontal location (latitude, longitude). The profiles are therefore almost straight upward. The projection on the horizontal plane of the trajectories of two falling spheres is also shown (V shaped line).

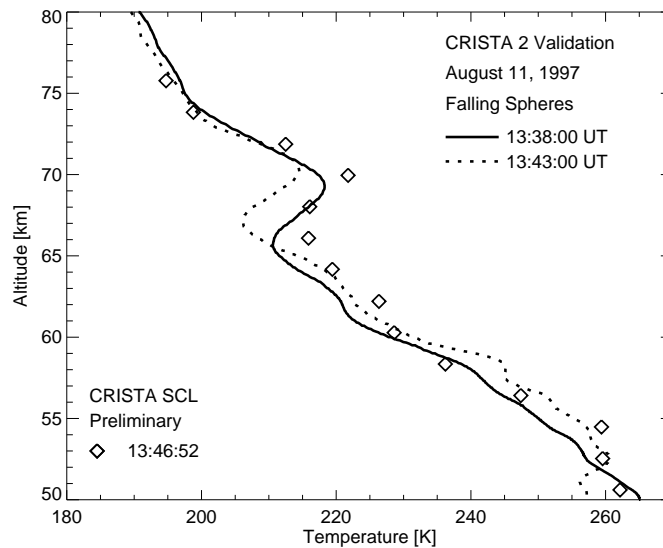


Figure 13: Temperature profiles of two falling spheres (solid and dotted lines) and the corresponding zero miss distance CRISTA SCL temperature profile (diamonds). Note that CRISTA temperatures are preliminary (non-version) data (Figure 4 of *Lehmacher et al.* 2000).

1994; Schmidlin *et al.*, 1991]. The data suggest relatively high variability, especially in the vicinity of an observed temperature inversion between 65 and 70 km. The variability is remarkable, considering that the temperatures were measured within 5 minutes. CRISTA temperatures agree well with the falling sphere observations. The inversion layer clearly shows up in the CRISTA profile, suggesting that the horizontal extent of this feature must have been at least on the order of the horizontal weighting function of CRISTA.

Validation based on satellite data

Validations based on comparisons with *in situ* instruments often pose problems due to the large atmospheric variability which is not accounted for by the limited spatial and temporal coverage of the GBR observational systems. This disadvantage can be avoided by comparisons with other satellites. Such comparisons also allow the detection of latitude-dependent effects. The first flight of CRISTA took place during the ATLAS-3 mission of NASA (*Kaye and Miller*, 1996). CRISTA-1 observations were carried out simultaneously with measurements of five other ozone sensors, one emission experiment (MLS) and four occultation experiments (ATMOS, HALOE, SAGE II, POAM II). Figure 14 shows a comparison of ozone values of the different sensors based on equivalent latitude/potential temperature (Eql/Θ) mapping (*Manney et al.*, 2000). The comparison shows excellent agreement (typically better than 0.5 ppm) of the ozone values in the altitude region below 655 K, where dynamics dominates. Good agreement is also found in the upper stratosphere, where chemistry dominates. The most notable differences occur in the middle stratosphere where both chemistry and dynamics are important. In the middle stratosphere of the southern hemisphere, the occultation instruments provide about 30 % lower values than CRISTA and MLS. These differences can be largely explained by differences in sampling in conjunction with a low ozone pocket sampled by the occultation instruments (*Manney et al.*, 1995).

The ozone comparison shown in Figure 14 is especially meaningful due to the large number of sensors. Other trace gases such as N_2O , CH_4 , and CFC-11 were measured only by CRISTA and ATMOS or HALOE. For these trace gases comparisons were made based on coincident observations. In general, good agreement (5% to 20 %) was obtained (for CRISTA version 3 data).

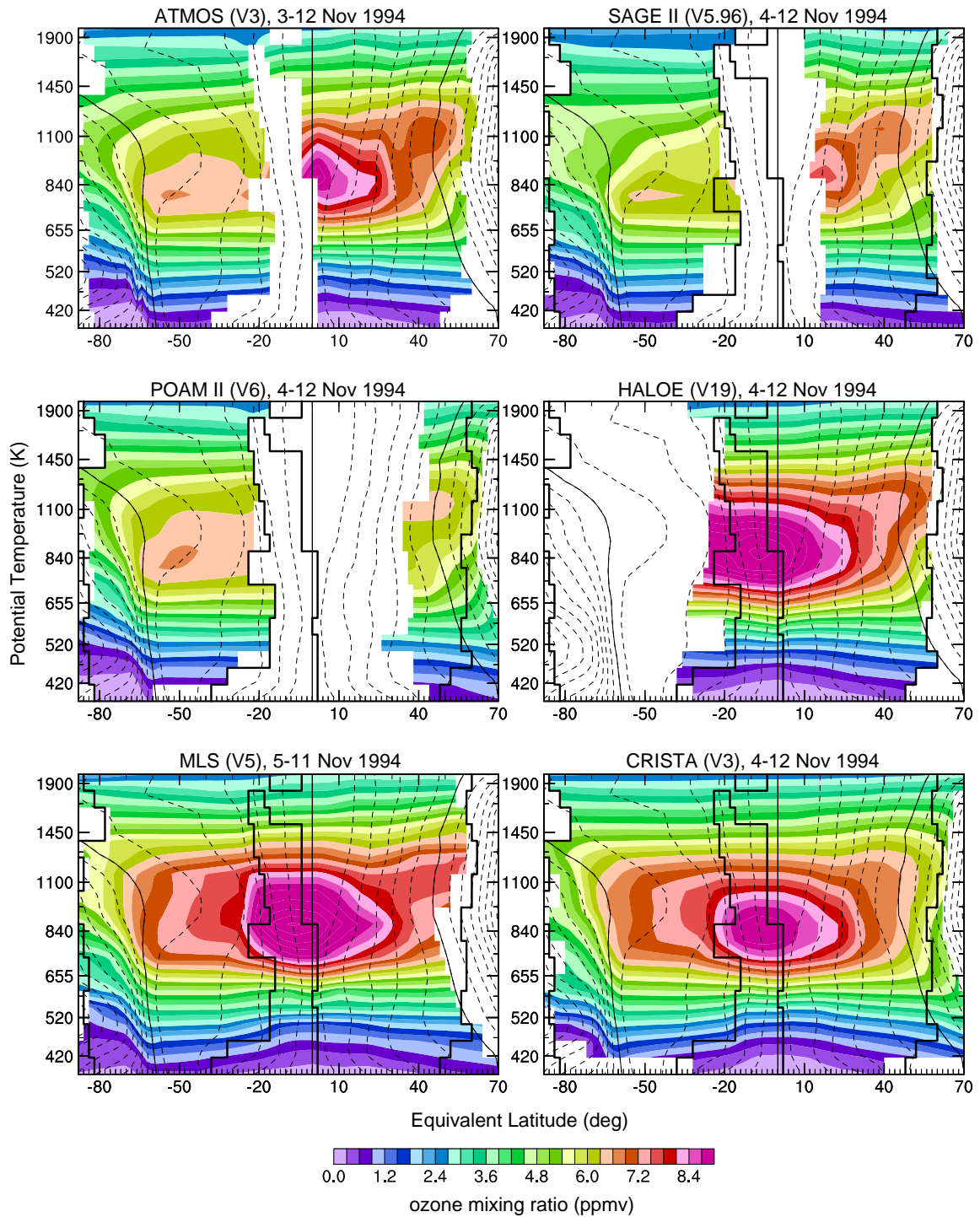


Figure 14: Eql/ Θ mapped ozone values of six instruments operated during ATLAS-3. Scaled PV contours (see *Manney et al.*, 1994) are overlaid (dashed lines). The solid contour line at high latitudes indicates the vortex edge. (Figure 1 from *Manney et al.*, 2000).

In addition to direct comparisons with other instruments, scientific analyses represent a powerful tool for validating satellite data sets. Three-dimensional model simulations with chemical transport models (and data assimilation) are starting to play an important role, i. e. for the validation of the capability of satellite instruments to resolve chemical and dynamical structures. Models do not necessarily completely predict the atmospheric state, but they can provide guidelines for dynamical and chemical structures to be expected from the observation. Such analyses are presented in Sections 4 and 5.

3 Dynamical processes observed by CRISTA

Dynamical processes play an important role in the atmospheric system. For example, the climatological distribution of ozone is largely influenced by poleward transport of ozone produced in the equatorial source region. A detailed description of atmospheric dynamics (e. g. *Andrews et al.*, 1987; *Brasseur et al.*, 1999) is beyond the scope of this work. This section presents a few dynamical features observed by CRISTA such as atmospheric waves (Section 3.1) and transport processes (Sections 3.2 and 3.3). Atmospheric waves such as planetary waves, gravity waves, and tidal oscillations play an important role in the dynamics of the atmosphere, e. g. in the mean circulation. Vertically propagating waves generated in the troposphere provide, for example, a large fraction of eddy momentum and heat fluxes in the middle atmosphere (*Holton*, 1975). A detailed understanding of wave sources, wave propagation, and interactions with the background flow (and other waves) is therefore crucial for the description of the atmospheric system. Planetary waves drive the mean meridional circulation in the stratosphere and at the same time facilitate quasi-horizontal trace gas transport. CRISTA observations suggest that narrow tongues of tropical and polar air frequently occur in the stratospheric surf zone and significantly contribute to the exchange of tropical and extra-tropical air. In the equatorial stratopause region circulation cells arising from inertially unstable conditions appear to play a significant role in tracer transport.

3.1 Atmospheric waves

Thermal tides

A basic source of tidal theory is *Chapman and Lindzen*, (1970). Well-known tidal features are, for example, diurnal migrating solar tides generated by periodic absorptions of solar radiance, primarily UV absorptions of ozone in the stratopause region and IR absorptions of H₂O in the troposphere. Migrating tidal waves follow the westward movement of the sun. Since the zonal wavenumber is equal to the number of oscillations per day, the phase at a given latitude depends only on the local solar time (LST).

Tidal waves in the upper atmosphere have been studied for more than 30 years

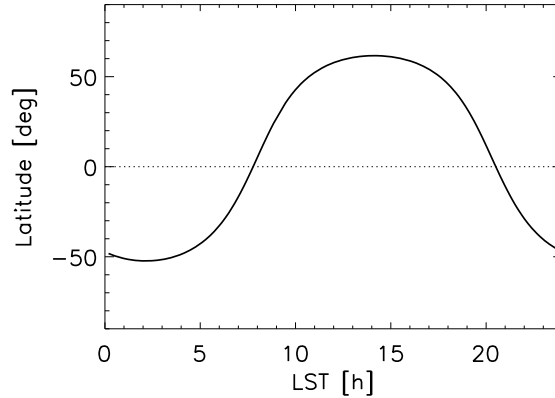


Figure 15: Local solar time distribution (LST) of the center telescope at points around an orbit for November 9, 1994. The LST shifts 22 minutes per day.

using, for instance, data from meteorological rockets. First global analyses of tidal signatures in atmospheric temperature fields were obtained from measurements of the Limb Infrared Monitor of the Stratosphere instrument (LIMS) on the Nimbus 7 satellite (*Gille and Russell, 1984*). *Hitchman and Leovy (1985)* report structures in day/night temperature differences consistent with the (1,1) mode of the migrating diurnal tide, i.e. maximum amplitudes at equatorial and middle latitudes. Recently the amount of wind data has significantly increased due to observations carried out by the Wind Imaging Interferometer (WINDII) (*Shepherd et al., 1993*) and the High Resolution Doppler Imager (HRDI) (*Hays et al., 1991*) on the Upper Atmosphere Research Satellite (UARS).

CRISTA temperature observations also exhibit significant tidal signatures (*Ward et al., 1999*). The observations provide an opportunity to examine the structure of tidal waves throughout the middle atmosphere with extended vertical coverage and improved accuracy at upper mesospheric heights. For analyses of tidal oscillations it is especially important to consider the local solar time (LST) distribution of the observations. Figure 15 shows the local solar times for the center telescope at points around an orbit for November 9, 1994 (Day 313). In the equatorial region, measurements at the ascending portion of the orbit are taken at 8 LST. Measurements at the descending portion are taken at 20 LST. Although the LST variation during the first mission is too small for a comprehensive spectral analysis, some tidal features are captured due to the LST differences between the ascending and the descending portion of each orbit. These differences are on the order of 12 hours for most of

the latitudinal band covered by CRISTA-1 (see Figure 15). Figure 16 (left panel) shows zonally averaged temperature differences (ascending minus descending part of the orbit) for November 9, 1994. The most apparent feature is the vertical pattern of alternating temperature minima and maxima at the equator and at middle latitudes. This pattern is characteristic of the (1,1) Hough mode and representative for the first symmetric propagating diurnal tide (*Forbes, 1982*).

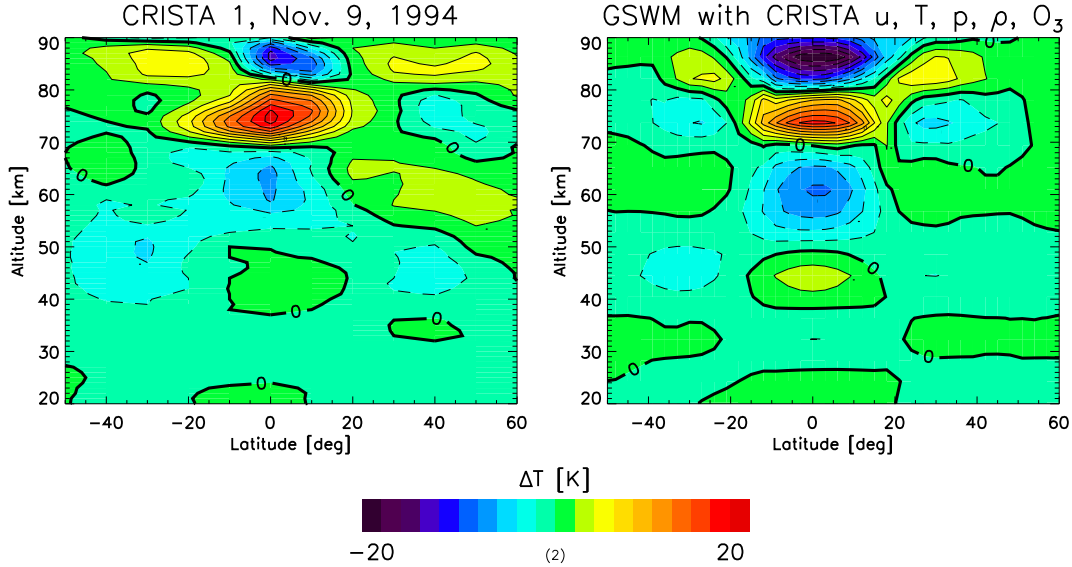


Figure 16: Latitude/height plot of zonal mean temperature differences for November 9, 1994 (left panel). The differences were calculated from zonal mean temperatures obtained from observations during the ascending and descending part of each orbit. The observations are compared to corresponding results obtained from the updated Global Scale Wave Model (right panel). (Plate 2 of *Oberheide et al., 2000*).

The main tidal structure observed by CRISTA is also present in a corresponding distribution of the Global Scale Wave Model (GSWM) (*Hagan et al., 1995*) calculated for the same LST but equinox conditions (*Ward et al., 1999*). *Oberheide et al., 2000* investigated sources of the remaining differences. In particular, the climatological background fields (e. g. winds, temperatures, and ozone) used in the GSWM-95 calculation were updated by background fields derived from CRISTA observations. In addition, revised tidal heating and dissipation schemes were included in the model, which represent early November conditions. The most significant changes are associated with the updated geostrophic background winds, which are in geostrophic balance with the CRISTA temperatures, and the improved gravity wave stress parametrization in the model. The results of the updated model are shown in the right panel of

Figure 16. Modeled and observed tidal phases match within one hour at the equator, amplitudes agree within 1K for most altitudes. However, the model still does not reproduce the decreasing tidal amplitude above 80 km, probably due to an underestimation of the equatorial gravity wave drag in the upper mesosphere.

As shown in Figure 16, temperatures measured by CRISTA-1 exhibit pronounced tidal structures, which can be well described by the linear theory as implemented in the Global Scale Wave Model. In contrast to this finding, the temperature distribution measured during the second CRISTA flight shows strong non-linear interactions between the tides and pronounced planetary waves. Since these non-linear interactions cannot be studied with the linear GSWM, future investigations will be based on the interactive non-linear ROSE model with appropriate lower boundary forcing.

Planetary Waves

Planetary waves are of great importance for the large-scale behaviour of the middle atmosphere (e. g. *Brasseur et al.*, 1999). They result from the latitudinal potential vorticity gradient (e. g. *Andrews et al.*, 1987). Fundamental work on the theory of tropospherically forced waves propagating into the middle atmosphere was performed by *Charney and Drazin*, (1961). A review of traveling planetary waves is given, for example, by *Salby* (1984).

During CRISTA-2 pronounced traveling planetary waves were observed in the southern hemisphere at mid-latitudes in the temperature field between 16 and 80 km. For example, a highly excited planetary wave-two was found with a period of about 12.5 days and a vertical wavelength of about 45 km (*Ward et al.*, 2000). Figure 17 shows the amplitude and the phase of this wave-two as a function of latitude and height for the geopotential perturbation field. The vertical and equatorward propagation of the wave-two signature extends into the mesosphere. Non-linear interactions with the tidal waves mentioned in the previous section are to be expected over a wide range of altitudes and will be investigated in future studies.

In addition, the CRISTA-2 planetary wave observations provide an opportunity to study the relationship between temperature and trace gases such as ozone. The relative phase of the signature in temperature and ozone varies with height (Figures 18 and 19). Below ~ 30 km temperature perturbations are in phase with ozone perturba-

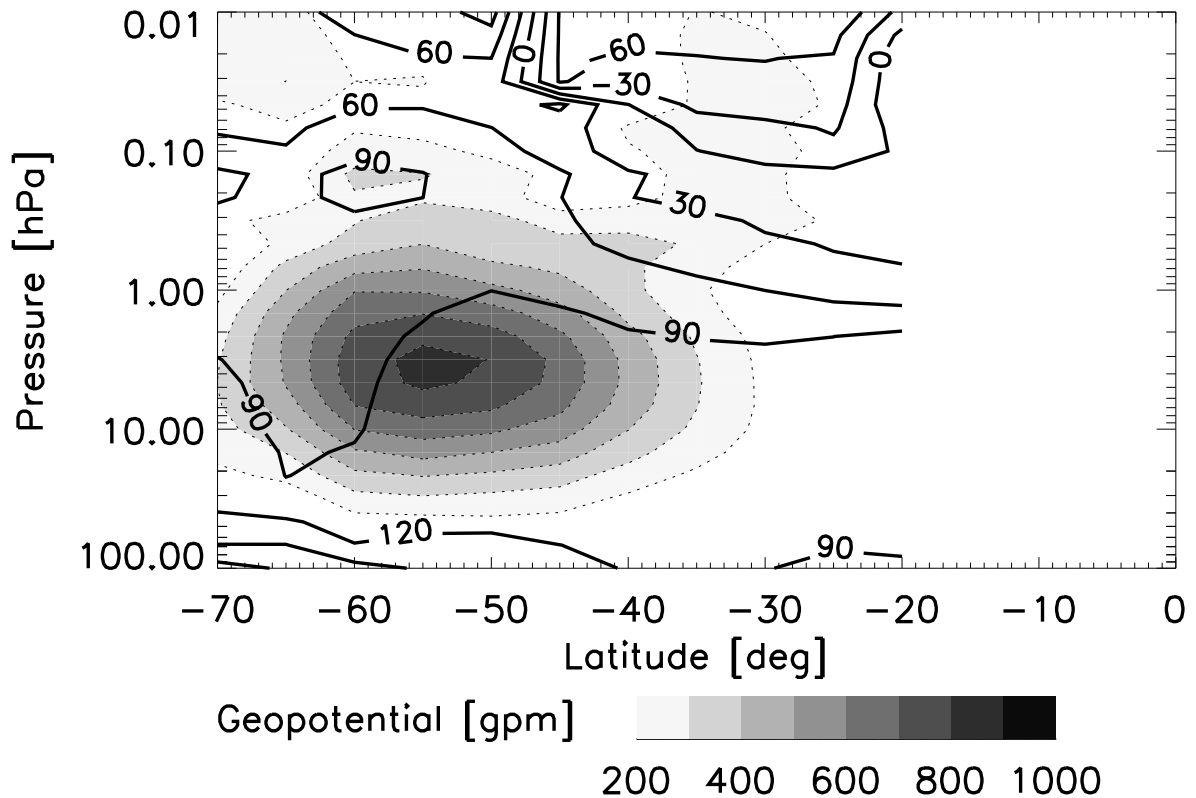


Figure 17: Wave-two geopotential perturbation field (*Oberheide*, dissertation in preparation). The amplitude is shown by a grey scale map and the phase is superimposed by solid black contour lines. The contour lines indicate the longitude at which the maximum amplitude occurred on August 9, 1997.

tions, since ozone is dynamically driven. The perturbations are out of phase at higher altitudes (above 40 km), where photochemistry dominates. *Ward et al.* (2000) point out that the CRISTA results above the middle stratosphere show a better agreement with photochemical equilibrium calculations than previous analyses. Future analyses will address the question whether this good agreement is due to better data quality or due to the particular dynamical conditions encountered during CRISTA-2. In addition, the temperature/ozone correlation will be investigated by three-dimensional modeling. The synergetic use of CRISTA-2 observation and results from model simulations should also allow for detailed studies of the dependence of ozone losses on different catalytic cycles (e. g. *Smith*, 1995).

Gravity Waves

Gravity waves (GW) drive large-scale circulation patterns, predominantly in the mesosphere and lower thermosphere. A review of middle atmosphere GW theory is given,

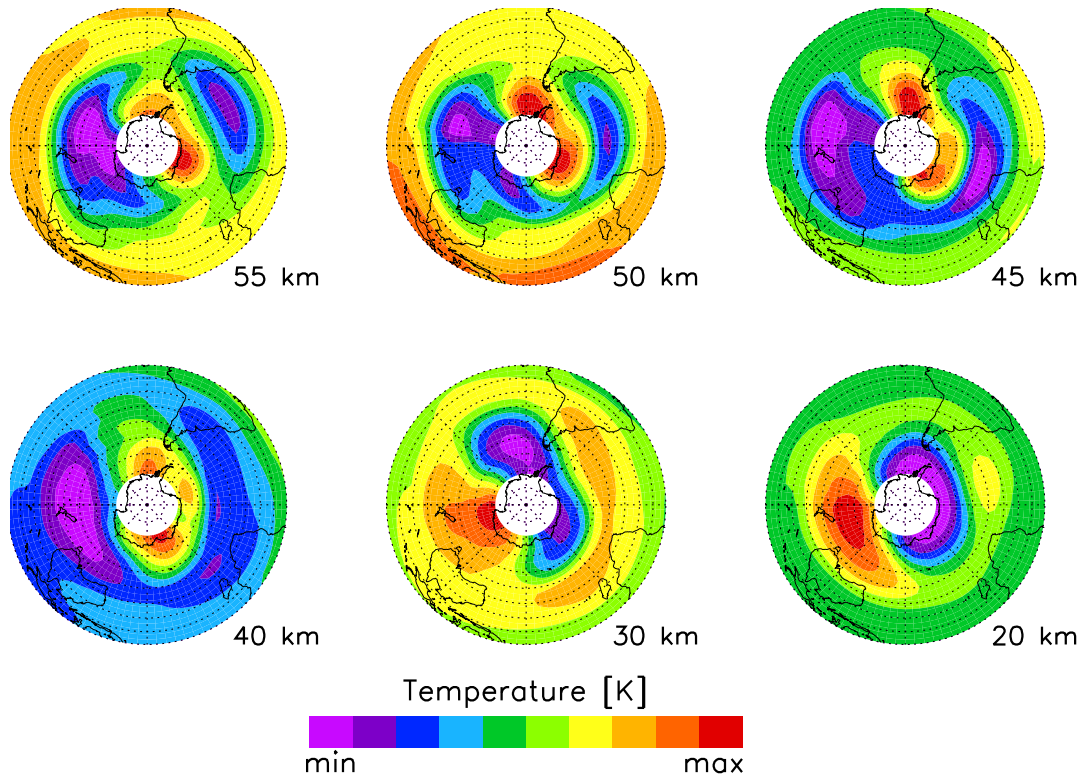


Figure 18: Polar view of CRISTA-2 temperature fields in the southern hemisphere at various altitude levels. (Figure 4 of *Ward et al.*, 2000).

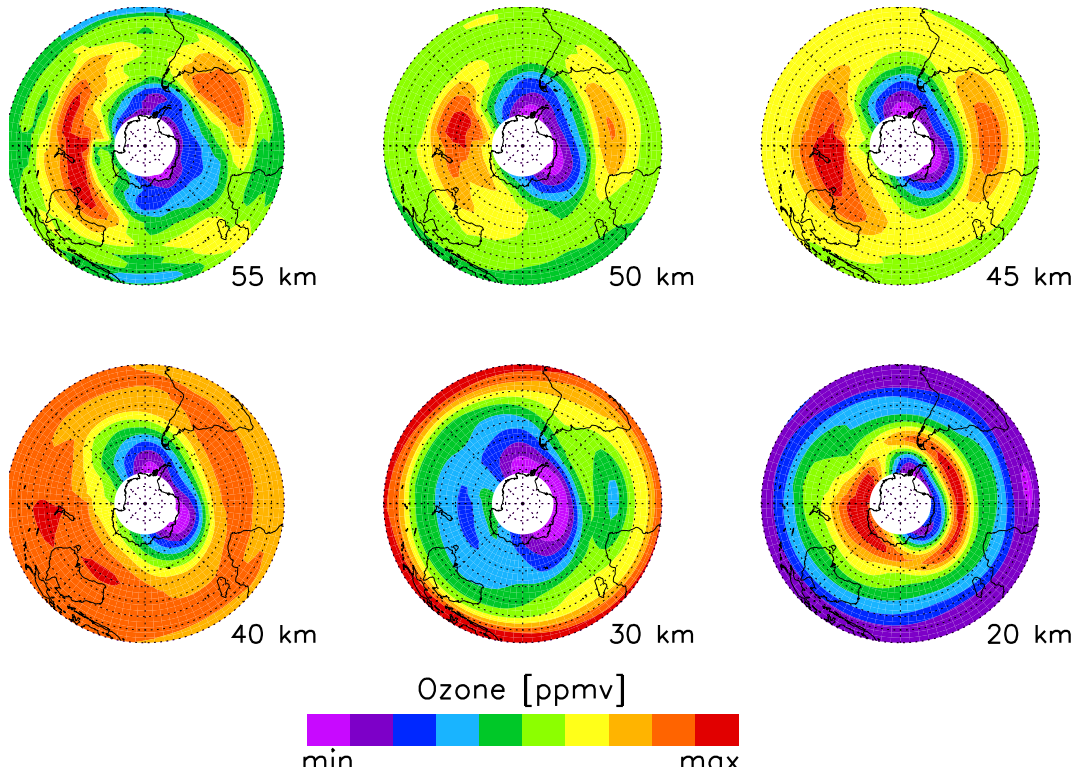


Figure 19: Same as Figure 18 but for ozone

for example, by *Fritts* (1984, 1989). Most observational studies of gravity waves are based on ground-based observations from a limited number of locations (e. g. *Eckermann et al.*, 1995). More recently, global data sets obtained from satellite measurements have been used for GW studies (*Fetzer and Gille*, 1994; *Wu and Waters*, 1996). CRISTA data allow analysis of gravity waves with vertical wavelengths larger than about 4 km (*Preusse et al.*, 1999). *Eckermann and Preusse* (1999) discuss temperature profiles measured in the lee of the Andes in terms of mountain waves. The southern tip of South America is found to be a region of very high GW activity during the CRISTA-1 measurement period. Future work will focus on global distributions of GW sources such as orographic, deep convection, and regions of strong wind shear (*Preusse*, personal communication).

3.2 Tracer transport by inertially unstable circulation

Inertial instabilities are dynamical features of the upper stratosphere and mesosphere, which result from an imbalance between the pressure gradient force and the centrifugal force (*Andrews et al.*, 1987). During CRISTA-1, the observed temperature field near the equatorial stratopause exhibited stacked perturbations with relatively short vertical scales (~ 10 km), consistent with low-latitude circulation cells responding to inertial instability. Indications of such circulation cells have been previously found in LIMS observations (*Hitchmann et al.*, 1987), CLAES observations (*Hayashi et al.*, 1998), and numerical model results (e. g. *Sassi et al.*, 1993). This kind of air motion may be important for trace gas transport in the stratopause region.

CRISTA-1 temperature measurements were analyzed with respect to low latitude circulation cells by dividing the observational period into five subperiods, all having lengths of 24 hours or more, in order to obtain complete longitudinal coverage for both ascending and descending nodes during each period (*Smith and Riese*, 1999). Figure 20 shows temperature data detrended from the zonal mean background atmosphere for three subperiods (2, 4, 5) at the equator and at 30° N. Strong temperature perturbations occur during periods 4 and 5 at 36.5 km, 41 km, and 45.5 km altitude around 90° W and 60° E. The tropical temperature perturbations are paired with perturbations of opposite sign at 30° N. They are a result of circulation cells associated with inertial instability. Positive temperature perturbations indicate downwelling, while negative temperature perturbations indicate upwelling. As indicated in Figure 21 for the circulation cell at 90° W, CH_4 values show perturbations consistent with the predicted response to the circulation cells through transport. Perturbations in ozone (not shown here) are consistent with expected photochemical changes (*Smith and Riese*, 1999).

Figure 22 shows a longitude vs latitude EPV plot derived from CRISTA geopotential heights on the 1800 K isentropic surface (48 km) for each of the five periods. The results support previous findings that circulation cells with short vertical scales occur when the upper stratospheric flow is inertially unstable. Unstable regions may be identified in Figure 22 by Ertel potential vorticity (EPV) values of opposite sign to the planetary vorticity (e. g. negative EPV in the northern hemisphere.)

A new result is the occurrence of two separate circulation cells in different longitude

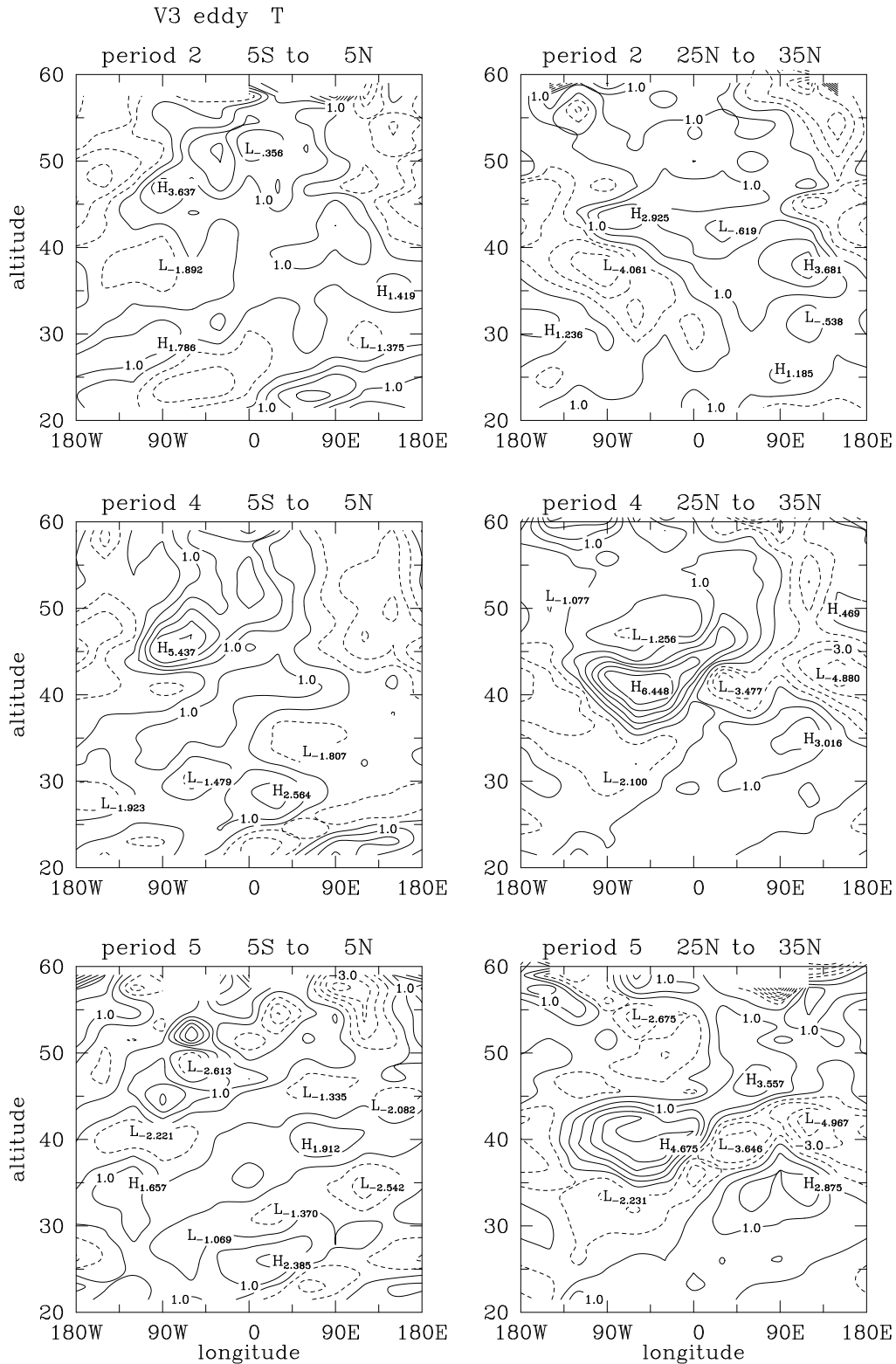


Figure 20: Longitude vs altitude cross section of CRISTA temperatures detrended from the longitudinal mean for the observation periods 2, 4, and 5. Positive values are shown by solid lines, while negative values are given by dashed lines. Contour interval is 1 K. Data shown in the left panel were averaged over the latitude band from 5° S to 5° N. Data shown in the right panel were averaged over the latitude band from 25° S to 35° N. (Figure 2 of *Smith and Riese, 1999*)

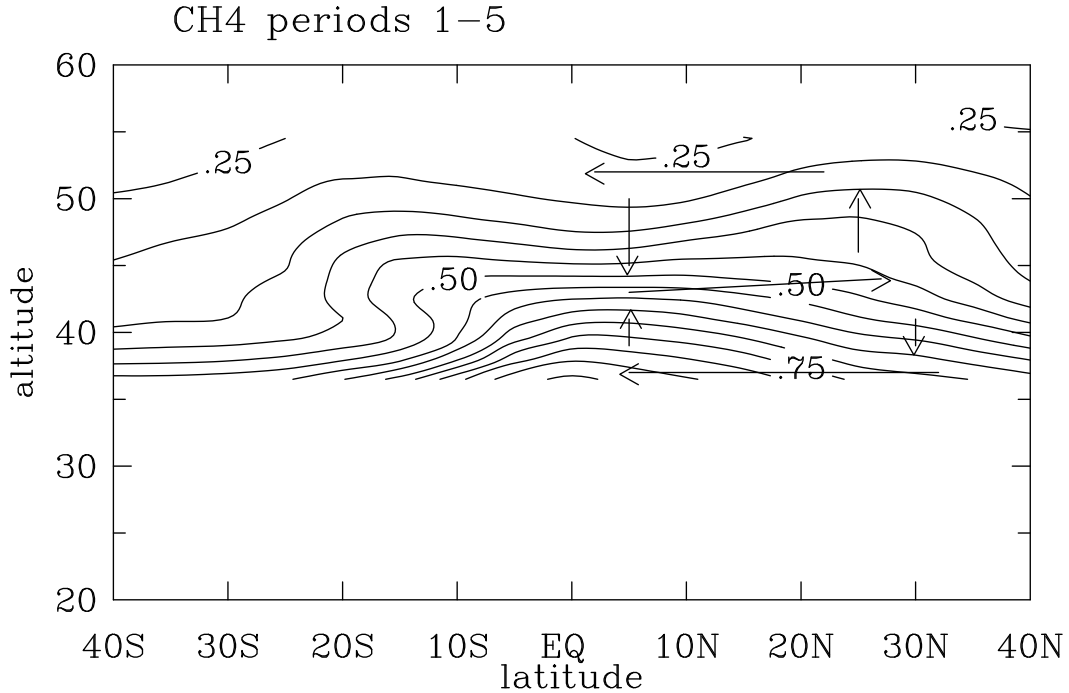


Figure 21: Zonal mean CH₄ mixing ratio averaged over the CRISTA-1 mission. The arrows show the circulation inferred from the temperature perturbations at 90° W shown Figure 23. Contour interval is 0.05 ppm. (Figure 6 of *Smith and Riese, 1999*)

bands that exhibit opposite phases (see Figure 20). At each altitude, perturbations at longitudes around 90° W have opposite signs to those located at 60° E.

Previous observations suggest that the outbreaks of circulation caused by inertial unstable conditions are quite rare. The chance of observing these structures during the CRISTA-1 mission was therefore not large. However, CRISTA temperature distributions clearly show an outbreak of inertial unstable circulation, although the temperature amplitudes derived from the CRISTA-1 observations ($\sim 3\text{K}$) are smaller than previously documented for such events (5 to 10K). This suggests that low perturbations as seen by CRISTA may have been below the detection limit of previous observations and that such cells may be more common than previous studies would indicate. In consequence, they could play a significant role for the transport of tracers in the stratopause region.

Another new finding is that the upper stratospheric circulation cell appears to be linked to a lower stratosphere Kelvin wave-one, which can be seen in the left panel of Figure 20 below 30 km. A detailed discussion of the wave characteristics is given by *Smith and Riese (1999)*. The amplitude of the Kelvin wave increased during

subperiod 1 and 2, persisted for about 3 days, and became weaker in the last period. Since the Kelvin wave has about the same vertical scale as the circulation cell, and is approximately in phase with it, interactions between these two dynamical features may have occurred. The vertical motion associated with the Kelvin wave may have affected the inertially unstable flow, e. g. by controlling its vertical scale.

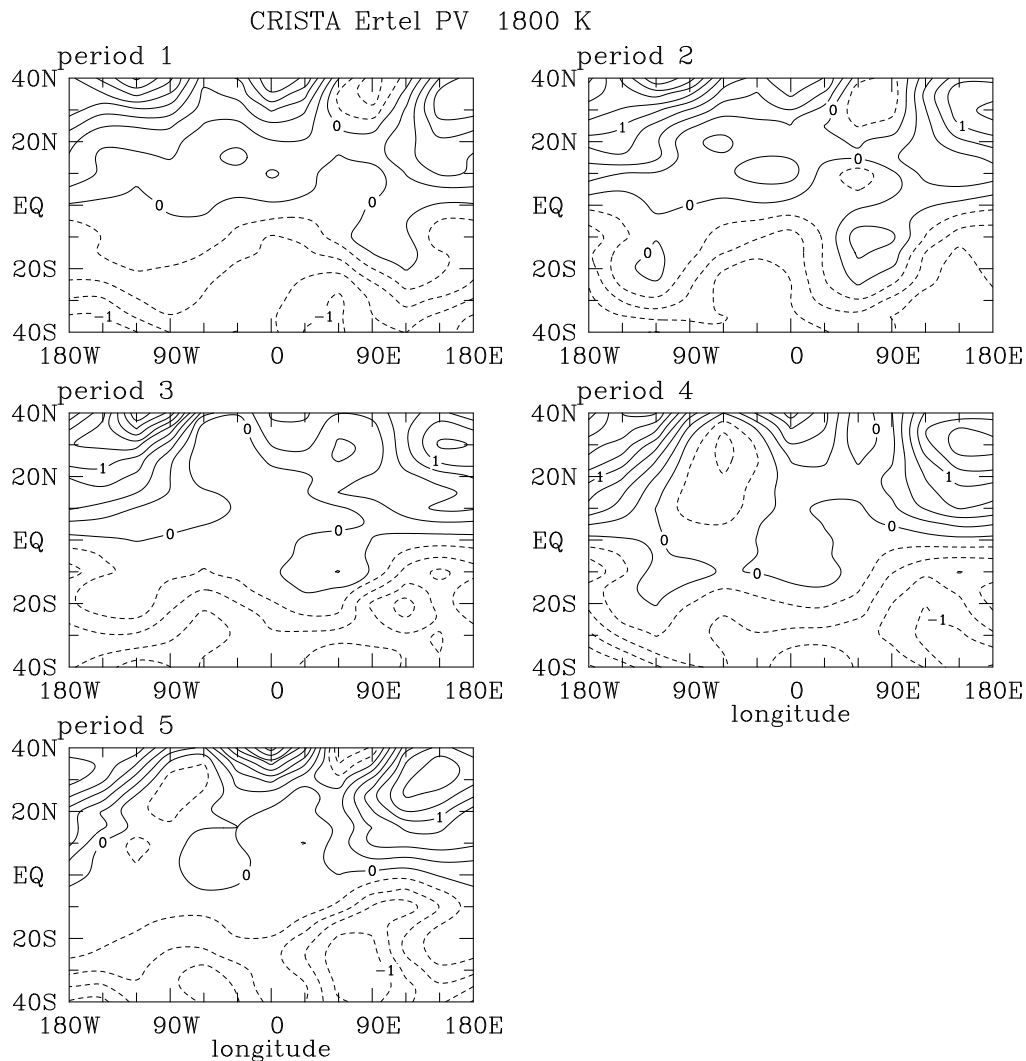


Figure 22: Ertels potential vorticity (EPV) derived from CRISTA data on the 1800 K (48 km) isentropic surface. Plotted is potential vorticity multiplied by the atmospheric density. Units are 10^5 K/(sm). The distributions are shown for the 5 observation periods. Areas with negative values are shown by dashed isolines. (Figure 5 of *Smith and Riese, 1999*)

3.3 Exchange of tropical and extra-tropical air

During winter, planetary waves facilitate quasi-horizontal transport and mixing in the stratospheric surf zone, which connects the vortex edge and the subtropical transport barrier (e. g. *McIntyre and Palmer, 1983*). Long-lived tracers such as nitrous oxide (N_2O), methane (CH_4), and chlorofluorocarbons (CFCs) are valuable tracers of such transport processes. Nitric acid (HNO_3) is a good tracer below 25 km, since the photochemical lifetime is on the order of several weeks in this region (*Brasseur and Solomon, 1986*). Satellite and aircraft observations of N_2O and CH_4 have been used in numerous previous studies of the stratospheric circulation and of stratospheric transport and mixing processes (e. g. *Mahlmann et al., 1986; Solomon et al., 1986; Holton and Choi, 1988; Garcia et al., 1992; Schoeberl et al., 1992; Randel et al., 1993, 1994; Stanford et al., 1993; Kindler et al., 1998*). The CRISTA data are especially suited for analyses of small- and medium-scale dynamical and photochemical structures associated with tropical/extra-tropical exchange of air by planetary wave mixing events (see also *Randel et al., 1993*).

CRISTA-1 observations

The meteorological conditions prevalent during CRISTA-1 have been described by *Manney et al. (1996)* and by *Naujokat and Pawson (1996)*. The north polar vortex had started to build up, while the south polar vortex had started to decay. The north polar vortex had developed above 35 mbar. The south polar vortex was strong below 16 mbar with coherent fragments up to 3 mbar. The situation was further characterized by enhanced temporal variability and strong small-scale and medium-scale dynamical structures. Analyses of high resolution potential vorticity (PV) fields generated by reverse trajectory calculations (*Manney et al., 1996*) also indicate that low latitude air was drawn around both vortices almost continuously. In addition, air was drawn off the vortices, leading to very complex air motions, especially in the northern hemisphere over the Pacific ocean and the western United States.

The general findings of the meteorological analyses are well reflected in the high resolution CRISTA-1 trace gas fields. The observations show enhanced temporal variability and pronounced dynamical structures. For example, several streamers of tropical and arctic air have been found in the CRISTA-1 measurements. Figure 23

shows an HNO_3 distribution measured on November 6, 1994 at 22.5 mbar (25 km). An air mass of HNO_3 rich air from the North polar vortex occurs in the region of the eastern United States. South of it a tongue of tropical air (streamer) extends from the southern United States across the Atlantic ocean towards Europe. Another strong tropical extrusion can be seen along the Asian coast. A third tropical extrusion of HNO_3 poor air extends across the South American continent into the South Atlantic Ocean.

A comparison of such dynamical structures with corresponding results of three-dimensional simulations performed with a chemical transport model is presented in Section 4.2 (see also *Riese, 1999; Riese et al., 1999b, 1999e, 2000a*).

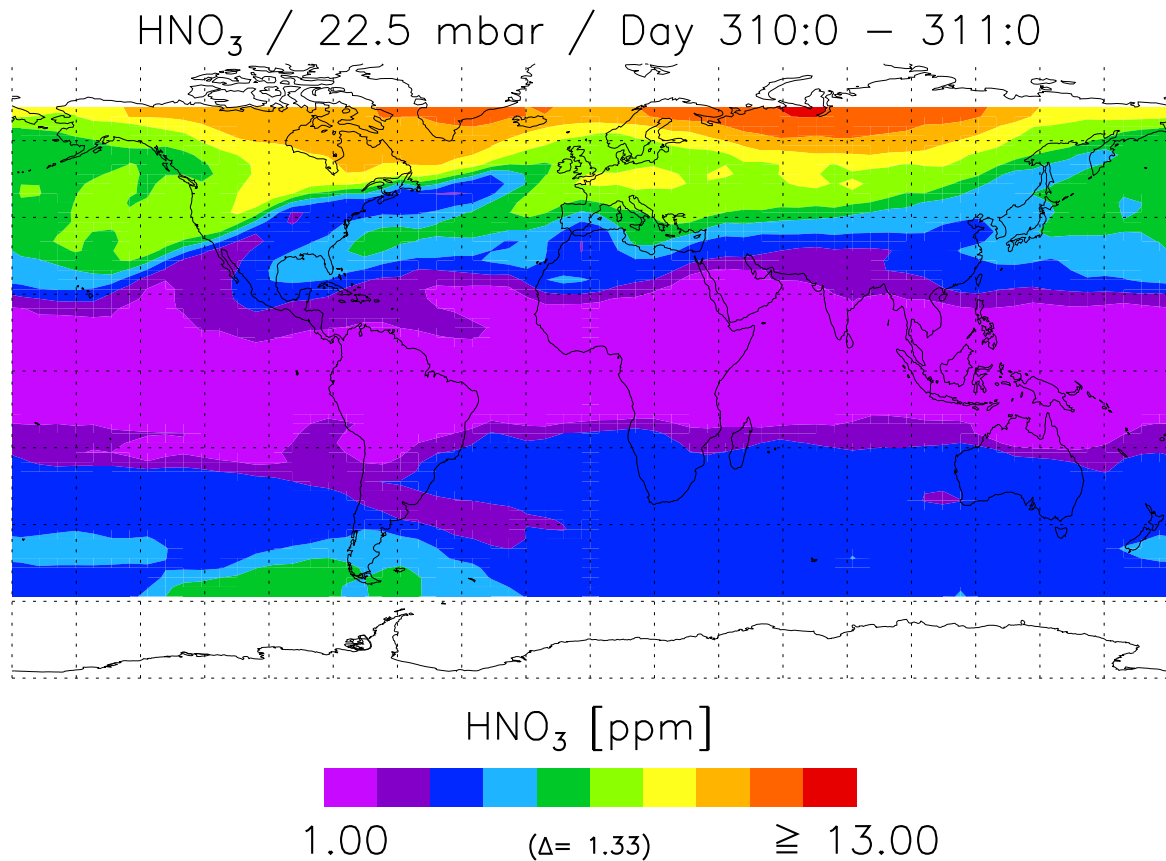


Figure 23: Mixing ratios of HNO_3 measured by CRISTA on November 6, 1994 at 22.5 mbar (25 km).

CRISTA-2 observations

During the second mission, CRISTA encountered conditions of large planetary wave activity in the southern hemisphere. Figure 24 shows a CH_4 distribution measured on August 11, 1997 at 4.6 mbar (35 km). The very low CH_4 mixing ratios at high southern latitudes indicate the elongated and deformed polar vortex, which results in pronounced wave-one and wave-two structures. The phase propagation of these waves is eastward during the course of the mission (not shown). The associated wind field advects air out of the tropics. As expected, the interaction between the polar vortex and the tropics is most pronounced in the area of the strongest vortex elongation (at the date line), where further analysis show wave breaking occurring (see also Figure 35).

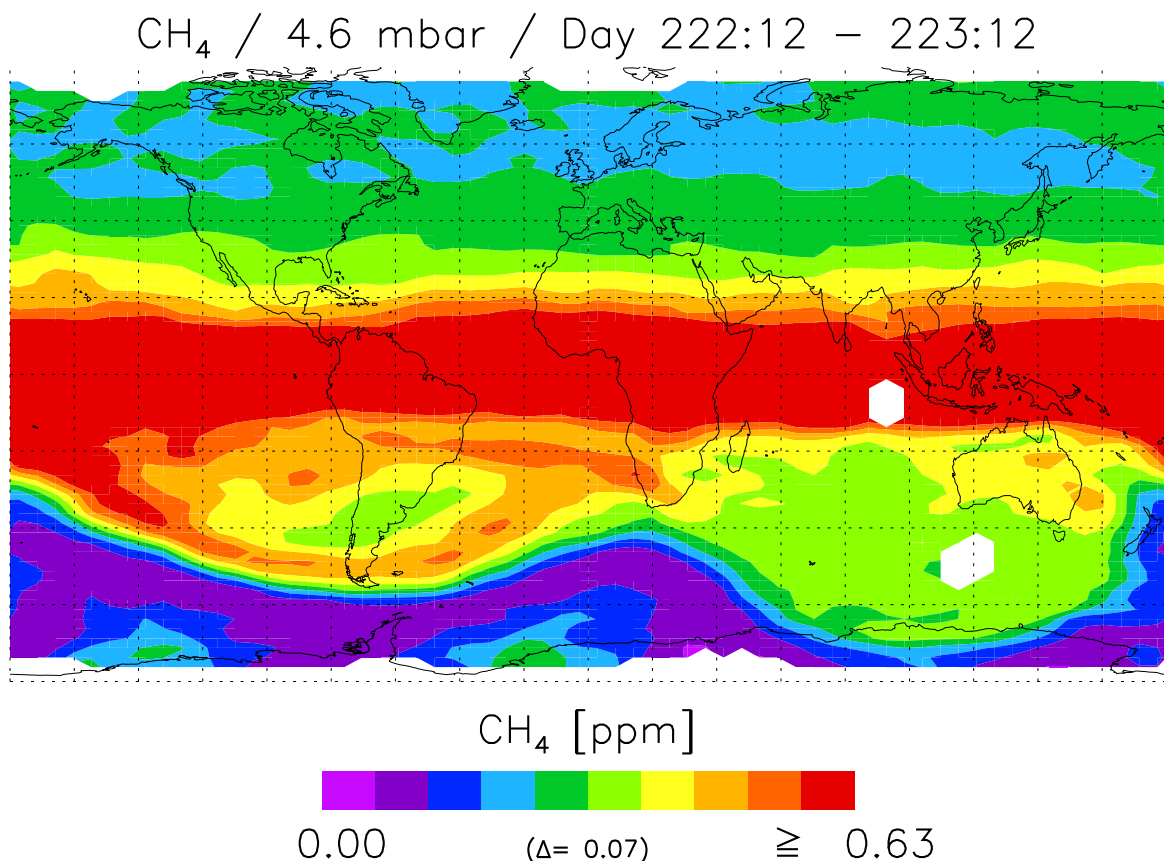


Figure 24: Mixing ratios of CH_4 measured by CRISTA on August 11, 1997 at 4.6 mbar (35 km).

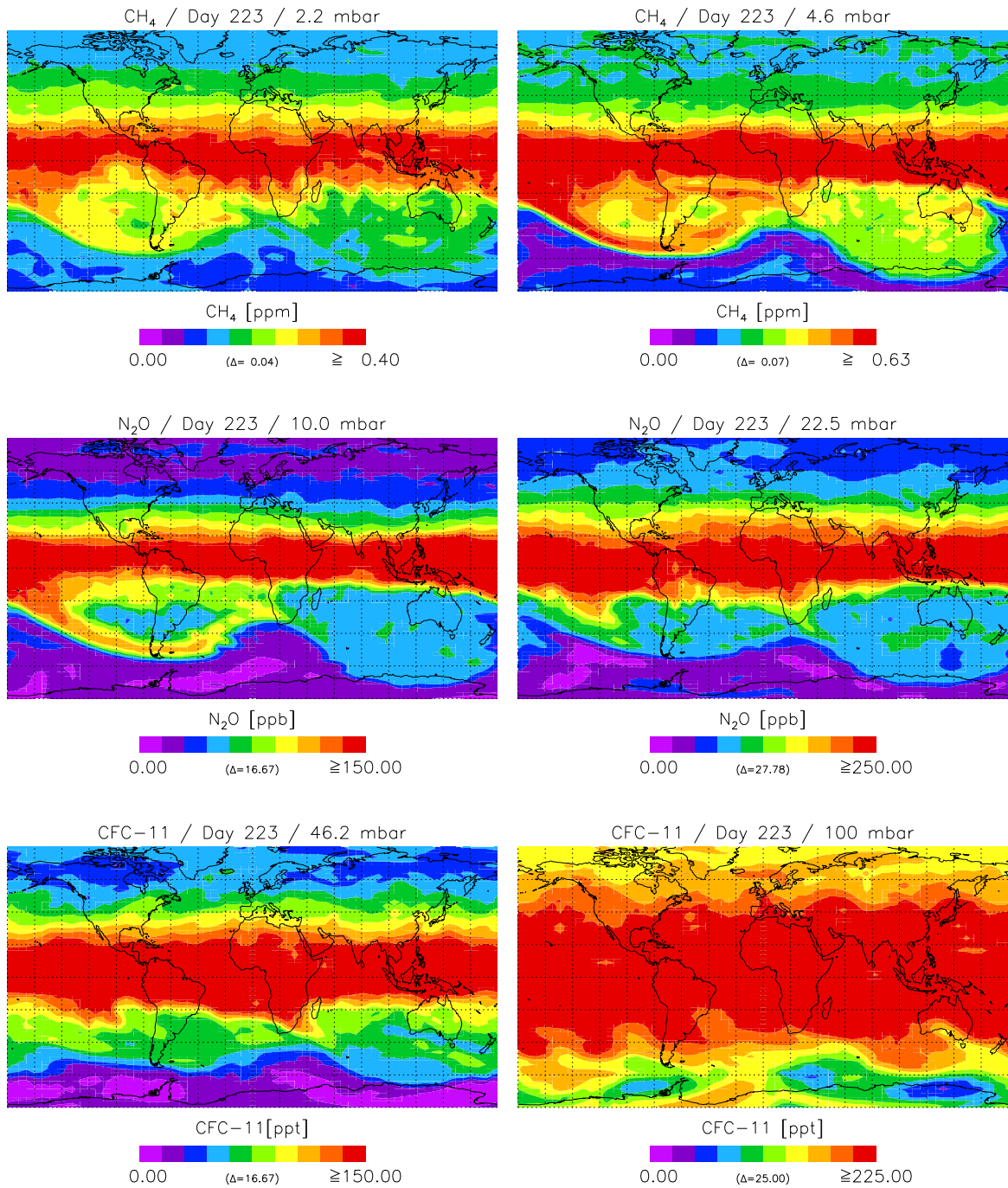


Figure 25: Analyzed (assimilated) CRISTA distributions of CH₄ (2.2 and 4.6 mbar), N₂O (10.0 and 22.5 mbar), and CFC-11 (46.2 and 100 mbar) on August 11, 1997.

The strength of the tropical extrusion, which results from the interaction of the polar vortex with the tropics, shows a pronounced altitude dependence. This is illustrated in Figure 25 by means of synoptic distributions of CH₄ (2.2 and 4.6 mbar), N₂O (10.0 and 22.5 mbar), and CFC-11 (46.2 and 100 mbar). A close relationship between the strength of the tropical extrusion and the amplitude of the planetary wave-two (Figure 17) is found.

Narrow tongues of tropical air were found during both CRISTA missions (see Figures 23 and 24). This suggests that displacement of the polar vortices frequently result in such dynamical structures. The CRISTA observations also demonstrate that these narrow tongues of tropical air can be highly variable in time and space. Results indicating the large temporal variability of tropical extrusions are presented in Section 4.2 based on CFC-11 observations at 31.6 mbar (23 km).

4 Three-dimensional modeling of the stratosphere

Modeling the behavior of minor constituents in the middle atmosphere has a long history. Models can be considered as the mathematical representation of our theoretical knowledge about chemical and dynamical processes. In one-dimensional models vertical transport is parameterized by means of vertical eddy diffusion concepts. Such models are well suited to detailed studies of chemically reactive species and diurnal variations (e. g. *Brasseur et al.*, 1987). Two dimensional models (e. g. *Brasseur et al.*, 1990; *Garcia and Solomon*, 1983) are frequently used to predict long-term changes of chemical constituents relevant for climate change. For a detailed understanding of the basic processes affecting transport of chemical species (and interactions with chemical processes) three-dimensional model formulations (e. g. *Rose and Brasseur*, 1989) have to be used and verified by observations.

4.1 Model description

Three-dimensional simulations can be performed by using two different approaches. Dynamical, chemical models calculate “on line” the dynamical variables of the atmosphere (e. g. wind and temperature fields). Chemical transport models (CTM), on the other hand, consist of chemistry and transport packages driven “off line” by three-dimensional dynamical models or conventional meteorological analyses. For example, analyzed winds provided by the UK Meteorological Office (UKMO) [*Swinbank and O’Neill*, 1994] or by the NASA GSFC data assimilation system (GEOS1DAS) [*Suarez et al.*, 1995] have been widely used for transport studies of atmospheric trace constituents (e. g. *Rood et al.*, 1989, 1992; *Rosenlof and Holton*, 1993; *Chen et al.*, 1994; *Douglass et al.*, 1996; *Kindler et al.*, 1998; *Chipperfield*, 1999).

The simulations presented in this section were performed with a three-dimensional model, combining the chemistry and transport codes of the NCAR ROSE model (e. g. *Rose*, 1983; *Rose and Brasseur*, 1989; *Granier and Brasseur*, 1991; *Smith*, 1995) with UKMO wind and temperature fields (see also *Lefèvre et al.*, 1994). The wind and temperature values are a product of a data assimilation system developed at the UK Meteorological Office for the UARS project (see *Swinbank and O’Neill*, 1994). The system assimilates a heterogeneous set of satellite temperature measurements and

radiosonde observations into a global circulation model (GCM) in order to obtain self-consistent synoptic wind and temperature distributions at a specific time. Assimilated winds and temperatures are available for 22 pressure levels from the ground up to 0.316 mbar (55 km) with a vertical step of 2.7 km. This vertical step is on the order of the vertical resolution of CRISTA trace gas data (2.5 to 3 km). The ROSE CTM uses 19 pressure levels between 316 mbar (8 km) and 0.316 mbar (55 km). The horizontal resolution of the meteorological data provided by the UKMO is 3.75° in longitude and 2.5° in latitude. This corresponds to 96×72 grid points for a given pressure level. Model runs with the CTM can be performed at this particular horizontal resolution or at somewhat lower horizontal resolutions (64×72 , 32×36). The present study uses 64×72 grid points (5.65° in longitude and 2.5° in latitude).

The ROSE model accounts for the chemistry of oxygen, hydrogen, carbon, nitrogen, chlorine, and bromine species. About one hundred gas phase reactions and seven heterogeneous reactions on volcanic aerosols and polar stratospheric clouds are included in the model. The reaction rate constants and absorption-cross sections are taken from the JPL-compilation (e. g. *DeMore et al.*, 1997). Solar irradiances are obtained from the Solar Stellar Irradiance Comparison Experiment (SOLSTICE) on board UARS. Photolysis rates are derived from pre-calculated lookup tables as a function of altitude, albedo, ozone column, and solar zenith angle. The chemical compounds are divided into two groups. Twenty-seven long-lived species (or families) are affected by both transport and chemistry. Fourteen short-lived or equilibrium species are calculated at each time step (20 min) neglecting transport. The transport of long-lived species and families is calculated with a semi-Lagrangian transport algorithm (*Smolarkiewicz and Rasch*, 1991).

Initial fields of long-lived species such as CFC-11, N_2O , and CH_4 have been derived from potential vorticity (PV) distributions of the starting day (November 1) by assuming a close correlation between the long-lived species and PV. Through this approach, initial structures are introduced into the trace gas fields that exactly resemble the structures of the PV fields. No information about structures in the constituent fields observed by CRISTA enters the initialization. For CRISTA-1 the correlation parameters were obtained from linear fits. More details about the initialization procedure are given by *Riese et al.* (1999b).

4.2 Simulation of the CRISTA measurement periods

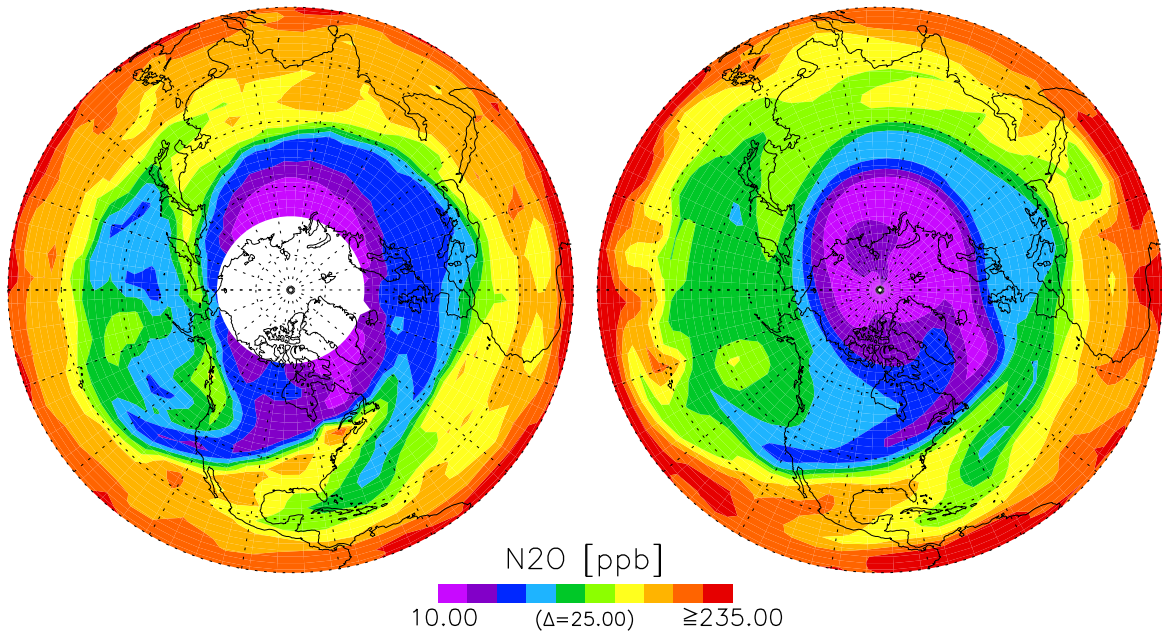
Exchange of tropical and extra-tropical air during CRISTA-1

A comparison of a measured northern hemispheric N_2O distribution (14.7 mbar) with results obtained from the model is shown in Figure 26 for November 6 (Day 310). The measurements were interpolated onto the model grid (64 x 72) by applying a two-dimensional weighting function, which resembles a triangle function with a half width of 8° in longitude and 4° in latitude. For comparison reasons, the filter was also applied to the modeled distribution. The filter suppresses the random noise of the observations as well as non-coherent fluctuations between adjacent measurement points caused by small-scale (unresolved) atmospheric processes. The measurements shown in Figure 26 were taken between Day 309:12 and Day 310:12, while the modeled distribution represents a synoptic map of Day 310:0. The general shape of the polar vortex is well reproduced by the model. The associated wind field advects air out of the tropics towards higher latitudes. Two pronounced tropical extrusions can be seen in the CRISTA observations: one extrusion extends across the southern United States into the Atlantic Ocean, and the other extends along the North American and Asian Pacific coast. Air is also drawn off the vortex (e. g. north of the Atlantic extrusion). In addition, a very pronounced extrusion of Arctic air is drawn from Canada into the Pacific Ocean. The interaction of this Arctic extrusion with the Asian tropical extrusion results in very complex air motions, especially over the Pacific Ocean.

The model captures the Atlantic extrusion of tropical air and the Arctic extrusion north of it. However, the strength of the Asian extrusion of tropical air and the associated transport along the coasts of Asia and North America are somewhat underestimated. For more quantitative comparisons of measured and modeled structures, the N_2O values have been “detrended” by subtracting zonal mean values at each latitude. Through this approach, the synoptic structures of the N_2O fields are more emphasized, e. g. the modeled Asian extrusion of tropical air (see lower panel of Figure 26). It can be seen that the combination of assimilated wind fields and the transport code used by ROSE is well suited to predict such planetary-scale tongues which significantly contribute to the mass exchange between the tropics and higher latitudes. However, the structures are more pronounced in the measured N_2O distribution at middle and high latitudes. This implies a larger horizontal eddy flux of

a.) CRISTA / 14.7 mbar / Day 309:12–310:12

b.) Model / 14.7 mbar / Day 310:0



c.) CRISTA / 14.7 mbar / Day 309:12–310:12

d.) Model / 14.7 mbar / Day 310:0

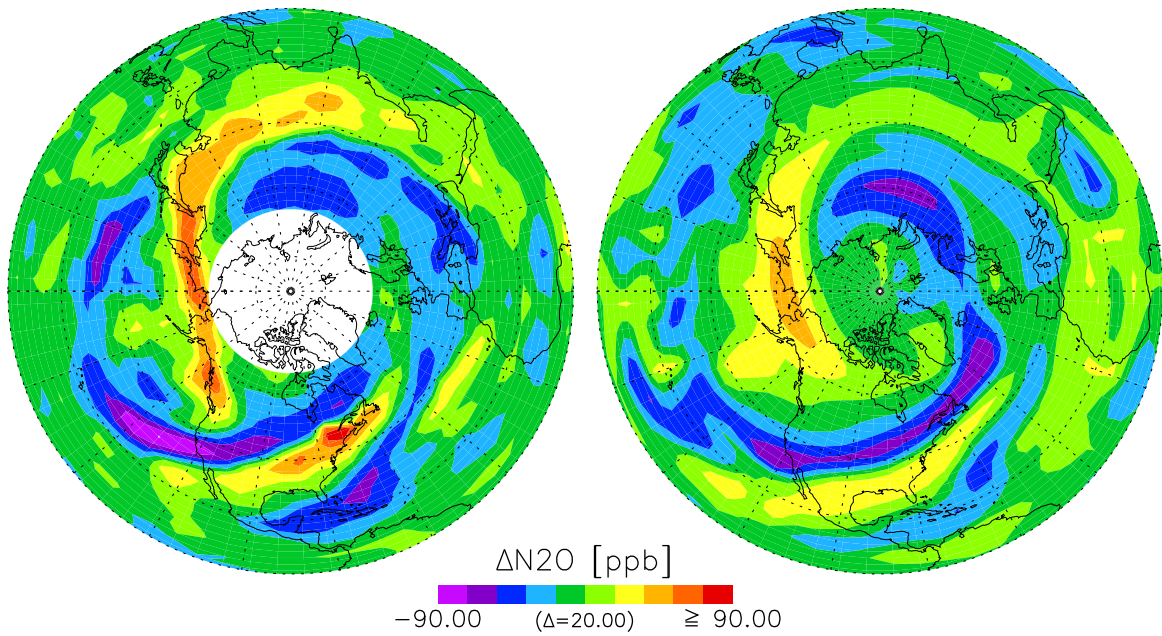


Figure 26: Comparison of a measured and modeled northern hemispheric N₂O distribution for November 6, 1994, at 14.7 mbar. Absolute values (upper panel) are shown as well as detrended values obtained by subtracting zonal averages at each latitude (lower panel).

N_2O than indicated by the the model results.

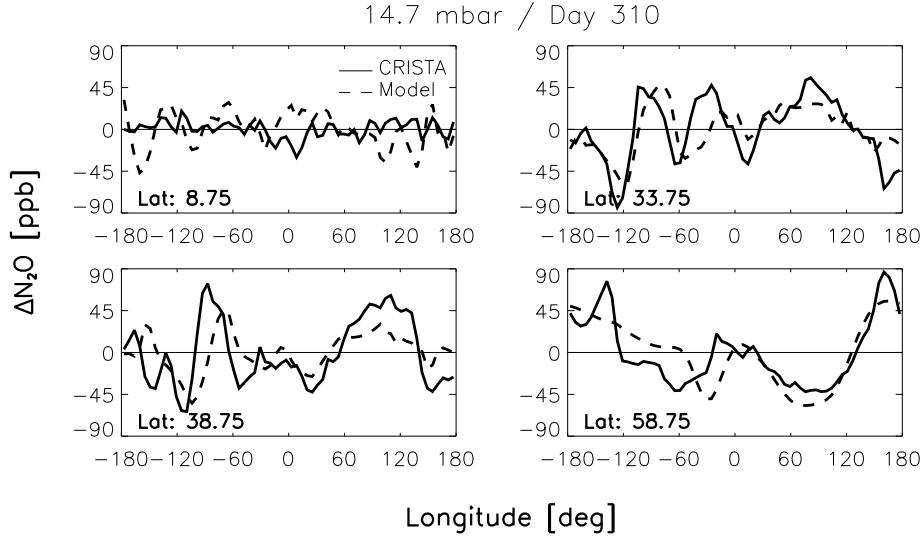


Figure 27: Comparison of measured and modeled longitudinal plots of detrended N_2O values at 14.7 mbar. Data are shown at four latitudes of the model grid (8.75° , 33.75° , 38.75° , and 58.75°). The detrended values were obtained by subtracting zonal mean values at each latitude.

The situation is quite different in the tropical and subtropical regions. The model results exhibit large medium-scale variability, which does not exist in the measured distribution. This discrepancy is shown in Figure 27 by means of longitudinal plots of detrended N_2O mixing ratios. At 8.75° N, unrealistically high variability is found in the model result. Since the structures of the modeled N_2O distribution are of medium scales, they would have been detected by CRISTA, if they were real. Such an overestimated variability in the tropics and subtropics appears to be a common problem of trace gas simulations based on assimilated winds. *Kindler et al.*, (1998) find, for example, unrealistically large amplitudes of wavenumbers 4 to 7 in the tropics and subtropics when comparing N_2O simulations to CLAES observations.

Temporal evolution of CFC-11 at 31.6 mbar (23 km)

Figure 26 demonstrates that the CTM reproduces important horizontal structures at mid-latitudes in the northern hemisphere at a pressure level of 14.7 mbar. The tropical extrusion that extends across the southern United States into the Atlantic Ocean is also very pronounced in CFC-11 observations at lower altitudes (N_2O data are only available down to about 22.5 mbar), as discussed below.

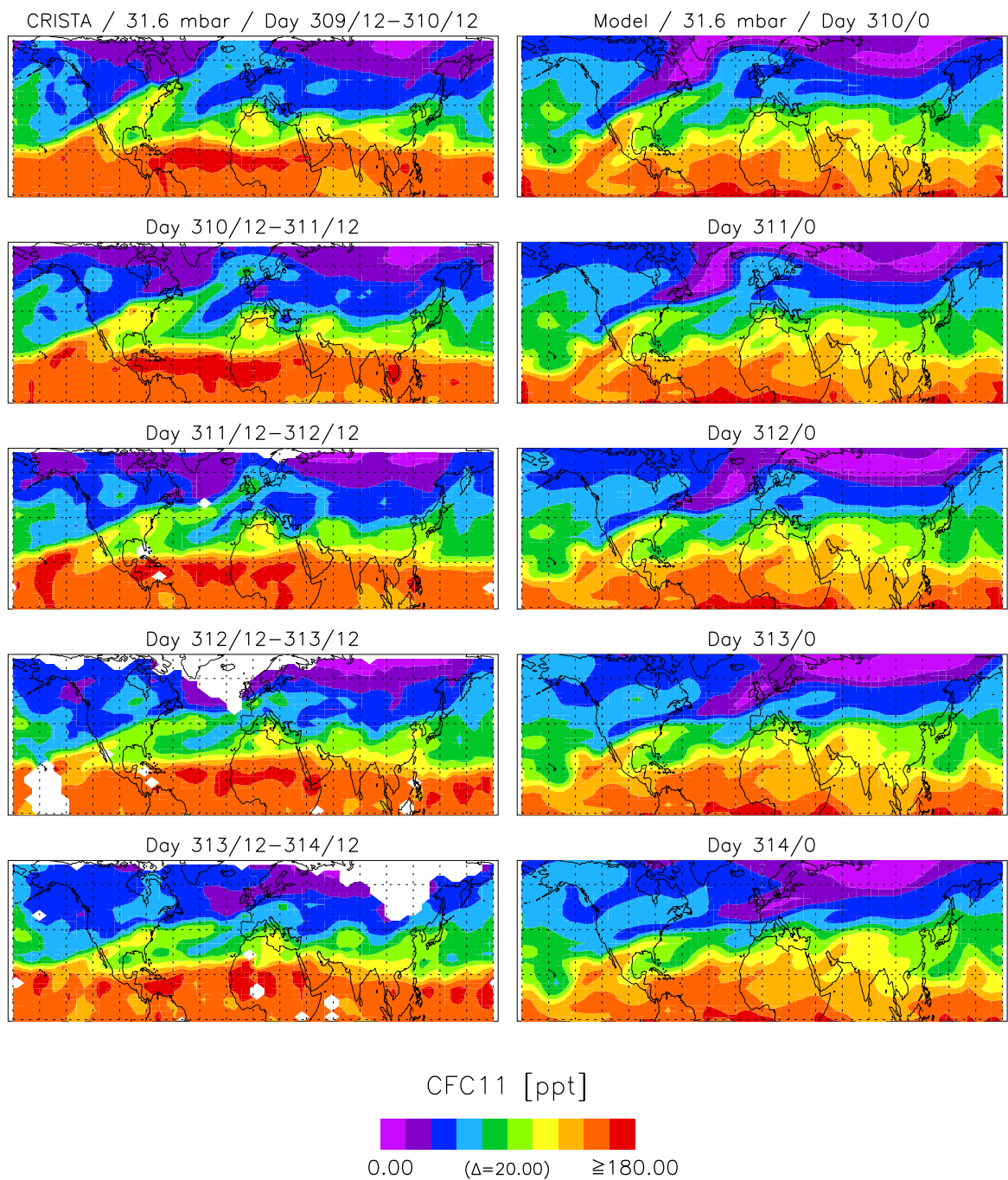


Figure 28: Measured and modeled time sequence (November 6 to November 10, 1994) of the northern hemispheric CFC-11 distribution at 31.6 mbar. Since CRISTA covers latitudes up to $+67^\circ$, the data are compared in the latitudinal band from 0° to $+70^\circ$. The blank areas in the measured maps indicate grid points where no measured data are available inside the non-zero region of the weighting function used for filtering the data.

During the measurement period of CRISTA-1, the shape of the north polar vortex varied significantly from day to day. A very pronounced planetary wave-two structure (stretched vortex) decayed in favor of a planetary wave-one structure (vortex shifted towards Scandinavia). Figure 28 shows a comparison of a measured and a modeled time sequence of CFC-11 distributions of the northern hemisphere (31.6 mbar) for the time period from November 6 to November 10 (Day 310 to Day 314). Associated detrended CFC-11 mixing ratios (Day 310 and Day 312) are compared in Figure 29 at four different latitudes.

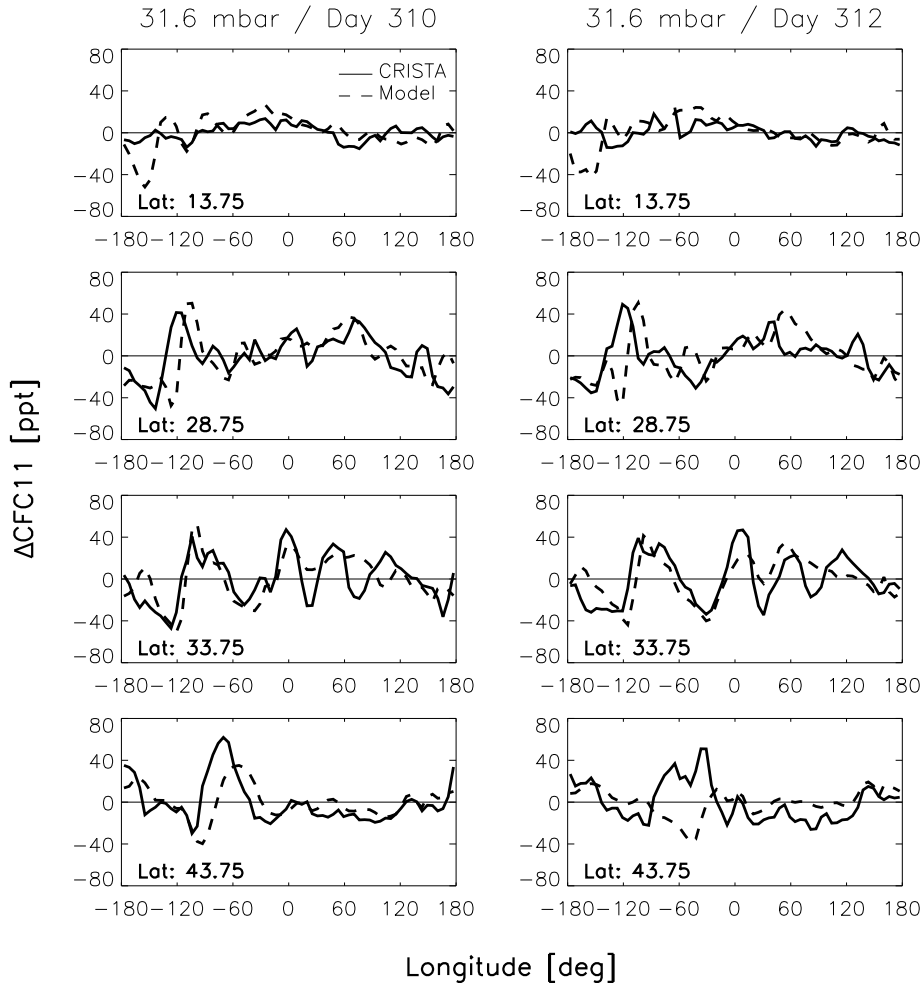


Figure 29: Comparison of measured and modeled longitudinal plots of detrended CFC-11 values at 31.6 mbar for November 6 and 8, 1994. Data are shown at four latitudes of the model grid (13.75° , 28.75° , 33.75° , and 43.75°). The detrended values were obtained by subtracting zonal mean values at each latitude.

The calculated fields represent synoptic maps (e. g. Day 310:0) while the measured fields contain data that were measured within a 24 hour time period (e. g. from Day

309:12 to Day 310:12). The modeled distributions capture a lot of the dynamical features, especially at middle and high latitudes. On November 6, the deformation of the north polar vortex and the resulting pronounced wave-two structure at high latitudes are indicated by CFC-11 poor vortex air. The north polar vortex is stretched towards Siberia and North America. The associated wind field advects air out of the tropics into higher latitudes.

At the 31.6 mbar pressure level, the strong tropical extrusion that extends across the United States into the Atlantic Ocean (see also Figure 26) is more pronounced than the extrusion at the Pacific coast. The model reproduces this tropical extrusion well. During the following days, the north polar vortex is shifted towards Europe, leading to a pronounced wave-one structure. As a result, the extrusion of tropical air is also displaced toward the South and stretched towards Europe and Asia. The CFC-11 observations of Day 314 suggest that some irreversible mixing of tropical air occurs over Europe and Asia.

The amplification of the wave-one structure and the associated deformation of the tropical extrusion are very similar in both observation and simulation. However, minor differences of the transport processes show up in the comparisons of Figure 29. On Day 312, the modeled tropical extrusion is somewhat more shifted towards the South than the observed extrusion. As a result, a large discrepancy occurs in Figure 29 at 43.75° N. Notable differences between the observations and the model results also occur in the tropics and subtropics, where the model produces too much variability. This finding confirms the result of the N_2O study at 14.7 mbar.

Structures observed in the southern hemispheric surf zone

A comparison of a measured and a modeled N_2O distribution in the southern hemisphere (10 mbar) is shown in Figure 30 for November 6. The reproduction of the observation by the model is considerably worse than in the northern hemisphere. The south polar vortex was already decaying at this pressure level. In addition, large amounts of tropical air were transported to higher latitudes (before the CRISTA mission) as a result of a strong interaction of the disturbed polar vortex with the tropics in mid October.

Figure 30 indicates that the UKMO winds (in conjunction with the transport

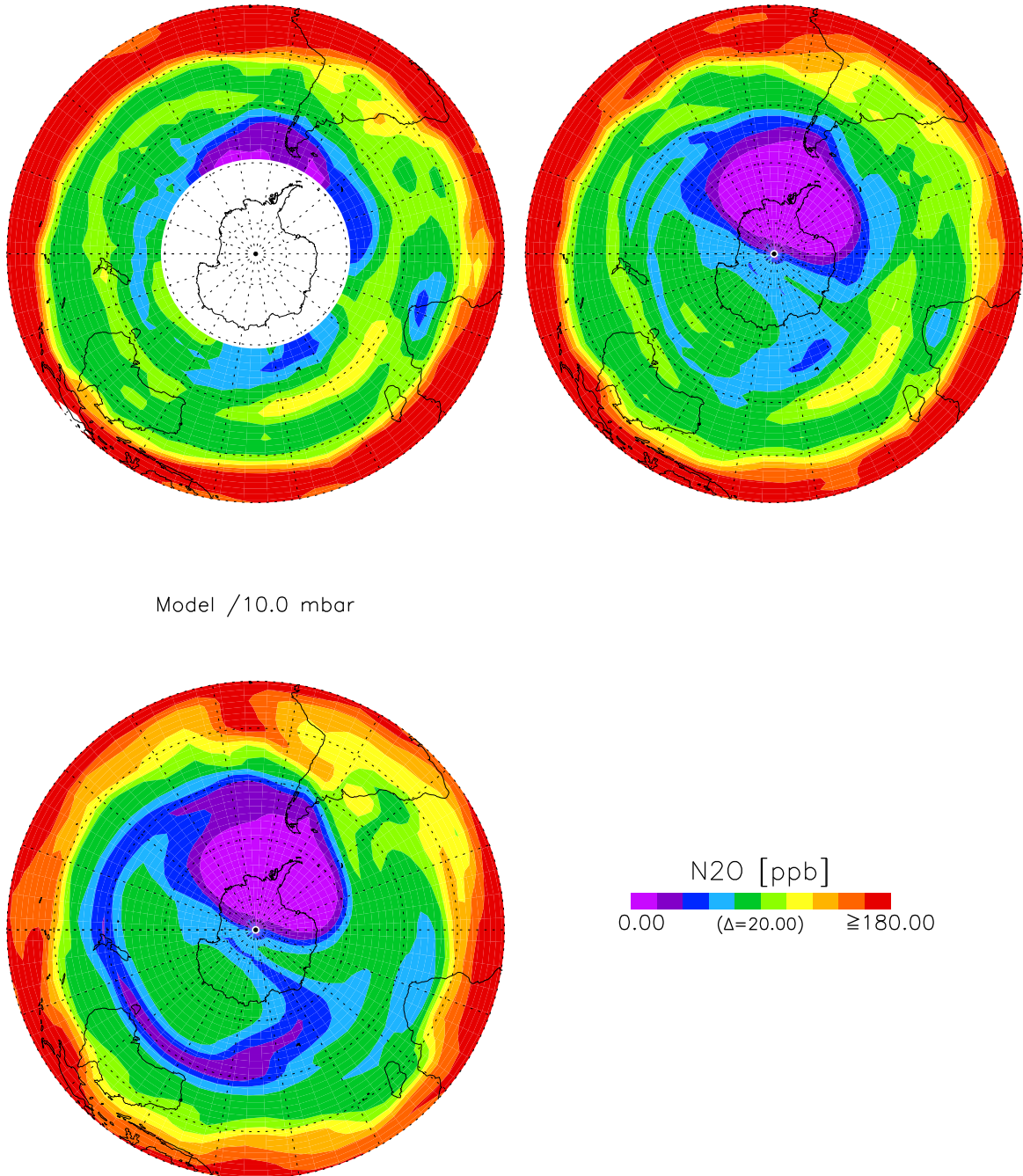


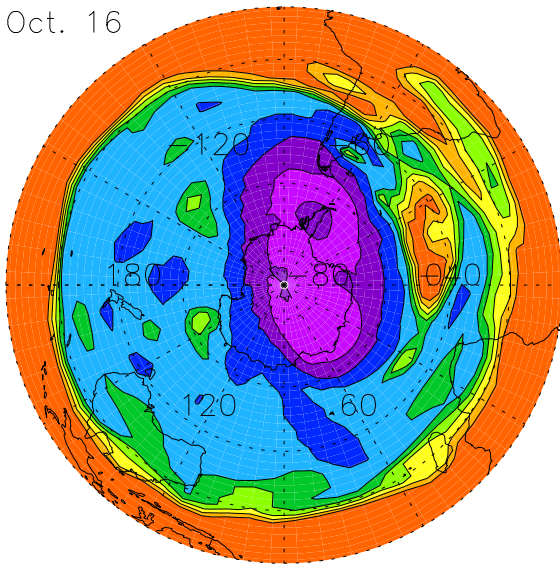
Figure 30: Comparison of a measured (upper panel) and a modeled (lower panel) southern hemispheric distribution of N₂O for November 6, 1994 at 10 mbar. Shown are polar projections of the southern hemisphere. Latitudinal circles (dotted circles) are given with an increment of 20° (starting from the equator). The upper panel shows the synoptic observations (left side) as well as a synoptic distribution (right side) obtained from the sequential trace gas assimilation system described in Sections 2.5 and 5.1.

scheme) are not quite able to reproduce the complex pattern of the associated air motions. There are major differences between the measured and modeled distribution. Possible reasons for these differences are as follows: In the model, there is a strong interaction of the elongated vortex with tropical air west of South America (on November 6), while the vortex is more separated from the subtropics in the measured distribution. This is mainly due to the steeper horizontal gradient of the measured N₂O mixing ratio in the vicinity of the subtropical transport barrier at about 15° S. The most notable difference between the model and the measurements occurs in the region of the stratospheric surf zone (e. g. *McIntyre and Palmer, 1993*), which connects the observed transport barrier and mid-latitudes. In the simulation a pronounced tongue of vortex air is drawn out towards low latitudes. Over the Pacific ocean, the tongue extends along the -40° latitudinal circle. In reality, the wind field advects two weaker tongues along this latitudinal circle. One of these tongues originates from the edge of the polar vortex, while the other tongue contains air of relatively high N₂O mixing ratios. This tongue is most likely the remnant of a large tropical air mass, which entered the surf zone as result of an interaction of the Antarctic vortex with the tropics (*Franzen et al., 2000*). This interaction took place about three weeks before the CRISTA-1 mission.

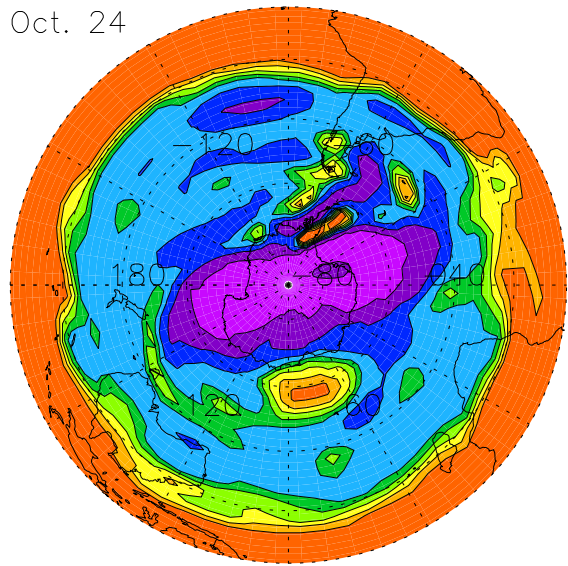
The complicated dynamical situation before the CRISTA-1 mission is illustrated in Figure 31 by means of N₂O values derived from UKMO PV fields by assuming a close correlation between PV and N₂O. The time sequence shown in Figure 31 illustrates the transport of tropical air towards higher southern latitudes. On October 16 the Antarctic vortex is deformed and shifted towards the tip of South America. A large extrusion of tropical N₂O rich air is being separated from the tropics (15° W, 50°S) due to a strong interaction with the polar vortex during the preceding days (not shown here). After the separation the air mass is advected by westerlies and starts to circle around the South Polar Vortex. On November 1 it is located between longitudes of 90 °E and 180°E and it becomes somewhat stretched. During the following days the remnant of the tropical extrusion is influenced by easterlies and is transported back to a longitude of about 45°E. The center of this air mass is also to be seen in the CRISTA observation (Figure 30).

A study of the temporal development of the tropical extrusion in a full CTM simulation is rather difficult due to the strong interference from air masses of low N₂O

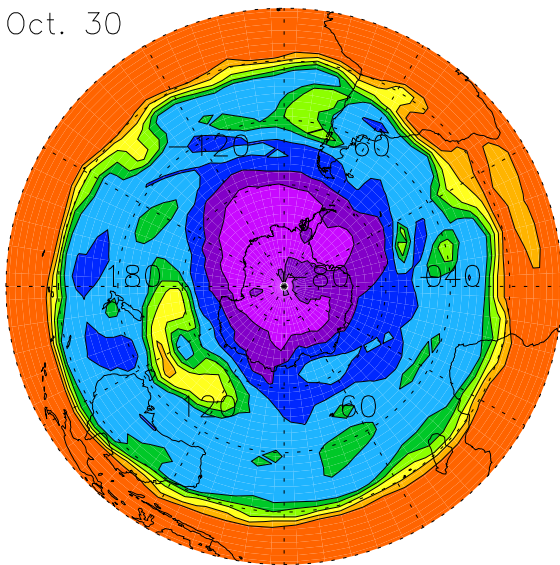
Oct. 16



Oct. 24



Oct. 30



Nov. 05

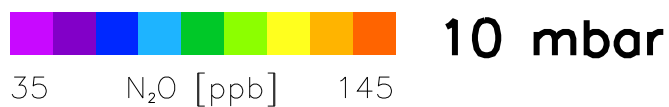
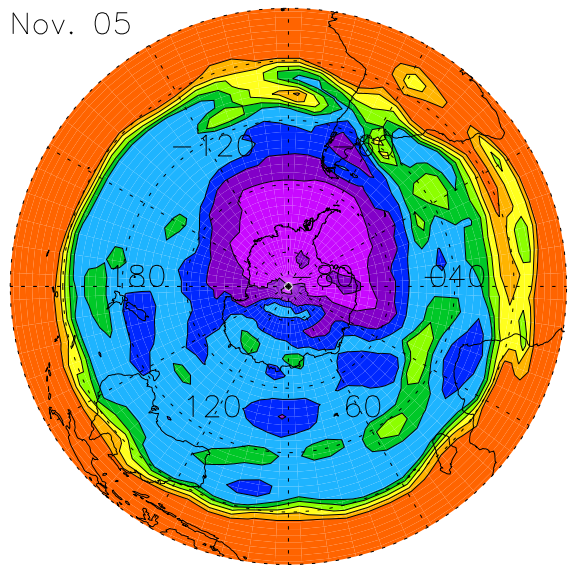


Figure 31: Temporal evolution of the southern hemispheric N₂O distribution at the 10 mbar pressure level. The N₂O values are derived from UKMO potential vorticity fields, CH₄ values of the UARS trace gas reference atmosphere, and N₂O/CH₄ correlation parameters obtained from the Atmospheric Laboratory for Application and Science (ATLAS) 1, 2, and 3 missions of the Atmospheric Trace Molecule Spectroscopy (ATMOS) instrument (*Dessler*, private communication).

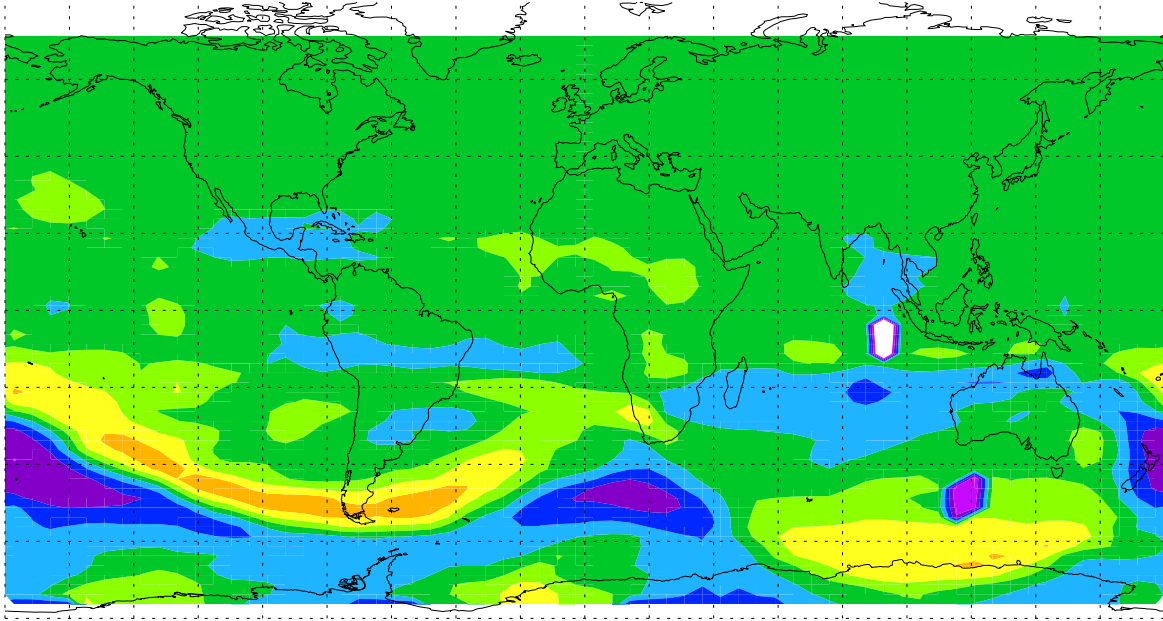
values resulting from the unrealistically strong breakup of the south polar vortex in the simulation at the beginning of the CRISTA-1 mission (see Figure 30). The breakup of the vortex in the simulation results in a pronounced tongue of vortex air, which interferes with the remnant of the tropical extrusion. For this reason, an idealized tracer study has been performed (*Franzen et al.*, 2000), which focused on the temporal development of the tropical air mass alone and neglects influences of the surrounding atmosphere. The results of this study indicate that the evolution of the tropical extrusion in early November depends critically on its location at the turning point of the eastward-westward motion. When shifting the tropical air mass somewhat to the south (5°) on October 30, part of it is transported along the 40°S latitudinal circle towards the tip of South America as suggested by the CRISTA-1 observation. This finding gives a hint of possible uncertainties of the meridional UKMO wind field, which may be too large at the turning point of the motion. Interestingly, corresponding NMC winds are about 5 m/s smaller (at 60°S), which is consistent with the southward shift applied in the sensitivity study. Idealized tracer studies of the behaviour of the Antarctic vortex indicate that such an overestimation of the northward wind component may also be responsible for the unrealistically strong breakup of the vortex obtained in full CTM simulations (see Figure 30).

Simulation of the CRISTA-2 measurement period

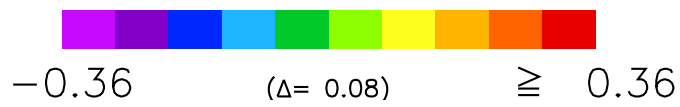
Simulations of the CRISTA-2 observational period are in progress. The initialization procedure of the model has been somewhat refined with respect to the CRISTA-1 simulations discussed above. Average mixing ratio values have been calculated from CRISTA-2 observations as function of pressure and equivalent latitude (see *Randel et al.*, 1998) derived from the meteorological PV fields. The calculated values can be used to convert the equivalent latitude distributions of specific days to corresponding trace gas fields (see also *Riese*, 2000). This initialization procedure was applied to the model on August 1, 1997.

A comparison of a measured CH_4 distribution (4.6 mbar) with results obtained from the model is shown in Figure 32 for August 11, 1997. The measurements were taken between Day 222:12 and Day 223:12, while the modeled distribution represents a synoptic map of Day 223:0. To emphasize the synoptic structures, the CH_4 fields have been “detrended” by subtracting the zonal mean background field. Good corre-

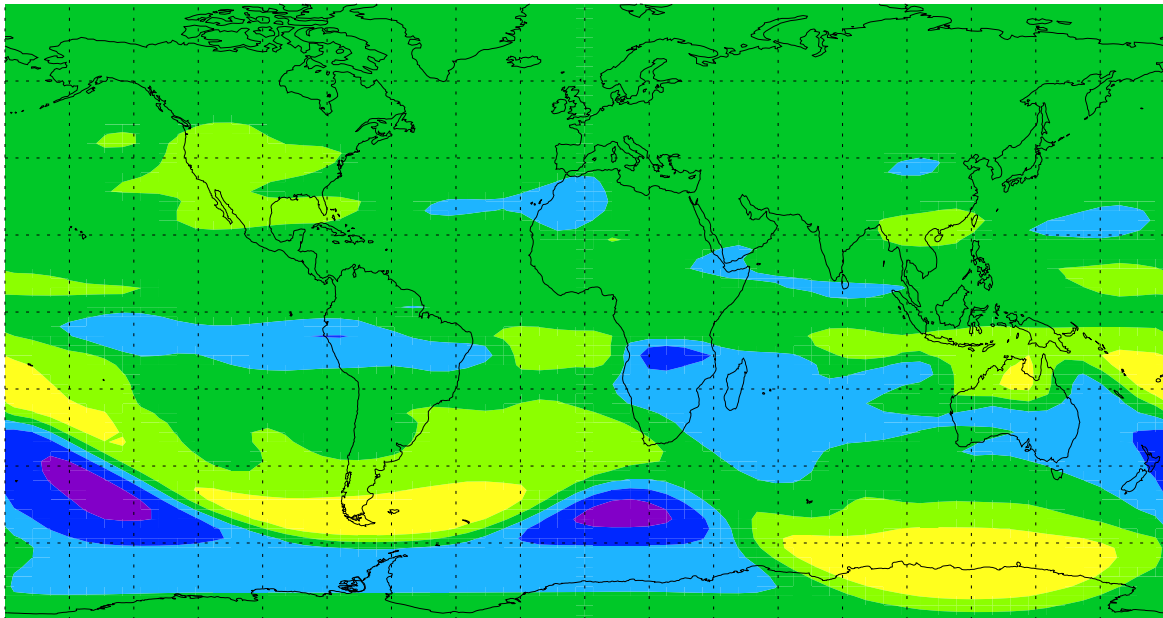
Eddy CH_4 / 4.6 mbar / Day 222:12 – 223:12



ΔCH_4 [ppm]



Eddy CH_4 / 4.6 mbar / Model Day 223:0



ΔCH_4 [ppm]

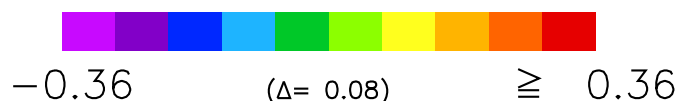


Figure 32: Comparison of measured and modeled CH_4 distributions for August 11, 1997 at 4.6 mbar. Shown are detrended values obtained by subtracting zonal averages at each latitude (“Eddy values”).

spondence between the main structures is found. The model captures, for example, the pronounced travelling planetary waves in the southern hemisphere and the strong extrusion of tropical air in the South American area discussed above.

5 Trace gas assimilation

5.1 The sequential approach

The aim of data assimilation is the construction of an optimum combination of *a priori* knowledge about a physical system (e. g. a model forecast) and observations of this system. For example, the UKMO meteorological fields are an optimum combination of measured winds and temperatures and values provided by a general circulation model. The advantage of these data for the generation of structures in constituents fields has been demonstrated in the previous chapter. However, for detailed studies of transport and photochemical processes it is useful to assimilate the measured trace gas concentrations themselves in the model, since this yields an even more realistic representation of the atmospheric state.

The CTM has therefore been used as the core of a trace gas assimilation system. In particular, a simple sequential assimilation method was developed, which combines CRISTA level 2 data (instrument sampling grid) with trace gas fields predicted by the CTM in the following manner: For CRISTA-1 the CTM is initialized on November 1 (Day 305:0) and calculates the synoptic evolution of the middle atmosphere. CRISTA measurements are available from November 4 (Day 308:17:35) on. After this date, the modeled trace gas distributions are sampled by the CRISTA observation grid. At each time step, mixing ratio values calculated by the model are updated at all locations where measurements are available. By using this approach, the trace gas assimilation system automatically accounts for the asynchronous nature of the CRISTA-1 measurements. Each measured value is used to update the model values at its four surrounding model grid points at the associated pressure level. The updates are weighted averages of the measured value and the corresponding model forecasts. For each of the surrounding grid points, the relative weight W of the measured value is calculated from its longitudinal ($\Delta\lambda$) and latitudinal ($\Delta\varphi$) distance as follows: $W = 1 - R$, $R = ((\Delta\lambda/\Delta\lambda_0)^2 + (\Delta\varphi/\Delta\varphi_0)^2)^{\frac{1}{2}}$, where $\Delta\lambda_0$ and $\Delta\varphi_0$ are the longitudinal and latitudinal resolution used for the model integration.

Due to the high data density of CRISTA, the distributions of long-lived trace gases are rapidly forced towards the observation, since all grid points are updated in about a day. This means that the CTM is continuously initialized by new data.

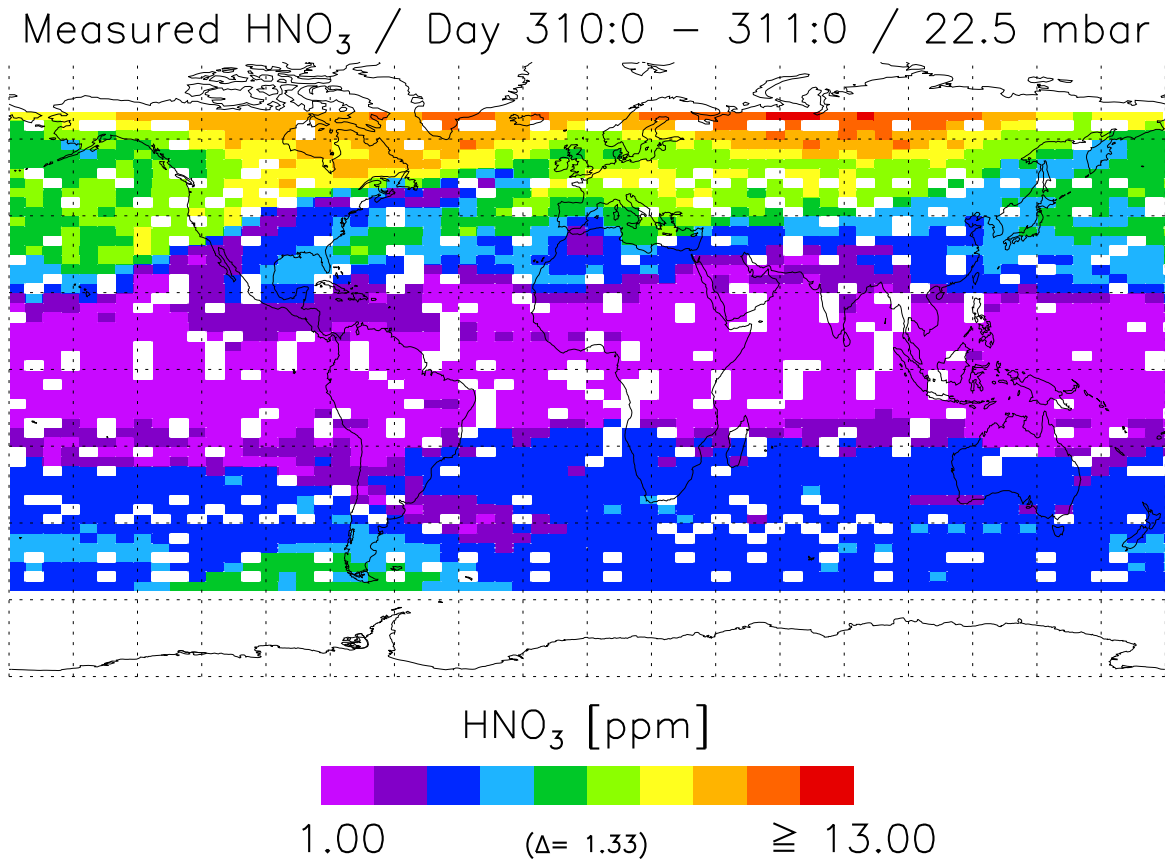


Figure 33: Mixing ratios of HNO_3 measured by CRISTA on November 6, 1994 at 22.5 mbar projected onto a regular CTM grid. (For details see text).

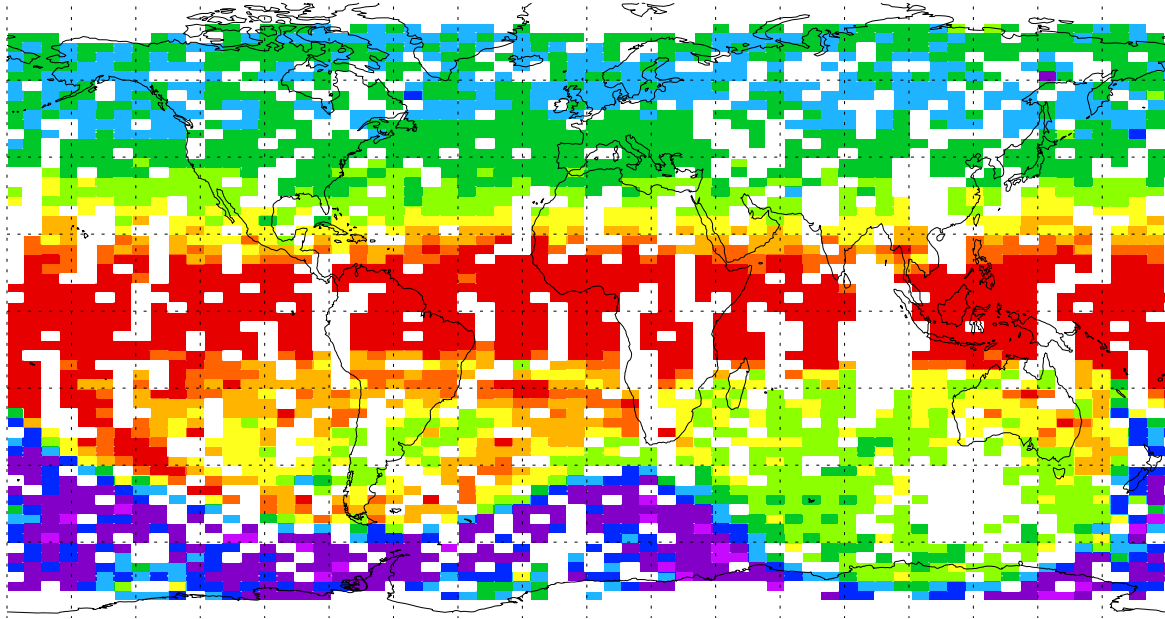
To illustrate the high CRISTA data density, Figure 33 shows HNO_3 observations for November 6, 1994 (Day 310:0 - 311:0) projected onto the horizontal model grid at the 22.5 mbar level. The observations were made using the high-resolution stratospheric measurement mode (see Table 1). The model resolution is 5.65° in longitude and 2.5° in latitude. It corresponds to the size of single colored (or blank) rectangles in Figure 33. Trace gas values (colored rectangles) are only given for those grid points which are the nearest neighbor of at least one observation. The figure suggests that the measurement net is somewhat less dense than the model grid. However, this is not the case. On average each grid point is the nearest neighbor of more than two observations. Grid points which are not the nearest neighbor of a measured point are also updated in the time period of Figure 33, because each observed value influences its four surrounding grid points (see above).

About one day after the first measured data are available, the model forecast essentially represents a temporal extrapolation of previous CRISTA measurements, and

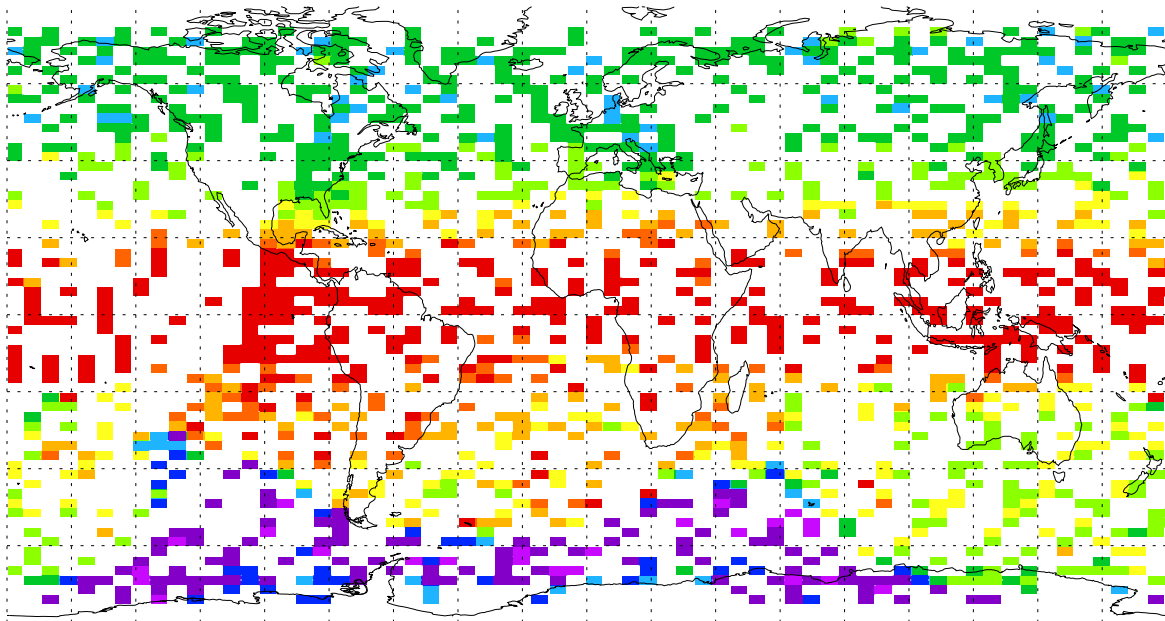
forecasts of the assimilation system become quite reliable. As a result, the analyzed maps of long-lived tracers become rather insensitive to changes of the weighting factors applied to the measurements and to the model forecasts. In a sensitivity study performed for CFC-11 at 46.4 mbar (see also Figure 11), the weighting factors for new measurements were reduced by a factor of two after Day 311:0. Nevertheless, the resulting CFC-11 values of Day 314:0 agree with the corresponding CFC-11 values of the standard approach typically to within 5%.

Trace gas assimilation can be considered as a means to enhance the spatial resolution of observations, e. g. for transport studies in the Eulerian framework (Section 5.2): Figure 34 shows measured CH_4 values at 4.6 mbar projected onto the horizontal model grid for two days of CRISTA-2 observations (August 11 and August 14, 1997). On August 11 the instrument was operated in a stratospheric mode. The data density is considerably higher during this day than three days later, when CRISTA focused on the mesosphere. In principle, the blank areas of Figure 34 could be filled with trace gas values by applying suitable spatial filters. The CH_4 distribution of Figure 24 was obtained, for example, by using a two-dimensional horizontal filter, which resembles a triangle function with a half width of 12° in longitude and a triangle with a width of 4° in latitude. However, application of such a spatial filter decreases the horizontal resolution of the trace gas field to the half width of the filter function. The sequential trace gas assimilation system, on the other hand, fills data gaps by model forecasts, which are essentially temporal extrapolations of previous observations. Corresponding (assimilated) CH_4 distributions are shown in Figure 35. Such distributions are ideally suited for analyses of to atmospheric transport processes at high horizontal resolution. Such work is already in progress for CRISTA-2. Results obtained for CRISTA-1 are discussed below.

Measured CH₄ / Day 222:12 – 223:12 / 4.6 mbar



Measured CH₄ / Day 225:12 – 226:12 / 4.6 mbar



CH₄ [ppm]

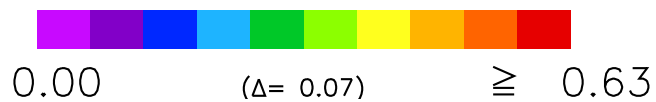
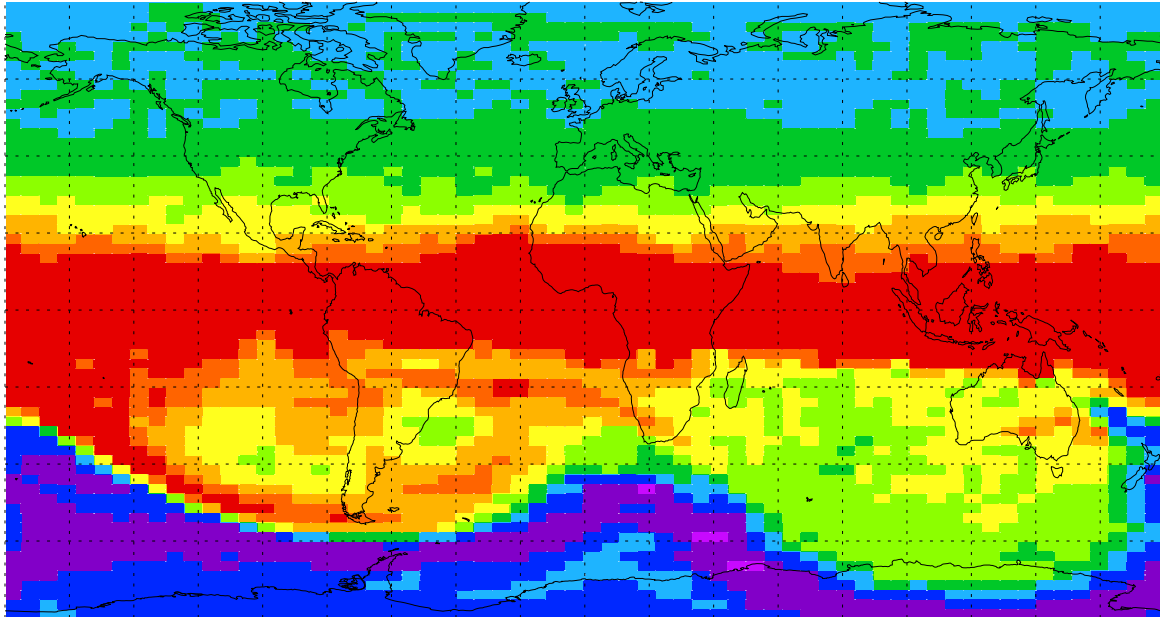
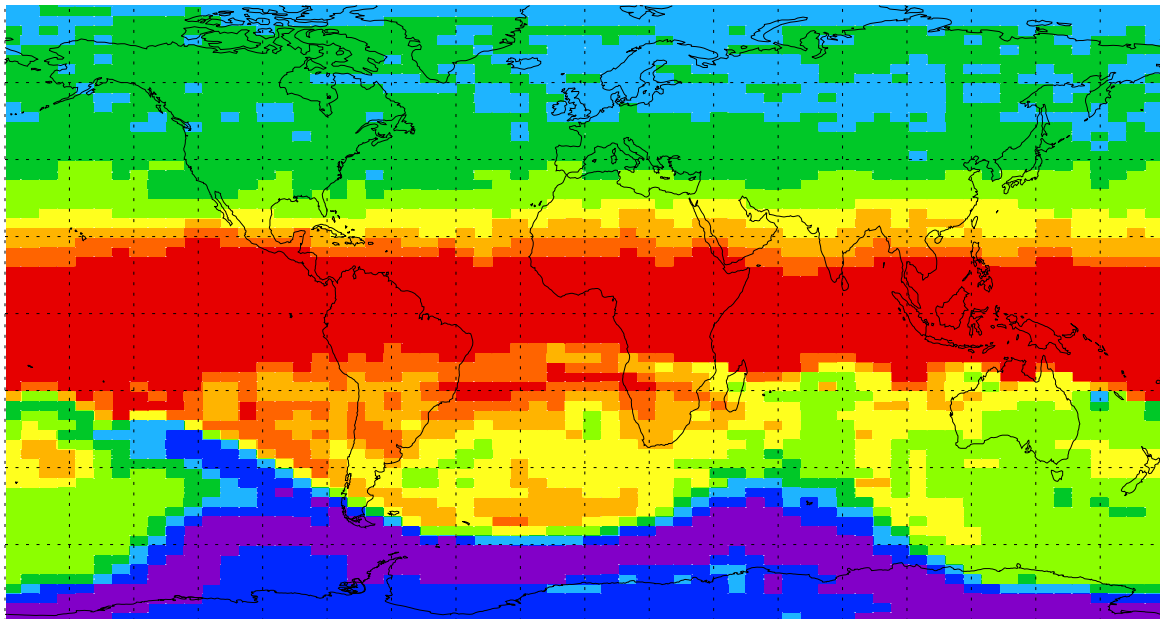


Figure 34: Mixing ratios of CH₄ measured by CRISTA on August 11 and August 14, 1997 at 4.6 mbar. The measurement points are projected onto the grid of the chemical transport model. (For details see text).

Analyzed CH₄ / Day 223:0 / 4.6 mbar



Analyzed CH₄ / Day 226:0 / 4.6 mbar



CH₄ [ppm]

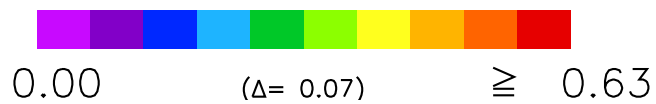


Figure 35: Analyzed (assimilated) CH₄ mixing ratios for August 11 and August 14, 1997 at 4.6 mbar. The values are shown at the resolution of the grid of the chemical transport model.

5.2 Transport studies based on assimilated trace gas fields

The main advantage of assimilated trace gas distributions is the availability of synoptic trace gas fields derived from observations on the temporal and spatial grid of the meteorological fields. This allows, for example, for quantitative studies of eddy fluxes and of their influence on the temporal evolution of the background atmosphere (hereafter “calculated tendencies”). The calculated tendencies may be compared to the measured temporal evolution of the zonal mean background field (hereafter “measured tendencies”) in order to test our understanding of the influence of dynamical structures on the temporal development of the background atmosphere. *Randel et al.* (1994) have calculated trace gas budgets for N₂O based on the transformed Eulerian-mean (TEM) conservation equation (Eq. 13) for zonal mean mixing ratios and modeled N₂O distributions (NCAR CCM2). The assimilated CRISTA data provide the opportunity to perform such an analysis based on observations.

TEM Framework

The analyses presented in this section are based on the transformed Eulerian-mean (TEM) conservation equation (Eq. 13) for zonal mean mixing ratios (*Andrews et al.*, 1987):

$$\frac{\partial \bar{\chi}}{\partial t} = -\bar{v}^* \frac{\partial \bar{\chi}}{\partial y} - \bar{w}^* \frac{\partial \bar{\chi}}{\partial z} + \bar{S} + \frac{1}{\rho} \nabla \cdot \mathbf{M} \quad (13)$$

The quantity on the left side of Equation 13 ($\partial \bar{\chi} / \partial t$) is the mixing ratio tendency. Forcing terms for Equation (13) include advection represented here by the residual mean circulation (\bar{w}^*, \bar{v}^*) , defined as

$$\bar{w}^* = \bar{w} + \frac{1}{a \cos \varphi} \frac{\partial}{\partial \varphi} \left(\cos \varphi \frac{R \overline{v'T'}}{H N^2} \right) \quad (14)$$

$$\bar{v}^* = \bar{v} - \frac{1}{\rho} \frac{\partial}{\partial z} \left(\rho \frac{R \overline{v'T'}}{H N^2} \right) \quad (15)$$

with:

R	gas constant
H	scale height
N	Brunt-Väisälä frequency
a	Earth's radius
φ	latitude
z	altitude
v	meridional velocity
w	vertical velocity
ρ	atmospheric density

The source term \bar{S} in Equation 13 accounts for the photochemical production (and loss), and \mathbf{M} is the eddy flux vector with horizontal and vertical components given by

$$M_y = -\rho \left(\overline{v'\chi'} - \frac{R}{H} \frac{\overline{v'T'}}{N^2} \bar{\chi}_z \right) \quad (16)$$

$$M_z = -\rho \left(\overline{w'\chi'} - \frac{R}{H} \frac{\overline{v'T'}}{N^2} \bar{\chi}_y \right) \quad (17)$$

Overbars denote zonal means. Primes denote deviations from the zonal mean values.

CFC-11 fluxes at 31.6 mbar

The assimilated CRISTA distributions are ideally suited for analyses of transport processes, since all information needed to evaluate Equations 13 to 17 is available at each time step of the model. Figure 36a shows a comparison of the meridional CFC-11 eddy flux ($-\frac{1}{\rho}M_y$) at 31.6 mbar derived from the analyzed CRISTA measurements and from the UKMO winds and temperatures (solid curve) with the corresponding values provided by the model without data assimilation (dashed curve) for November 6 (Day 310:0). The general meridional distribution of the CFC-11 fluxes is quite similar, however, the flux derived from the analyzed data being somewhat larger at middle latitudes. The underestimation of the eddy flux in the simulation without trace gas assimilation represents an additional manifestation of the fact that the strengths of synoptic-scale structures is underestimated in trace gas simulations based on meteorological wind fields alone.

At 30° N, the longitudinal interval of the subtropical extrusion (140°E to 120°E, see Figure 28) represents only about 6% of the latitudinal circle. Nevertheless, it contributes about 25% to the measured eddy flux (not shown here). This underlines

the importance of planetary-scale tongues for the exchange of tropical and extra-tropical air.

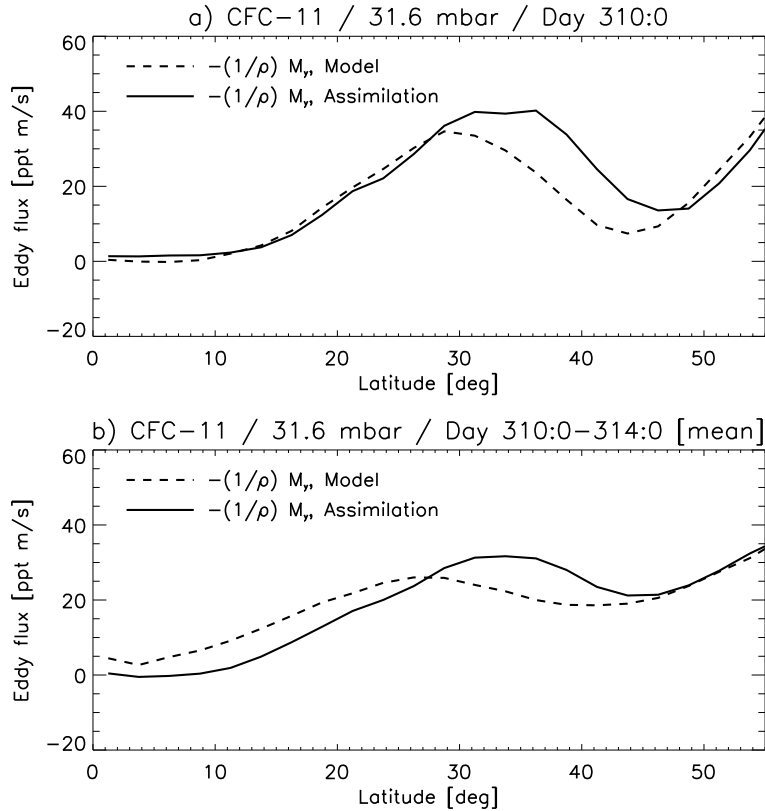


Figure 36: Comparison of the meridional CFC-11 flux derived from assimilated CRISTA data (solid curve) for November 6 (Day 310:0) at 31.6 mbar with the respective CFC-11 flux derived from model simulations without trace gas data assimilation (dashed curve). The top panel shows eddy fluxes on November 6 (Day 310). The lower panel shows mean values for the time period from November 6 to November 10 (Day 310:0 to Day 314:0).

Figure 36b shows mean CFC-11 eddy fluxes for the time period from Day 310:0 to Day 314:0. The fluxes have been calculated with a temporal resolution of one day. Figure 36b shows averages of the values obtained for the single days. The mean flux of the model is somewhat overestimated in the equatorial region (due to the higher variability of the CFC-11 mixing ratios). It is smaller northward of about 30° N, since the modeled structures are less pronounced at higher latitudes. In comparison to the single day observation (Figure 36a), the mean curves are flattened. This means that large parts of the CFC-11 mixing ratio tendencies associated with the fluxes of single days cancel when averaged over longer time periods. This finding confirms the analysis

of *Randel et al.* (1994), who also find a large degree of reversibility of transport effects during wave disturbed periods in their analysis of CCM2 simulations.

CH₄ Budget at 4.6 mbar

The assimilated CRISTA data provide for the first time the opportunity to perform a global trace gas budget analysis for a relatively short time period (about one week) based on observations. As an example, CH₄ distributions at 4.6 mbar are studied here, since strong irreversible mixing processes appear to be present in the CH₄ field at this altitude (Figure 37). On November 6 (Day 310), an air mass of CH₄ rich air is being separated from the air mass of the associated tropical extrusion (in the Atlantic off the coast of Nova Scotia). During the following days, this air mass moves eastward and starts to circle around the north polar vortex. On November 12 (Day 316) it is mixed into another air mass that extends along the Pacific coast. Parts of the large air mass of CH₄ rich air, which is located over the Pacific Ocean, are drawn through the southern United States towards the Atlantic. During the following days, there are complex interactions with the polar extrusions of CH₄ poor air.

In addition to examples of transport from the tropics into middle latitudes, which have also been shown in previous studies (e. g. *Randel et al.*, 1993), the trace gas distributions of Figure 37 indicate a pronounced transport in the opposite direction. It can be seen that CH₄ poor air is transported from middle latitudes into the tropics at and below 40° N, 110° E (Days 310 to 312). After November 8 (Day 312) an air mass of relatively low CH₄ mixing ratios is located at 20° N, 90° E, and is surrounded by air of higher mixing ratios. Thus, the time sequence of the analyzed data suggests that irreversible mixing occurs.

The situation shown in Figure 37 has been investigated by means of the TEM equation. Figure 38 compares measured CH₄ (4.6 mbar) tendencies ($\partial\bar{\chi}/\partial t$, solid curve) to tendencies calculated from the sum of all terms on the right of Equation 13 at 4.6 mbar. The calculation of transport terms (right side of Eq. 13) is based on CRISTA trace gas structures and UKMO wind and temperature fluctuations obtained from synoptic fields. The measured tendencies have been determined by comparing zonal mean CH₄ values of Day 310:0 to respective values of Day 314:0. The divergence of the eddy flux and the effects of the residual mean circulation have been calculated with a

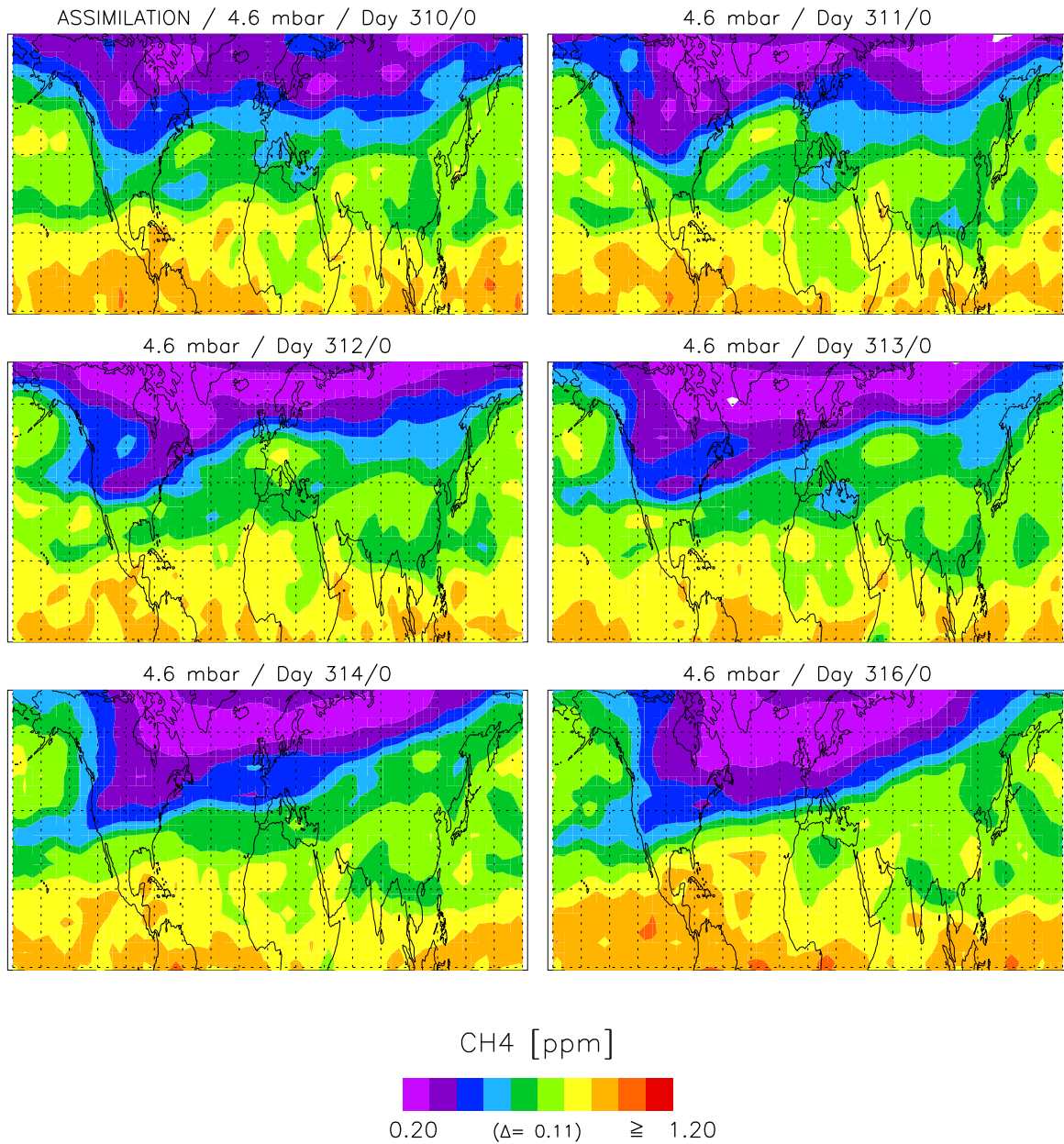


Figure 37: Time sequence of assimilated CH₄ data of CRISTA at 4.6 mbar. Data are shown for November 6, 7, 8, 9, 10 and 12, 1994. (For details see text.)

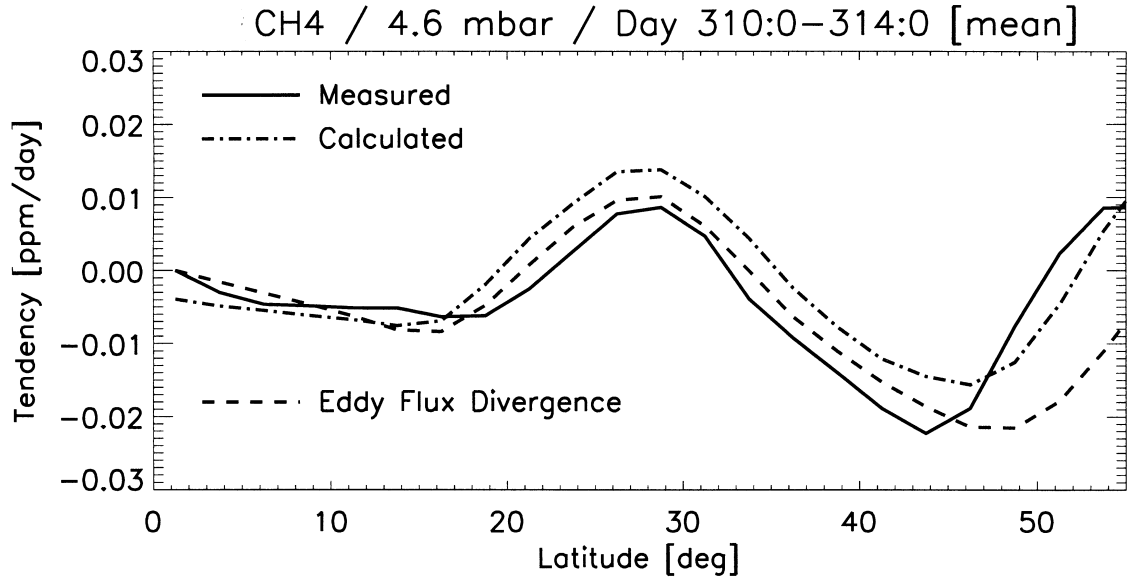


Figure 38: Comparison of measured zonal mean tendencies of CH₄ mixing ratios (solid curve) with calculated tendencies. The calculation includes all terms from the right side of Equation 13. In addition, effects of eddy transport are shown by the dashed curve.

temporal resolution of one day. Figure 38 shows averages obtained for the time period from Day 310:0 to 314:0. Effects of the eddy flux divergence (predominantly $\frac{1}{\rho} \partial M_y / \partial y$) are much larger than effects of the residual mean circulation and of photochemical production and loss at this altitude. The relative latitudinal shape of the measured and the calculated tendencies are in reasonable agreement. A relative minimum at 20° N shows up in the measured tendencies as well as in the calculated tendencies. It is related to the transport process from middle latitudes to the tropics. Measured zonal mean mixing ratio tendencies are about -0.007 ppm/day at 18.75° N (Figure 38). A longitudinal plot at this latitude shows that the largest tendencies (-0.03 ppm/day) occur in a longitudinal band of about 50° width centered around 80° E (see Figure 37).

Figure 38 demonstrates the feasibility of trace gas budget studies based on assimilated high resolution trace gas fields even for relatively short observation periods of about a week. In future analyses, the diagnostic tools developed for CRISTA will be applied to long term series of assimilated ENVISAT trace gas fields in order to derive seasonal cycles and latitudinal variations of trace gas eddy flux divergences and effects of the mean meridional circulation on the background atmosphere.

5.3 Modeling of chemically active species

Comparisons of global observations of chemically active species with results of three-dimensional simulations are often hampered by an inadequate representation of dynamical processes in the model. As described in this section, a reasonable separation of dynamical effects and photochemical effects can be obtained by sequential assimilation of long-lived tracers and chemical families. The resulting global distributions of the long-lived species account for the dynamical conditions prevalent during the observational period of a given instrument, i. e. for the important dynamical structures, thereby providing useful constraints for simulations of chemically active species. Through such an approach, the relative contributions (partitioning) of chemically active species to their chemical families may be studied under realistic conditions. A detailed understanding of the partitioning of chemical families such as total nitrogen (NO_y) is especially important, for example, for the assessment of chemical ozone losses.

Stratospheric ozone losses result primarily from catalytic cycles involving odd nitrogen, odd chlorine, odd hydrogen, and odd bromine. Reactions involving odd nitrogen ($\text{NO}_x = \text{NO} + \text{NO}_2$) species are the dominant stratospheric ozone sink above ~ 25 km altitude (e. g. *Crutzen, 1970; Brasseur et al., 1997*). For this reason, a detailed understanding of the partitioning of the nitrogen family is crucial for quantitative determinations of ozone destruction rates. The nitrogen partitioning can be significantly influenced by heterogeneous reactions (e. g. *Solomon et al., 1996*). For example, heterogeneous hydrolysis of N_2O_5 is an important sink of NO_x in the lower stratosphere (e. g. *Fahey et al., 1993*). The reaction also substantially alters the effect of other cycles since the ratios of odd hydrogen members (OH/HO_2) and of odd chlorine members ($\text{ClO}/\text{ClONO}_2$) are controlled by NO_x .

Analyses of the nitrogen partitioning have been performed based on aircraft and balloon observations with limited geographical coverage (e. g. *Salawitch et al., 1994; Sen et al., 1998*). The results suggest that the partitioning of NO_y species (total nitrogen) relevant for stratospheric ozone destruction is reasonably well understood, at least for conditions with high aerosol loadings. Analyses of satellite data provide global coverage and reveal a gradual increase of the NO_y/NO_x ratio in the post-Pinatubo stratosphere, consistent with model predictions (e. g. *Morris et al., 1997; Danilin et*

al., 1999). However, the nitrogen partitioning obtained from satellite observations to date has only been investigated in terms of zonally averaged values or single profile data based on box models or two-dimensional models. The sequential assimilation approach presented here allows for three-dimensional simulations of chemical processes observed by CRISTA.

Assimilation of chemical families

The technique described here is an extension of the trace gas assimilation technique (Section 5.1) to chemical families (NO_y , Cl_x , O_x). It is used to constrain simulations of chemically active species such as N_2O_5 and NO_2 . The assimilation is based on the “observed” mixing ratios of families, which are estimated from measurements of individual components. The reactive nitrogen reservoir (NO_y) is estimated, for example, from the observed nitrogen components (NO_y^i) and the relative contributions (α_i) of each component to total NO_y as predicted by the model. The model predictions of the relative contributions (α_i) of the individual family members NO_y^i (NO_2 , HNO_3 , N_2O_5 , and ClONO_2 for CRISTA-1) are evaluated at the locations (altitude z , longitude λ , latitude ϕ) and the local solar times (LST) of the observations. The “observed” NO_y mixing ratio is estimated for each measured nitrogen component NO_y^i separately based on the predicted relative contribution (α_i). This yields four different estimates of the “observed” NO_y amount, one for each observed component. The best estimate of the “observed” NO_y value is obtained by weighting the different estimates inversely with their variance σ^2 . Finally, the best estimate for NO_y is inserted into the model by using the sequential assimilation procedure. The mixing ratio values of the family members are adjusted according to the updated NO_y value. The relative partitioning remains unchanged.

Since the observed NO_y members (NO_2 , HNO_3 , N_2O_5 , and ClONO_2) are not directly inserted into the model, their values will only be in good agreement with corresponding model results, if the partitioning ratios predicted by the model are in good agreement with the partitioning ratios measured by CRISTA. The model predictions of the nitrogen partitioning are basically a function of the atmospheric aerosol loading and kinetic parameters of key gas-phase reactions (e. g. $\text{R}_1: \text{NO}_2 + \text{OH} + \text{M} \rightarrow \text{HNO}_3$; $\text{R}_2: \text{OH} + \text{HNO}_3 \rightarrow \text{NO}_3 + \text{H}_2\text{O}$). As discussed by *Osterman et al.* (1999), gas-phase kinetic parameters of *DeMore et al.*, (1994) result in better

agreement between modeled and observed nitrogen species than kinetic parameters provided by *DeMore et al.*, (1997), mainly due to a slower rate of reaction R_1 . Recent studies (e. g. *Gao et al.*, 1999) demonstrate that best agreement is achieved when using newly measured rate constants (*Brown et al.*, 1999 a,b) for reaction R_1 and R_2 . To test the sensitivity of the modeled nitrogen species to the aerosol loading and the values of the kinetic parameters, four test cases have been defined: Case A_1 is based on the newly measured rate constants and aerosol surface densities obtained from SAGE II observations carried out in October, 1994; in case A_2 heterogeneous reactions are neglected; case B_1 uses the newly measured rate constants and aerosol loadings provided by HALOE; case B_2 is based on HALOE aerosol and kinetic parameters of the JPL-94 compilation.

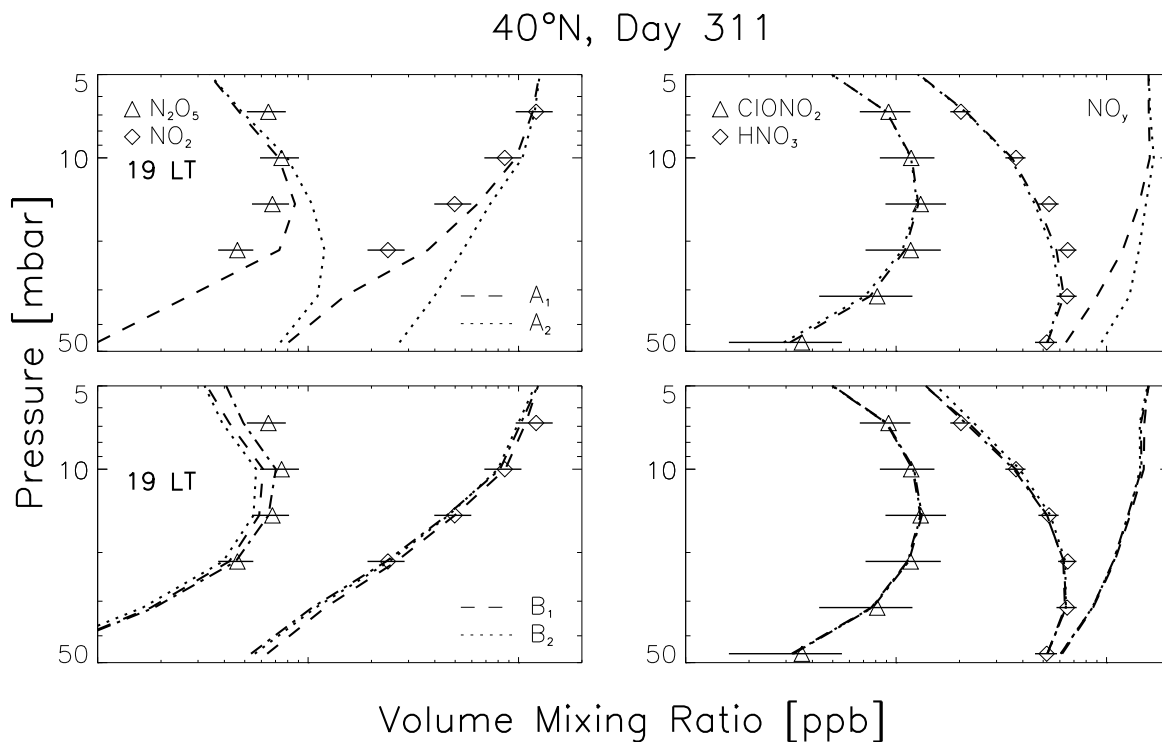


Figure 39: Comparison of measured (symbols) and simulated zonal mean profiles (30°N to 50°N) of nitrogen components for early nighttime conditions (19 LT). The left panel shows results for N_2O_5 and NO_2 , while the right panel contains $ClONO_2$, HNO_3 , and NO_y values. For details concerning the model cases A_1 , A_2 , B_1 , and B_2 see text. (Figure 2 of *Riese et al.*, 2000b).

Comparisons of measured (symbols) and modeled (lines) mixing ratio profiles of four nitrogen components are presented in Figure 39. Mid-latitude (30°N to 50°N) zonal averages calculated from individual profile measurements and corresponding

model forecasts of the constrained model are shown for early nighttime conditions (19 LT). The upper panel of Figure 39 demonstrates the importance of heterogeneous reactions on sulfate aerosols at altitudes below 10 mbar (30 km). The neglect of heterogeneous reactions in case A₂ results in a considerable overestimation of the amounts of N₂O₅ and NO₂. More realistic results are obtained in cases A₁ and B₁. Compared to the strong influence of the aerosol loading assumed for the simulations, the sensitivity of N₂O₅ and NO₂ on assumptions made for the gas-phase rate constants (case B₂) is rather small.

The local solar time (LST) distribution shown in Figure 15 indicates that most information about diurnal variations of chemically active species is contained in observations performed in the latitudinal regions of the northern and southern turning points of the orbital tracks. Figure 40a shows CRISTA values of NO₂ at 3.16 mbar measured during the time period from day 308/1734 to day 314/0354 in the latitudinal band from 30°N to 50°N (orange points). Note that observations of other nitrogen species are not available at this altitude level. The LST coverage of the combined measurements of the three telescopes is about 12 hours. It includes the day to night transition (terminator), where steep gradients in the diurnal variation of NO₂ occur. The large scatter of the observation is mainly due to intense zonal variations caused by dynamical processes. As discussed above, the CRISTA observations were performed during a dynamically disturbed period characterized by intense wave activity and exchange of tropical air and extra-tropical air, for instance, in the form of planetary-scale tongues. Figure 40a also shows observed values averaged over the time step (20 min) of the model (black symbols). The observations are compared to a zonally averaged diurnal cycle obtained from the model (orange line). The night/day ratio is of the order of 3-4 for both model result and observation. However, the transition from day to night is somewhat steeper in the measurement. Simulated values of unmeasured species such as NO_x (NO₂+NO), HNO₃, ClONO₂, and N₂O₅ are also shown in Figure 40a. Figure 40b presents the same comparisons at 10 mbars, where CRISTA observations of NO₂, HNO₃, N₂O₅, and ClONO₂ are available. Shown are averaged values for all species as well as single observations of HNO₃ (green points) and ClONO₂ (violet points). At this pressure level, the night/day ratio of NO₂ is larger in the observation than in model case B₁.

Comparisons of horizontal distributions of measured and modeled (case B₁) NO_y

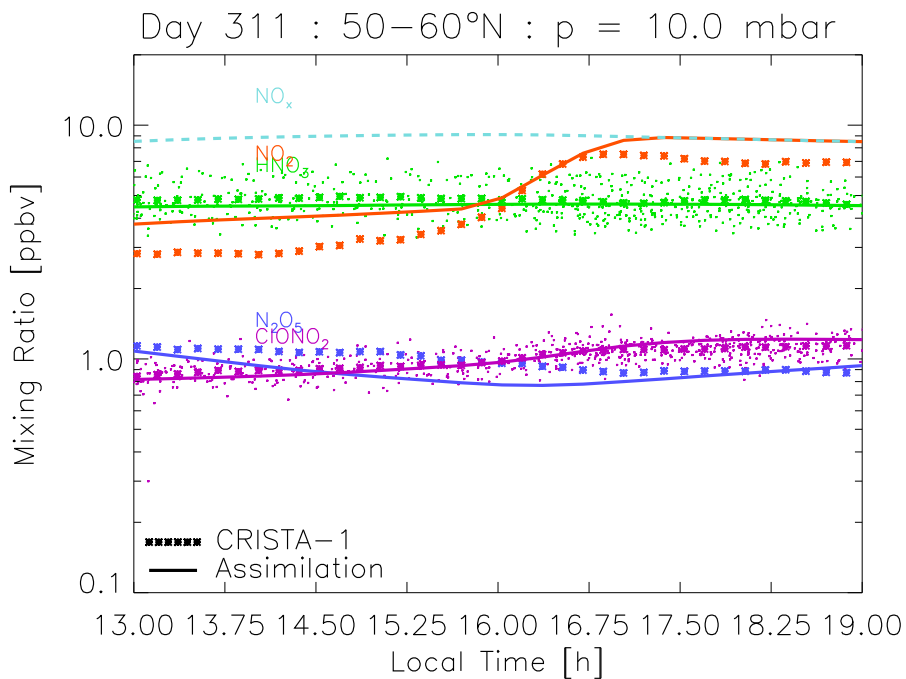
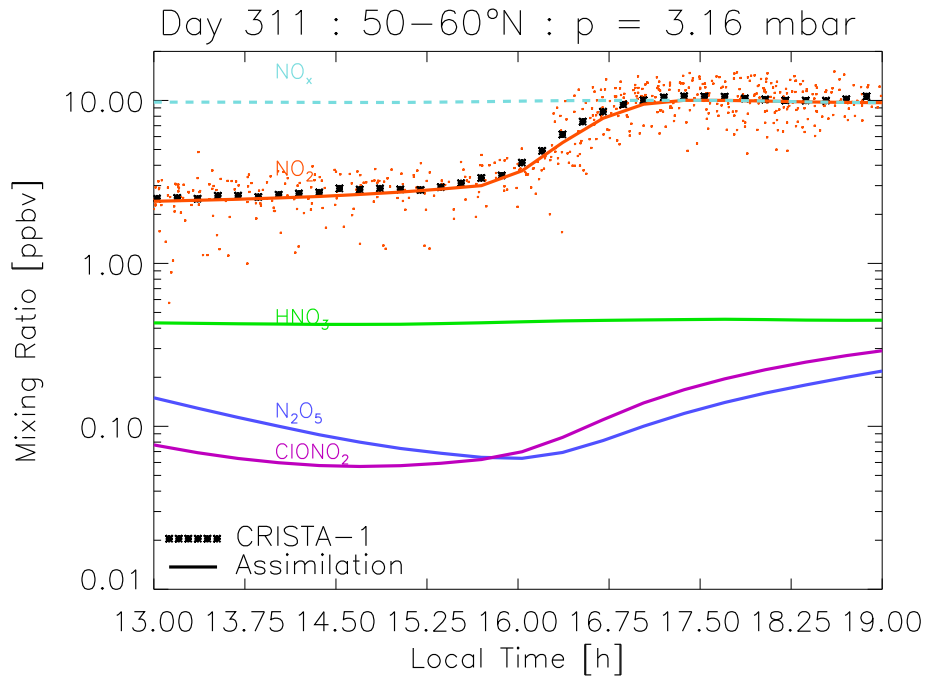


Figure 40: **(a)** Comparison of measured and modeled diurnal variations of nitrogen species at 3.16 mbar (50°N to 60°N). Single observations of NO_2 are given by orange points. Mean observed NO_2 values are also shown (black symbols). Corresponding zonally averaged model results are given by colored lines (orange: NO_2 , green: HNO_3 , blue: N_2O_5 , violet: ClONO_2). For more details see text. **(b)** Same as (a) but for the 10 mbar level. Single observations are shown for HNO_3 (green points) and ClONO_2 (violet points). Mean observed values are also shown (colored symbols). (Figure 3 of *Riese et al.*, 2000b).

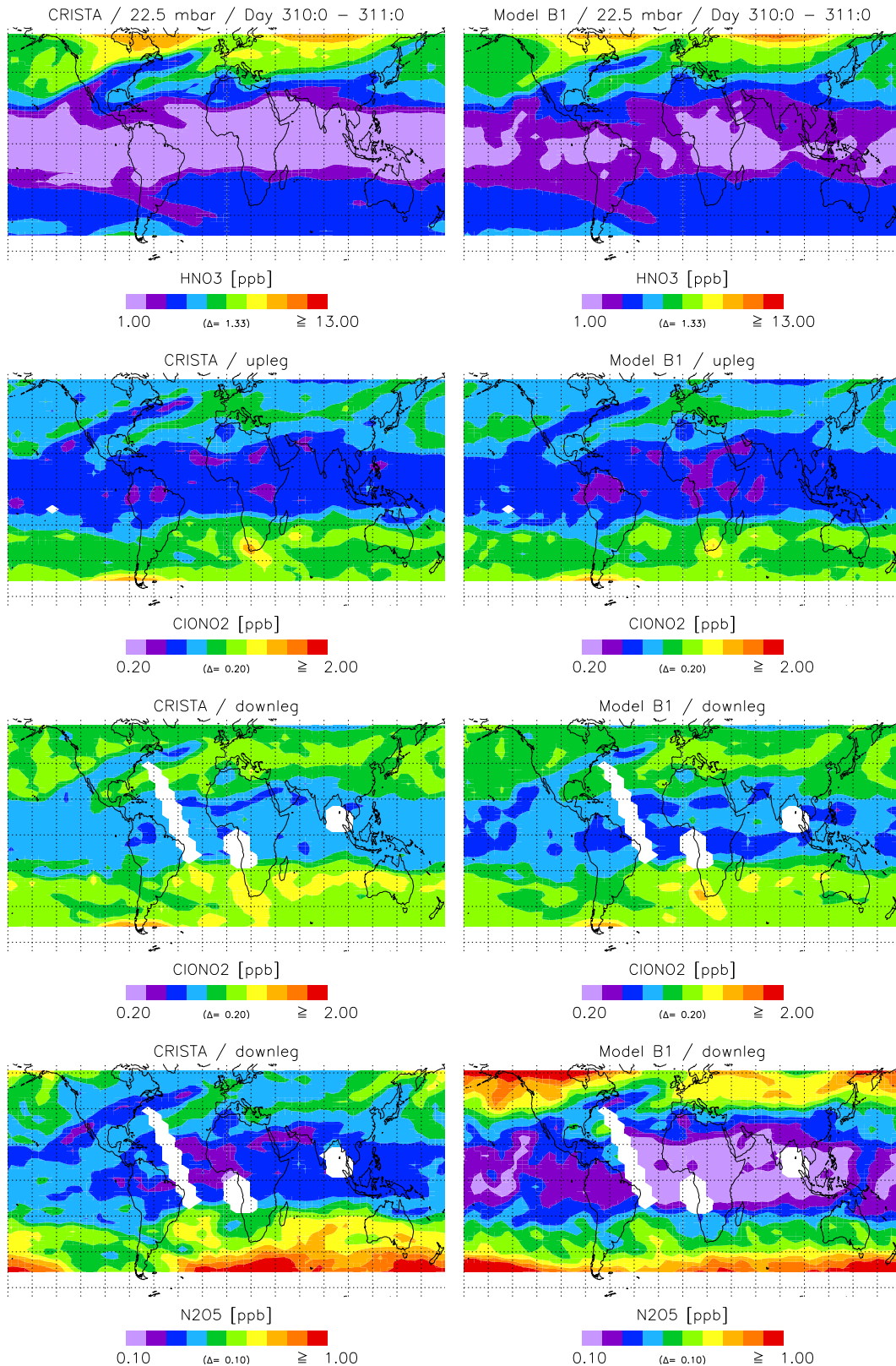


Figure 41: Comparison of measured and modeled nitrogen species for November 6, 1994 at 22.5 mbar (25 km). Shown are distributions of HNO₃, CIONO₂ (upleg), CIONO₂ (downleg), and N₂O₅ (downleg). (Figure 4 of *Riese et al.*, 2000b).

species are shown in Figure 41 for November 6 (day 310) at 22.5 mbar. The left panel shows the observation, while the right panel shows the model forecast (before NO_y is updated by new observations) at the instrument sampling grid, i. e. at the locations and times of the observations. One day of observations (day 310:0 to day 311:0) is shown. The HNO_3 distributions (upper panel) contain all measurement points of November 6, since no major diurnal variations are present at this altitude level. For ClONO_2 , observations on the upleg were separated from observations on the downleg (second and third panel). For N_2O_5 only measurements on the downleg are shown.

For HNO_3 the shape of the polar vortex is well reproduced by the model. In the northern hemisphere two pronounced planetary-scale tongues can be seen in both observations and model results. Another weaker tongue of tropical air extends across the South American continent into the Indian Ocean. The overall agreement of the observed and modeled structures is remarkable. The most notable difference concerns the overestimation of HNO_3 by the model in the tropics. The observed distributions of ClONO_2 exhibit important diurnal variations, which are well reproduced by the model. The model also reproduces significant horizontal structures at middle latitudes, which resemble the structures observed in HNO_3 . In the case of N_2O_5 the overall agreement is considerably worse. In particular, the model overestimates the amount of N_2O_5 at high latitudes, probably due to an underestimate of the aerosol loadings. This discrepancy becomes even larger when using aerosol loadings provided by SAGE II (case A_1).

6 Summary

The CRISTA experiment provided high-quality limb observations of atmospheric infrared emission with high spatial resolution. The inversion of these observations to atmospheric temperature and trace gas distributions is based on an efficient data system. The fast measurement technique of CRISTA results in a large amount of radiance data. The radiative transfer calculations required to retrieve atmospheric pressures, temperatures, and trace gas mixing ratios (level 2 data) are very complex and several iterations of the whole retrieval process have to be performed in order to achieve high-quality retrieval results. The CRISTA forward radiance model therefore uses fast radiative transfer codes based on pre-calculated atmospheric emissivity lookup tables which account for the details of the CRISTA spectroscopy. The forward model is the core of a multiple-emitter multiple-spectral sampling point onion-peeling algorithm, which proved to be well suited to resolve horizontal and vertical atmospheric structures.

CRISTA provides information on the most prominent atmospheric wave types, e. g. on thermal tides and on planetary waves. Temperatures measured by CRISTA-1 (November 1994) show pronounced tidal structures which can be described by the linear theory as implemented in the GSWM (Global Scale Wave Model, Hagan et al., 1995). Planetary wave-two signatures observed during CRISTA-2 are consistent with those expected from a migrating planetary wave with an ozone signature, which is dynamically driven at lower altitudes (below 35 km) and photochemically driven at higher altitudes. CRISTA results above the middle stratosphere show a better agreement with photochemical equilibrium calculations than previous analyses.

CRISTA observations are especially suited for analyses of atmospheric transport processes. In the equatorial stratopause region (50 km) circulation cells arising from inertially unstable conditions were present during the CRISTA-1 observation period. Two separate circulation cells in different longitude bands with opposite phases were observed. Another new finding is that the upper stratospheric circulation cell appears to be linked to a lower-stratosphere Kelvin wave with a zonal wavenumber of one. Since the Kelvin wave has about the same vertical scale as the circulation cells (~ 10 km), and is approximately in phase with it, interactions between these two dynamical features may have occurred. The vertical motion associated with the Kelvin

wave could have affected the inertially unstable flow, e. g. by controlling its vertical scale. The temperature perturbations observed by CRISTA are rather small and may have been below the detection limit of previous observations. Circulation cells arising from inertially unstable conditions could be more common than previous studies would indicate and thus play a significant role for tracer transport in this atmospheric region.

High resolution stratospheric trace gases distributions measured by CRISTA are ideally suited for studies of stratospheric transport related to planetary wave activity, especially when they are used in conjunction with a three-dimensional transport model. The CRISTA missions took place during periods of disturbed dynamical conditions characterized by relatively large wave activity and associated exchange of tropical and extra-tropical air. As a result, numerous small and medium-scale structures were present in the trace gas distributions measured by CRISTA. The detailed structure of the observed constituent distributions has been modeled with the NCAR ROSE chemical transport model. The modeled trace gas distributions capture most of the measured planetary-scale and medium-scale structures, especially at high and middle latitudes.

For quantitative studies of transport and photochemical processes the ROSE CTM has been used as the core of a sequential data assimilation system. Sequential assimilation of long-lived species and chemical families appears to be an attractive technique to create synoptic trace gas fields from asynoptic satellite observations. The assimilation system provides synoptic distributions that are consistent with the CRISTA measurements at each time step of the model (20 min). Data gaps are filled and the measured trace gas distributions are extrapolated towards higher latitudes. The assimilation system provides, in addition, distributions of unmeasured species (consistent with the measurements). The main advantage of assimilated trace gas distributions is the availability of synoptic trace gas fields derived from observations on the temporal and spatial grid of the meteorological fields. This allows, for example, for quantitative studies of eddy fluxes and of their influence on the temporal evolution of the background atmosphere. Horizontal eddy fluxes of CFC-11 (31.6 mbar) calculated for CRISTA-1 from the assimilated trace gas concentrations are in reasonable agreement with respective fluxes calculated from modeled trace gas fields without data assimilation. Both data sets indicate a large degree of temporal cancellation of eddy

transport during the time period of the CRISTA-1 measurements. A study of the CH_4 budget at 4.6 mbar indicates that irreversible transport processes are rather important at this pressure level during the time period of the CRISTA-1 measurements. Most interesting is a pronounced mixing event from mid-latitudes into the tropics, which is also evident in measured and calculated zonal mean CH_4 mixing ratio tendencies.

To study chemical processes of short-lived species under realistic conditions, the assimilation system has been extended to chemical families such as NO_y , Cl_x , and O_x . Through this approach, simulations of short-lived species such as N_2O_5 and NO_2 can be constrained by CRISTA observations of long-lived species, and total amounts of chemical families, derived from measurements of individual family members. This allows for meaningful comparisons of measured and modeled short-lived species. In the present case, the approach has been successfully used to perform a study of the partitioning ratios of the nitrogen family. In particular, the dependence of the partitioning on assumptions made for the aerosol loading and key gas-phase reaction rates was investigated. Very good agreement between measured and modeled fields was found in terms of significant diurnal variations and large longitudinal variations. Sequential assimilation of chemical families appears to be an attractive method to investigate global fields of chemically active species provided by satellite observations, thereby testing our current understanding of photochemical processes.

Acknowledgement

My sincerest thank goes to D. Offermann for his invaluable support during all phases of this thesis. I would also like to thank Guy Brasseur, Xuexi Tie, and Anne Smith for their helpful and friendly collaboration in interpreting and modeling the CRISTA data. Anne Smith's comments on the first draft of this thesis are gratefully acknowledged. I also wish to thank Larry Gordley for his support in the CRISTA retrieval and for many helpful discussions. The CRISTA project was supported by grant 50 OE 8503 of DARA (Deutsche Agentur für Weltraumangelegenheiten), Bonn, Germany. The data evaluation of the second CRISTA mission is supported by grant 50 QV 9802 4.

7 References

- Andrews, D. J., J. R. Holton, and C. B. Leovy, Middle Atmosphere Dynamics, Int. Geophys. Ser., Academic Press, San Diego, USA, 1987.
- Bacmeister, J. T., S. D. Eckermann, P. A. Newmann, L. Lait, K. R. Chan, M. Loewenstein, M. H. Proffit, and B. L. Gary, Stratospheric horizontal wavenumber spectra of winds, potential temperature, and atmospheric tracers observed by high-altitude aircraft, *J. Geophys. Res.*, *101*, 9441–9470, 1996.
- Bacmeister, J. T., V. Küll, D. Offermann, M. Riese, and J. W. Elkins, Intercomparison of satellite and aircraft observations of ozone, CFC-11, and NO_y using trajectory mapping, *J. Geophys. Res.*, *104*, 16,379–16,390, 1999.
- Beer, R., Tropospheric Emission Spectrometer: Scientific objectives and approach, goals and requirements, D-11294, JPL, 1996.
- Brasseur, G. and S. Solomon, Aeronomy of the middle atmosphere, (second edition), D. Reidel Publishing Company, Boston, 1986.
- Brasseur, G., D. Cariolle, A. D. Rudder, L. J. Gray, J. A. Pyle, E. P. Röth, U. Schmailzl, and D. J. Wuebbles, Odd nitrogen during the MAP/GLOBUS 1983 campaign: Theoretical considerations, *Planet. Space Sci.*, *35*, 637–645, 1987.
- Brasseur, G., M. H. Hitchman, S. Walters, M. Dymek, E. Falise, and M. Pirre, An interactive chemical dynamical radiative two-dimensional model of the middle atmosphere, *J. Geophys. Res.*, *95*, 5639–5655, 1990.
- Brasseur, G. P., X. X. Tie, P. J. Rasch, and F. Lefèvre, A three-dimensional simulation of the Antarctic ozone hole: Impact of anthropogenic chlorine on the lower stratosphere and upper troposphere, *J. Geophys. Res.*, *102*, 8909–8930, 1997.
- Brasseur, G. P., J. J. Orlando, and G. S. Tyndall, Atmospheric Chemistry and Global Change, Oxford University Press, USA, 1999.
- Brown, S. S., K. Talukdar, and A. R. Ravishankara, Rate constants for the reaction $\text{OH} + \text{NO}_2 + \text{M} \rightarrow \text{HNO}_3 + \text{M}$ under atmospheric conditions, *Chem. Phys. Lett.*, *299*, 277–284, 1999a.
- Brown, S. S., K. Talukdar, and A. R. Ravishankara, Reconsideration of the rate constant for the reaction of hydroxyl radicals with nitric acid, *J. Phys. Chem.*, *103*, 3031–3037, 1999b.
- Conway, R. R., M. H. Stevens, C. M. Brown, J. G. Cardon, S. E. Zasadil, and G. H. Mount, Middle Atmosphere High Resolution Spectrograph Investigation, *J. Geophys. Res.*, *104*, 16,327–16,348, 1999.
- Chapman, S., and R. S. Lindzen, Atmospheric tides, D. Reidel, Norwell, Mass., USA, 1970.
- Charney, J. G., and P. G. Drazin, Propagation of planetary-scale disturbances from the lower into the upper atmosphere, *J. Geophys. Res.*, *66*, 83–108, 1961.
- Chen, P., and J. R. Holton, A. O'Neill, and R. Swinbank, Quasi-horizontal transport and mixing in the Antarctic stratosphere, *J. Geophys. Res.*, *99*, 16,851–16,866, 1994.
- Chipperfield, M., Multiannual simulations with a three-dimensional chemical transport model, *J. Geophys. Res.*, *104*, 1781–1806, 1999.

- Crutzen, P. J., The influence of nitrogen oxides on the atmospheric ozone content, *J. R. Meteorol. Soc.*, *96*, 320-325, 1970.
- Danilin, Y. M. et al., Nitrogen species in the post-Pinatubo stratosphere: Model analysis utilizing UARS measurements, *J. Geophys. Res.*, *104*, 8247-8262, 1999.
- DeMore, W. B. et al., Chemical kinetics and photochemical data for use in stratospheric modeling, *JPL Publ. 94-26*, 1994.
- DeMore, W. B. et al., Chemical kinetics and photochemical data for use in stratospheric modeling, *JPL Publ. 97-4*, 1997.
- Douglass, A. R., C. J. Weaver, R. B. Rood, and L. Coy, A three-dimensional simulation of the ozone annual cycle using winds from a data assimilation system, *J. Geophys. Res.*, *101*, 1463-1474, 1996.
- Drummond, J. R., J. T. Houghton, G. D. Peskett, C. D. Rodgers, M. J. Wale, J. G. Whitney, and E. J. Williamson, The Stratospheric and Mesospheric Sounder on Nimbus 7, *Phil. Trans. Roy. Soc. Lond.*, A 296, 219-241, 1980.
- Eckermann, S. et al., Gravity wave and equatorial wave morphology of the stratosphere derived from long-term rocket soundings, *R. Meteorol. Soc.*, 146-186, 1995.
- Eckermann, S. and P. Preuße, Global measurements of stratospheric mountain waves from space, *Science*, *286*, 1433-1436, 1999.
- Endemann M., G. Lange, and B. Fladt, Michelson interferometer for passive atmospheric sounding MIPAS, a high resolution limb sounder for the European Polar Platform, in *Passive Infrared Remote Sensing of Clouds and the Atmosphere*, ed D. K. Lynch, *Proc. SPIE Int. Soc. Opt. Eng.*, 1934, 13-15, 1993.
- Ern, M., Interpolation asymptotischer Satellitendaten, Diplomarbeit, WU-D 93-35, Bergische Universität-Gesamthochschule Wuppertal, Wuppertal 1995.
- Fahey, D. W., et al., In situ measurements constraining the role of sulfate aerosols in mid-latitude ozone depletion, *Nature*, *363*, 509-514, 1993.
- Fetzer E. J. and J. C. Gille, Gravity wave variance in LIMS temperatures, Part I: Variability and comparisons with background winds, *J. Atmos. Sci.*, *51*, 2461-2483, 1994.
- Forbes, J. M., Atmospheric tides 1. Model description and results for the solar diurnal component, *J. Geophys. Res.*, *87*, 5222-5240, 1982.
- Franzen, A., M. Riese, X. Tie, and D. Offermann, Tracer transport in the southern hemisphere as observed during the CRISTA 1 mission, *Geophys. Res. Lett.*, submitted, 2000.
- Fitts, D. C., Gravity wave saturation in the middle atmosphere - a review of theory and observations, *Rev. Geophys. Space Phys.*, *22*, 275-308, 1984.
- Fitts, D. C., A review of gravity wave saturation processes, effects and variability in the middle atmosphere, *Pageoph.*, *130*, 343-370, 1989.
- Garcia, R. R., and S. Solomon, A numerical model of the zonally averaged dynamical and chemical structure of the middle atmosphere, *J. Geophys. Res.*, *88*, 1379-1400, 1983.
- Garcia, R. R., F. Stordal, S. Solomon, and J. T. Kiehl, A numerical model of zonally averaged dynamical and chemical structure in the middle atmosphere, *J. Geophys. Res.*, *97*, 12,967-12,991, 1992.

- Gao, R. S., et al., A comparison of observations and model simulations of NO_x/NO_y in the lower stratosphere, *Geophys. Res. Lett.*, *26*, 1153-1156, 1999.
- Gordley, L. L. and J. M. Russell III, Rapid inversion of limb radiance data using an emissivity growth approximation, *Appl. Opt.*, *20*, 807 - 813, 1981.
- Gordley, L. L., B. T. Marshall, and D. A. Chu, Linepak: Algorithms for modeling spectral transmittance and radiance, *JQRST*, *52*, 563-599, 1994.
- Gille, J. C., and J. M. Russell III, The Limb Infrared Monitor of the Stratosphere: Experiment description, performance, and results, *J. Geophys. Res.*, *89*, 5125-5140, 1984.
- Gille, J. C. and J. J. Barnett, The High Resolution Dynamics Limb Sounder (HIRDLS): An instrument for the study of global change, in *The use of EOS for studies of Atmospheric Physics*, ed Gille J. C. and G. Visconti, pp 439-450, North Holland, Amsterdam, 1992.
- Granier, C. and G. Brasseur, Ozone and other trace gases in the Arctic and Antarctic regions: Three-dimensional model simulations, *J. Geophys. Res.*, *96*, 2995-3011, 1991.
- Grossmann, K. U., Recent improvements in middle atmosphere remote sounding techniques: The CRISTA-SPAS experiment, in: *AGU Monograph*, in print, 2000.
- Hagan, M. E., J. M. Forbes, and F. Vial, On modeling migrating solar tides, *Geophys. Res. Lett.*, *22*, 893-896, 1995
- Hayashi, H., M. Shitani, and J. C. Gille, Vertically stacked temperature distributions near the equatorial stratopause as seen in cryogenic limb array etalon spectrometer data, *J. Geophys. Res.*, *103*, 19,469-19,483, 1998.
- Hays, P. B. et al., The High-Resolution Doppler Imager on the Upper Research Satellite, *J. Geophys. Res.*, *98*, 10713-10723, 1991.
- Haynes, P. H., C. J. Marks, M. E. McIntyre, T. G. Shepard, and T. G. Shine, On the "downward control" of extratropical diabatic circulations and eddy-induced mean zonal forces, *J. Atmos. Sci.*, *48*, 651-678, 1991.
- Hitchman, M. H. and C. B. Leovy, Diurnal tide in the equatorial middle atmosphere as seen in LIMS temperatures, *J. Atmos. Sci.*, *42*, 557-561, 1985.
- Hitchman, M. H., C. B. Leovy, J. C. Gille, and P. L. Bailey, Quasistationary zonally asymmetric circulations in the equatorial lower mesosphere, *J. Atmos. Sci.*, *44*, 2219-2236, 1987.
- Holton, J. R., The dynamic meteorology of the stratosphere and mesosphere, *Meteor. Mono.*, 15(37), Amer. Met. Soc., MA, 1975
- Holton, J. R. and W. -K. Choi, Transport circulation deduced from SAMS trace specie data, *J. Atmos. Sci.*, *45*, 1929-1939, 1988.
- Kaye, J. A. and T. Miller, The ATLAS series of Shuttle missions, *Geophys. Res. Lett.*, *23*, 17, 2285-2288, 1996.
- Kindler, T. P., D. M. Cunnold, F. N. Alyea, W. L. Chameides, G. P. Lou, and K. Schwan, An evaluation using ^{14}C and N_2O simulations of three-dimensional transport driven by United Kingdom Meteorological Office and Goddard Space Flight Center assimilated winds, *J. Geophys. Res.*, *103*, 10,827-10,847, 1998.

- Lehmacher G. A., J. Oberheide, F. J. Schmidlin, and D. Offermann, Zero miss time and zero miss distance experiments for validation of CRISTA 2 temperatures, *Adv. Space Res.*, *26*, 965-969, 2000.
- Lefèvre, F., G. P. Brasseur, I. Folkin, A. K. Smith, and P. Simon, Chemistry of the 1991-1992 stratospheric winter: Three-dimensional model simulations, *J. Geophys. Res.*, *99*, 8,183-8,195, 1994.
- Lübken F. J., Intercomparison of density and temperature profiles obtained by lidar, ionization gauges, falling spheres, datasondes, and radiosondes during the DYANA campaign, *J. Atmos. Terr. Phys.*, *56*, 1969-1984, 1994.
- Mahlman, J. D., H. Levy II, and W. J. Moxim, Three-dimensional simulations of stratospheric N₂O: Predictions for other trace constituents, *J. Geophys. Res.*, *91*, 2687-2707, 1986.
- Manney, G. L., R. W. Zurek, A. O'Neill, and R. Swinbank, On the motion of air through the stratospheric polar vortex, *J. Atmos. Sci.*, *51*, 2973-2994, 1994.
- Manney, G. L. et al., Formation of low-ozone pockets in the middle stratospheric anticyclone during winter, *J. Geophys. Res.*, *100*, 13,939-13,950, 1995.
- Manney, G. L., R. Swinbank, and A. O'Neill, Stratospheric meteorological conditions from the 3 - 12 Nov. 1994 ATMOS/ATLAS-3 measurements, *Geophys. Res. Lett.*, *23*, 2409-2412, 1996.
- Manney, G. L., H. A. Michelson, R. M. Bevilacqua, M. R. Gunson, F. W. Irion, N. J. Livesey, J. Oberheide, M. Riese, J. M. Russell II, J. M. Zawodny, Comparison of ozone observations from seven satellite instruments in early November 1994 in the context of meteorological variability, *to be submitted to JGR*, 2000.
- Marshall, T. B., L. L. Gordley, and D. A. Chu, Bandpak: Algorithms for modeling broadband transmission and radiance, *JQRST*, *52*, 581-599, 1994.
- McIntyre, M. E., and T. N. Palmer, Breaking planetary waves in the stratosphere, *Nature*, *305*, 593-600, 1983.
- Mlynczak, M. G., Energetics of the mesosphere and lower thermosphere and the SABER experiment, *Adv. Space Res.*, *20*, 1177-1183, 1997.
- Morris, G. A., et al., Trajectory mapping and applications to data from the Upper Atmosphere Research Satellite, *J. Geophys. Res.*, *100*, 16,491-16,506, 1995.
- Morris, G. A., D. B. Considine, A. E. Dessler, S. R. Kawa, J. Kumer, J. Mergenthaler, A. Roche, and J. M. Russell III, Nitrogen partitioning in the middle stratosphere as observed by the Upper Atmosphere Research Satellite, *J. Geophys. Res.*, *102*, 8955-8965, 1997.
- Naujokat, B. and S. Pawson, The cold stratospheric winters 1994/1995 and 1995/1996, *Geophys. Res. Lett.*, *23*, 3703-3706, 1996.
- Oberheide, J. M. E. Hagan, W. E. Ward, M. Riese, and D. Offermann, Modeling the diurnal tide for the CRISTA 1 time period, *J. Geophys. Res.*, in print, 2000.
- Offermann, D., The DYANA campaign: A survey, *J. Atmos. Terr. Phys.*, *56*, 1639-1657, 1994.

- Offermann, D. and R. Spang, Detection of stratospheric clouds in Antarctica and in the tropics by CRISTA, *Proceedings of European workshop on mesoscale processes in the stratosphere: Their effect on stratospheric chemistry and microphysics*, Bad Tölz, Germany, 8-11 Nov., 1998.
- Offermann, D., K. U. Großmann, P. Barthol, P. Knieling, M. Riese, and R. Trant, The Cryogenic Infrared Spectrometers and Telescopes for the Atmosphere (CRISTA) experiment and middle atmosphere variability, *J. Geophys. Res.*, *104*, 16,311–16,325, 1999.
- Osterman, G. B., B. Sen, G. C. Toon, R. J. Salawitch, J. J. Margitan, J.-F. Blavier, D. W. Fahey, and R. S. Gao, Partitioning of NO_y species in the summer Arctic stratosphere, *Geophys. Res. Lett.*, *26*, 1157-1160, 1999.
- Preusse, P., M. Riese, J. Oberheide, M. Bittner, K. U. Grossmann, and D. Offermann, Evidence for a zonally trapped diurnal tide in CRISTA temperatures, *Adv. Space Res.*, *19*, 579–582, 1997.
- Preusse, P., B. Schäler, J. T. Bacmeister, and D. Offermann, Evidence for gravity waves in CRISTA temperatures, *Adv. Space Res.*, *24*, 1601–1604, 1999.
- Randel, W. J. J. C. Gille, A. E. Roche, J. B. Kumer, J. L. Mergenthaler, J. W. Waters, E. F. Fishbein, and W. A. Lahoz, Stratospheric transport from the tropics to middle latitudes by planetary wave mixing, *Nature*, *365*, 533–535, 1993.
- Randel, W. J. B. A. Boville, J. C. Gille, P. L. Bailey, S. T. Massie, J. B. Kumer, J. L. Mergenthaler, and A. E. Roche, Simulation of stratospheric N₂O in the NCAR CCM2: Comparison with CLAES data and global budget analysis, *J. Atmos. Sci.*, *51*, 2834–2845, 1994.
- Reber, C. A., Upper Atmosphere Research Satellite (UARS) mission, NASA Rep. 430-1003-001, 1985.
- Riese, M., P. Preusse, R. Spang, M. Ern, M. Jarisch, K. U. Grossmann, and D. Offermann, Measurements of trace gases by the Cryogenic Infrared Spectrometers and Telescopes for the Atmosphere (CRISTA) experiment, *Adv. Space Res.*, *19*, 563–566, 1997.
- Riese, M., Was sind Atmosphärenmodelle?, *Berg. Blätter*, *22*, 21, 1999.
- Riese, M., R. Spang, P. Preusse, M. Ern, M. Jarisch, D. Offermann, and K. U. Grossmann, Cryogenic Infrared Spectrometers and Telescopes for the Atmosphere (CRISTA) data processing and atmospheric temperature and trace gas retrieval, *J. Geophys. Res.*, *104*, 16,311–16,325, 1999a.
- Riese, M., X. Tie, G. Brasseur, and D. Offermann, Three-dimensional simulations of stratospheric trace gas distributions measured by CRISTA, *J. Geophys. Res.*, *104*, 16,419–16,435, 1999b.
- Riese, M., Technical Note to ESA: Review of Algorithm Technical Baseline Document for MIPAS Level 2 processing, 1999c.
- Riese, M., Technical Note to NASA: Review of Algorithm Technical Baseline Document for TES Level 1 and TES Level 2 processing, 1999d.
- Riese, M., R. Spang, J. Oberheide, G. Lehmacher, P. Preuß, and D. Offermann, Some results of the Cryogenic Infrared Spectrometers and Telescopes for the Atmosphere (CRISTA)

- Experiment, *Proc. 14th Symp. on European Rocket and Balloon Programmes and Related Research*, Potsdam, Germany, 31 May-3 June, 1999e.
- Riese, M., Initialization of CTM simulations by means of the UARS reference atmosphere, *Adv. Space Res.*, submitted, 2000.
- Riese, M. and D. Offermann, CRISTA 1 Data Evaluation: Final Report, University of Wuppertal, Wuppertal, June 2000.
- Riese, M., X. Tie, G. Brasseur, D. Offermann, and R. Spang, Three-dimensional simulations of CRISTA trace gas measurements, *Adv. Space Res.*, *26*, 971–974, 2000a.
- Riese, M. V. Küll, X. Tie, G. Brasseur, D. Offermann, G. Lehmacher, and A. Franzen, Modeling of nitrogen species measured by CRISTA, *Geophys. Res. Lett.*, *27*, 2221–2225, 2000b.
- Reber, C. A., Upper Atmosphere Research Satellite (UARS) mission, NASA Rep. 430-1003-001, 1985.
- Roche, A. E., J. B. Kumer, J. L. Mergenthaler, G. A. Ely, W. G. Ulpinger, J. F. Potter, T. C. James, and L. W. Sterrit, The Cryogenic Limb Array Etalon Spectrometer (CLAES) on UARS: Experiment description and performance, *J. Geophys. Res.*, *98*, 10,763–10,775, 1993.
- Rodgers, C., Statistical principles of inversion theory, in *Inversion Methods in Atmospheric Remote Sensing*, edited by A. Deepak, pp. 117-134, Academic, San Diego, Calif., 1976.
- Rood, R. B., D. J. Allen, W. E. Baker, D. J. Lamich, and J. A. Kaye, The use of assimilated stratospheric data in constituent transport calculations, *J. Atmos. Sci.*, *46*, 687–701, 1989.
- Rood, R. B., A. E. Douglass, J. A. Kaye, M. A. Geller, C. Yuechen, D. J. Allen, E. M. Larson, E. R. Nash, and J. E. Nielson, Three-dimensional simulations of wintertime ozone variability in the lower stratosphere, *J. Geophys. Res.*, *96*, 5055–5071, 1991.
- Rood, R. B., E. Nielsen, R. Stolarski, A. Douglass, J. Kaye, and D. J. Allen, Episodic total ozone minima and associated effects on heterogeneous chemistry and lower stratospheric transport, *J. Geophys. Res.*, *97*, 7979–7996, 1992.
- Rose, K., On the influence of nonlinear wave-wave interactions in a 3-d primitive equation model for sudden stratospheric warmings, *Beitr. Phys. Atmosph.*, *19*, 14–41, 1983.
- Rose, K. and G. Brasseur, A three-dimensional model of chemically active trace species in the middle atmosphere during disturbed winter conditions, *J. Geophys. Res.*, *96*, 16,387–16,403, 1989.
- Rosenlof, K. H. and J. R. Holton, Estimates of the stratospheric residual circulation using the downward control principle, *J. Geophys. Res.*, *98*, 10,456–10,479, 1993.
- Russell, J. M. III, and S. R. Drayson, The inference of atmospheric ozone using satellite horizon measurements in the 1024 cm⁻¹ band, *J. Atmos. Sci.*, *29*, 376-390, 1972.
- Salawitch, R. J., et al., The distribution of hydrogen, nitrogen, and chlorine radicals in the lower stratosphere: Implications for changes on O₃ due to emissions of NO_y from supersonic aircraft, *Geophys. Res. Lett.*, *21*, 2547-2550, 1994.
- Salby, M. L., Sampling theory for synoptic satellite observations, I., Space-time spectra, resolution, and aliasing, *J. Atmos. Sci.*, *39*, 2577–2600, 1982a.

- Salby, M. L., Sampling theory for asynoptic satellite observations, II., Fast Fourier synoptic mapping, *J. Atmos. Sci.*, *39*, 2601–2614, 1982b.
- Salby, M. L., Survey of planetary-scale traveling waves: the state of theory and observations, *Rev. Geophys. Space Phys.*, *22*, 209–236, 1984.
- Sassi, F., R. R. Garcia, and B. A. Boville, The stratopause oscillation in the NCAR community climate model, *J. Atmos. Sci.*, *50*, 3608–3624, 1993.
- Sen, B., G. C. Toon, G. B. Osterman, J.-F. Blavier, J. J. Margitan, R. J. Salawitch, and G. K. Yue, Measurements of nitrogen in the stratosphere, *J. Geophys. Res.*, *103*, 3571–3585, 1998.
- Schäler, B. and M. Riese, Retrieval of water vapor in the tropopause region from CRISTA measurements, *Adv. Space Res.*, submitted, 2000.
- Schmidlin, F. J. et al., The inflatable sphere: A technique for the accurate measurement of middle atmosphere temperature, *J. Geophys. Res.*, *96*, 22,673–22,682, 1991.
- Schoeberl, M. R., L. R. Lait, P. A. Newman, and J. E. Rosenfield, The structure of the polar vortex, *J. Geophys. Res.*, *97*, 7859–7882, 1992.
- Shepherd, G. G. et al., WINDII, the wind imaging interferometer on the Upper Atmosphere Research Satellite, *J. Geophys. Res.*, *98*, 10725–10750, 1993.
- Shepherd, T. G., J. N. Koshyk, and K. Ngan, On the nature of large-scale mixing in the stratosphere and mesosphere, *J. Geophys. Res.*, *105*, 12,433–12,446, 2000.
- Smith, A. K., Numerical simulations of global variations of temperature, ozone, and trace species in the stratosphere, *J. Geophys. Res.*, *100*, 1253–1269, 1995.
- Smith, A. K. and M. Riese, CRISTA observations of tracer transport by inertially unstable circulations, *J. Geophys. Res.*, *104*, 19,171–19182, 1999.
- Smolarkiewicz, P. K. and P. J. Rasch, Monotone advection on the sphere: An Eulerian versus semi-Lagrangian approach, *J. Atmos. Sci.*, *48*, 793–810, 1991.
- Solomon, S., J. T. Kiehl, R. R. Garcia, and W. Grose, Tracer transport by the diabatic circulation deduced from satellite observations, *J. Atmos. Sci.*, *43*, 1603–1617, 1986.
- Solomon, S., R. W. Portmann, R. R. Garcia, L. W. Thomason, and M. P. Mc Cormick, The role of aerosol variations in anthropogenic ozone depletion at northern midlatitudes, *J. Geophys. Res.*, *101*, 6713–6727, 1996.
- Spang, R., Das Datensystem zur Auswertung der CRISTA-Missionsdaten, Dissertation, WUB-DIS 97-4, Bergische Universität-Gesamthochschule Wuppertal, Wuppertal 1997.
- Spang, R., M. Riese, and D. Offermann, CRISTA-2 observations of the south polar vortex in winter 1997: A new data set for polar process studies, *Geophys. Res. Lett.*, submitted, 2000.
- Stanford, J. L., J. R. Ziemke, and S. Y. Gao, Stratospheric circulation features deduced from SAMS constituent data, *J. Atmos. Sci.*, *50*, 226–246, 1993.
- Suarez, M. J., S. Schubert, A. Molod, C. Park, L. Takacs, C. Wu, M. Seabloom, W. Higgins, R. Rood, and Y. Kondratyeva, A multi-year assimilation with the GEOS-1 system: Overview and results, , *NASA Tech. Memo.*, *104606*, 1995.

- Swinbank, R. and A. O'Neill, A Stratosphere-Troposphere data assimilation system, *Monthly Weather Review*, 122, 686-702, 1994.
- Taylor, F. W., et al., Remote sensing of atmospheric structure and composition by pressure modulator radiometry from space: The ISAMS experiment on UARS, *J. Geophys. Res.*, 98, 10799-10814, 1993.
- Trepte, C. R., R. E. Veiga, and M. P. McCormick, The poleward dispersal of Mount Pinatubo volcanic aerosol, *J. Geophys. Res.*, 98, 18563-18573, 1993.
- Ward, W. E., J. Oberheide, M. Riese, P. Preusse, and D. Offermann, Tidal signatures in temperature data from the CRISTA I mission, *J. Geophys. Res.*, 104, 16,319–16,403, 1999.
- Ward, W. E., J. Oberheide, M. Riese, P. Preusse, and D. Offermann, Planetary wave two signatures in CRISTA II ozone and temperature data, *Geophys. Monograph.*, in press, 2000.
- Wu, D. L. and J. W. Waters, Satellite observation of atmospheric variance: A possible indication of gravity waves, *Geophys. Res. Lett.*, 23, 3631–3634, 1996.
- Wattenbach, R., and K. Moritz, Astronomical Shuttle Pallet Satellite (ASTRO-SPAS), *Acta Astronaut.*, 40, 723–732, 1997.